

Important Notice

This copy may be used only for the purposes of research and private study, and any use of the copy for a purpose other than research or private study may require the authorization of the copyright owner of the work in question. Responsibility regarding questions of copyright that may arise in the use of this copy is assumed by the recipient.

UNIVERSITY OF CALGARY

1.5D Internal Multiple Prediction: an Application on Synthetic Data, Physical Modelling Data
and Land Data Synthetics

by

Pan Pan

A THESIS

SUBMITTED TO THE FACULTY OF GRADUATE STUDIES
IN PARTIAL FULFILMENT OF THE REQUIREMENTS FOR THE
DEGREE OF MASTER OF SCIENCE

GRADUATE PROGRAM IN GEOLOGY AND GEOPHYSICS

CALGARY, ALBERTA

JUNE, 2015

© Pan Pan 2015

Abstract

A 1.5D implementation of the inverse scattering series internal multiple prediction algorithm is investigated with the challenges of land seismic data application in mind. This method does not require any subsurface information and is suitable for situations where there is close interference between primaries and internal multiples; however, in land environments, issues of noise, coupling and statics have led to fewer reported successes. The methodology is also computationally costly, with the cost increasing dramatically as the implementation makes the transition from its 1D form to 1.5D, 2D and ultimately 3D. With these issues in mind, the algorithm is examined using a step-by-step approach: first, by carrying out synthetic examples; second, by testing physical modelling data; and finally, by operating on well log synthetics from land data. In the synthetic environment a study is undertaken to determine under what circumstances lower-dimension versions of the prediction algorithm can be applied to higher dimension problems to take advantage of the computational speed. The effects of various ϵ values are analyzed. A method to mitigate large-dip artifacts noticeable in unfiltered 1.5D internal multiple prediction is developed. Applicability of these ideas to real measurements taken in a physical modelling experiment, and using realistic synthetic data produced from real well logs is confirmed.

Acknowledgements

First of all, I would like to express my gratitude to my supervisor Dr. Kris Innanen for his supervision, leadership, advice, and guidance. He has played an important role in my life during my MSc program; he is not only a mentor but also a friend. He has provided me with endless encouragement and support in various ways. Secondly, I would like to thank sponsors of CREWES project and NSERC (Natural Science and Engineering Research Council of Canada) for providing the financial means to complete my MSc program.

A major component in this thesis is about physical modelling data and I feel fortunate to have had the opportunity to work in the Seismic Physical Modelling Facility to collect physical modelling data. I'd like to acknowledge Dr. Joe Wong for his help in acquiring the physical modelling data, his advice and many discussions. Thank you for advising me to learn the use of ProMAX to process my own data. Thank you to Mr. Kevin Bertram, who was a great help with physical modelling experiment. Thank you to Mr. David Henley for helping with the pre-processing.

I would like to thank Dr. Larry Lines and Dr. Harvey Yarranton for agreeing to be the examiners of my defense and posing thought-provoking questions during my defense. I would like to thank Dr. Gary Margrave for his superb instruction on signal processing. Thank you to Mr. Kevin Hall for helping me whenever possible when it came to any computer issues and to Mr. Malcolm Bertram for his help during field school and demonstrating refraction techniques. Thank you to Laura Baird for all of the hard work that she does to make a better CREWES. She is always the one that telling me how wonderful I am, giving me confidence and trying to ensure that I have

everything I need. Thank you to Dr. Helen Isaac and Mr. Andreas Cordsen for coming to my defense presentation.

I would especially like to thank two fellow students who have been with me since I started my MSc program. Babatunde Arenrin, who helped me work out any problems I had and guided my choice made with the Hussar synthetic data experiment. He is an incredible source of inspiration and a pleasure to work with. I would also like to thank Shahin Moradi who helped me solve any problems regarding MATLAB code, and shared the happiness in my life.

I would like to thank all of my office mates and fellow students at CREWES for all of your helpful suggestions and comments during my time at the University. I'd like to thank Wenyong Pan, Tianci Cui, Jean Cui, Jian Sun, Rafael Asuaje, Raúl Cova, Jessica Dongas, Marcelo Guarido de Andrade, Shahin Jabbari, Scott Keating, Bobby Gunning, Michelle Montano, Shahpoor Moradi, Eric Rops, Bona Wu, Junxiao Li, Khaled Al Dulaijan, Jesse Kolb, and Adrian Smith for sharing my great experience as a graduate student.

I would like to thank my parents for supporting me to study aboard, without their help and encouragement I would never have made it this far. Last but not least, I would like to show my appreciation to my husband Yichi Zhang and my best friend Rosa La for assisting me during the final editing stage of my thesis.

To my beloved parents and my husband Yichi

Table of Contents

Abstract	ii
Acknowledgements	iii
Dedication	v
Table of Contents	vi
List of Tables	viii
List of Figures and Illustrations	ix
List of Symbols, Abbreviations, Nomenclatures	xiv
CHAPTER ONE: INTRODUCTION	1
1.1 Statement of the problem	1
1.2 Previous work concerning multiple attenuation	2
1.2.1 Method I: Deconvolution methods	2
1.2.2 Method II: Filtering methods	3
1.2.3 Methods III: Wavefield prediction and subtraction methods	5
1.3 Theoretical background	6
1.3.1 Classification of seismic events	6
1.3.2 Scattering theory	10
1.3.3 Internal multiple prediction algorithms	12
1.3.3.1 Internal multiple prediction in 2D	12
1.3.3.2 Internal multiple prediction in 1D	13
1.3.3.3 Internal multiple prediction in 1.5D	14
1.3.4 Lower-higher-lower relationship	14
1.4 1D example	17
1.4.1 Subevent interpretation of internal multiples	17
1.4.2 1D numerical example	19
1.5 Thesis overview	21
1.6 Hardware and software	22
CHAPTER TWO: 1D INTERNAL MULTIPLE PREDICTION	24
2.1 Chapter overview	24
2.2 Synthetic example	24
2.3 Systematic study of prediction errors	28
2.3.1 The influence of offset	28
2.3.2 The influence of dipping angles	29
2.3.2.1 Case I	29
2.3.2.2 Case II	30
2.3.2.3 Case III	31
2.4 Towards making practical recommendations	32
2.5 Chapter summary	33
CHAPTER THREE: NUMERICAL ANALYSIS OF 1.5D INTERNAL MULTIPLE PREDICTION	34
3.1 Chapter overview	34
3.2 Synthetic example	34
3.2.1 Velocity model and shot record	34

3.2.2 Making the pseudo-depth domain input $b_1(k_g, z)$	37
3.2.3 Internal multiple prediction	39
3.3 Analysis on the effects of ϵ values.....	41
3.4 Analysis on the effects of dipping angles	42
3.5 Analysis on large-dip artifacts	48
3.6 Chapter summary	55
CHAPTER FOUR: MULTIPLE PREDICTION ON PHYSICAL MODELLING DATA	56
4.1 Chapter overview	56
4.2 Physical modelling experiment overview.....	56
4.2.1 Introduction to physical modelling systems	56
4.2.2 The physical model set-up.....	57
4.2.3 Physical modelling data acquisition	58
4.3 Seismic data processing.....	60
4.4 1.5D Internal multiple prediction.....	63
4.4.1 Event identification	63
4.4.2 Internal multiple prediction	67
4.4.3 Analysis of the three parameters chosen in the algorithm.....	70
4.5 Chapter summary	74
CHAPTER FIVE: THE HUSSAR EXPERIMENT	76
5.1 Chapter overview	76
5.2 The Hussar experiment overview	77
5.2.1 Introduction	77
5.2.2 Well log analysis	78
5.3 Hussar synthetics experiment	80
5.3.1 Block log	80
5.3.2 Internal multiple prediction	81
5.3.3 Relatively thin layers test	85
5.4 Chapter summary	88
CHAPTER SIX: CONCLUSIONS	90
6.1 Conclusions.....	90
6.2 Recommendations.....	92
6.3 Future work.....	93
REFERENCES	94

List of Tables

Table 1.1: Parameters of the synthetic model.....	21
Table 2.1: Parameters of the velocity model and shot record.....	26
Table 3.1: Parameters of the velocity model and shot record.....	36
Table 3.2: Parameters of the new velocity model.....	40
Table 3.3: Parameters of the new velocity model and shot record.....	52
Table 4.1: A processing flow applied to the physical modelling data.	60
Table 4.2: Summary of approximate travel times of the identified events.....	66
Table 4.3: Time costs with different parameters chosen	74

List of Figures and Illustrations

Figure 1.1: Multiple removal using <i>tau-p</i> transforms (from Kabir and Marfurt, 1999). (a) Original data with primaries and multiples. (b) and (c) after forward transformation, in which primaries and multiples are well separated. (d) Primaries are muted. (e) Inverse transformation to estimate multiples. (f) Primaries remaining after subtracting the multiples in (e).	5
Figure 1.2: Examples of the direct-arrival and the direct-arrival ghost (modified from Weglein and Dragoset, 2005). (a) The path of the direct arrival. (b) The path of the direct-arrival ghost. The blue-green area represents the water layer. The red and yellow dots indicate the positions of seismic sources and receivers, respectively. The white lines are raypaths of the events being defined.	7
Figure 1.3: Ghost events that move upward from the source and/or downward to the receiver, and interact with the free-surface (modified from Weglein and Dragoset, 2005). (a) The source ghost; (b) the receiver ghost; (c) the source-receiver ghost.....	8
Figure 1.4: Illustration of primary reflections (modified from Weglein and Dragoset, 2005).	9
Figure 1.5: FSMs (modified from Weglein and Dragoset, 2005). (a) A FSM reflection; (b) first-order FSM reflects once from the free-surface; (c) second-order FSM reflects twice from the free-surface.	9
Figure 1.6: Internal multiples (modified from Weglein and Dragoset, 2005). (a) A first-order internal multiple; (b) a second-order internal multiple.	9
Figure 1.7: Construction of the travel times of an internal multiple.....	15
Figure 1.8: Two combinations of sums and differences of primary travel times. In (a) the combination of sums and difference produces an internal multiple, whereas in (b) it produces artifacts that does not correspond to any physical event.	16
Figure 1.9: Construction of an internal multiple using subevents (modified from Weglein and Matson, 1998). The first subevent is a primary reflection that travels from point ‘a’, reflected from the second reflector, and is received at point ‘c’. The second subevent is a primary that propagates from point ‘b’, reflected from the first interface ‘e’, and received at point ‘c’. The third one is a primary from point ‘b’ to ‘d’, reflected from the second interface.....	17
Figure 1.10: A numerical example of 1D internal multiple prediction. The zero-offset trace with three primaries and two associated first-order internal multiples. The arrival times for the two internal multiples are $t_1 = 0.98s$ and $t_2 = 1.07s$, respectively.	20
Figure 1.11: Applying the 1D internal multiple attenuation algorithm to the synthetic model. (a) Input data; (b) input data with focus on internal multiples; (c) prediction output; (d) prediction output with focus on internal multiples.	20

Figure 2.1: Four-layer velocity model.	25
Figure 2.2: (a) Shot record of the model with the direct wave removed. (b) Zero-offset trace. (c) The same trace as (b) with a larger scale. Yellow lines show the positions of primaries, and red lines indicate the positions of internal multiples.....	25
Figure 2.3: Application of the 1D internal multiple prediction algorithm to the zero-offset trace. (a) Input data. (b) Prediction output. The red circles indicate the positions of the internal multiples in the input and output data.....	27
Figure 2.4: The ray paths of the two dominant internal multiples.....	27
Figure 2.5: The relative travel time errors between predicted and actual multiples plotted against increasing offset.....	28
Figure 2.6: The relative travel time errors between predicted and actual multiples in the zero-offset trace plotted against an increasing series of dipping angles, with the generator as the dipping interface.	30
Figure 2.7: The relative travel time errors between predicted and actual multiples in the zero-offset trace plotted against an increasing series of dipping angles, with the second interface as the dipping interface.	31
Figure 2.8: The relative travel time errors between predicted and actual multiples in the zero-offset trace plotted against an increasing series of dipping angles, with the third interface as the dipping interface.	32
Figure 3.1: Four-layer velocity model used to generate synthetic data to test the 1.5D internal multiple prediction algorithm.	35
Figure 3.2: Shot record calculated using the velocity model in Figure 3.1. (a) Zero-offset travel times of primaries are indicated by yellow lines; (b) zero-offset travel times of internal multiples are indicated by red lines.	36
Figure 3.3: The input $b_1(k_g, z)$ is generated using the input data and reference velocity c_0	38
Figure 3.4: Comparison of the input zero-offset trace and constructed input. (a) Input data: zero-offset trace; (b) constructed input stacked over the wavenumbers. The red circles and the blue circles show locations of primaries and internal multiples, respectively.	39
Figure 3.5: The output of the 1.5D internal mutiple prediction with an ϵ value of 200 ms. (a) The two predicted internal mutiples. (b) The original data with both priamries and internal multiples.	40
Figure 3.6: The output of the 1.5D internal mutiple prediction with an ϵ value of 200 ms. In this case, a primary and an internal multiple interfere. (a) The two predicted internal mutiples. (b) The original data with both priamries and internal multiples.....	41

Figure 3.7: Comparison of outputs of the 1.5D internal multiple predictions with ϵ values of 100, 200, and 300 respectively. (a) The output with an ϵ value of 100 ms. (b) The output with an ϵ value of 200 ms. (c) The output with an ϵ value of 300 ms.	42
Figure 3.8: Four-layer velocity model with the first interface's dipping at 2 degrees.....	43
Figure 3.9: Shot record calculated using the velocity model in Figure 3.8. (a) Zero-offset travel times of primaries are indicated by yellow lines; (b) zero-offset travel times of internal multiples are indicated by red lines.	43
Figure 3.10: The output of the 1.5D internal multiple prediction with an ϵ value of 200 ms. (a) The two predicted internal multiples. (b) The original data with both primaries and internal multiples. Red lines indicate the positions of the internal multiples.	44
Figure 3.11: Four-layer velocity model with the first interface dipping at an angle of 5 degrees.	45
Figure 3.12: Shot record calculated using the velocity model in Figure 3.11. (a) Zero-offset travel times of primaries are indicated by yellow lines; (b) zero-offset travel times of internal multiples are indicated by red lines.	45
Figure 3.13: The output of the 1.5D internal multiple prediction with an ϵ value of 180 ms. (a) The two predicted internal multiples. (b) The original data with both primaries and internal multiples. Red lines indicate the positions of the internal multiples.	46
Figure 3.14: Prediction errors of IM1 plotted against an increasing series of dipping angles.	47
Figure 3.15: Prediction errors of IM2 plotted against an increasing series of dipping angles.	48
Figure 3.16: Three-layer velocity model used to test the large-dip artifacts. Medium velocities range from 1500 m/s (top) to 2800 m/s (middle) to 4200 m/s (bottom).	50
Figure 3.17: Shot record calculated using the synthetic model in Figure 3.16. (a) Zero-offset travel times of primaries are indicated by the yellow lines; (b) zero-offset travel times of internal multiples are indicated by the red lines.	50
Figure 3.18: The input for the internal multiple prediction algorithm.....	51
Figure 3.19: The output of the 1.5D internal multiple prediction with a fixed ϵ value of 180 ms. (a) The two predicted internal multiples. (b) The original data with both primaries and internal multiples.....	51
Figure 3.20: The scheme to mitigate large-dip artifacts. (a) Illustration of the input consisting of one event to the prediction algorithm; (b) a fixed ϵ value chosen based on pseudo-depth at $k_g = 0$; (c) coping method used to account for the tendency of $b_1(k_g, z)$ to spread out in z as k_g increases (from Innanen and Pan, 2014).	53

Figure 3.21: The scheme to derive the function of $\epsilon(k_g)$	54
Figure 3.22: Internal multiple predictions using a linear $\epsilon(k_g)$ method. (a) Prediction result; (b) the original data.	54
Figure 4.1: Schematic diagram of the physical modelling experiment. All lengths are in scaled units (i.e., physical modelling units multiplied by 10000). The transducers are set just below the water surface.....	58
Figure 4.2: The 3D positioning system with source and receiver mounted on the gantries. Physical models are placed in a tank of water beneath the gantries.	59
Figure 4.3: Plan view of the physical modelling data acquisition. All units are in field scale.	60
Figure 4.4: Raw data.	62
Figure 4.5: Raw data after applying trace mute.....	62
Figure 4.6: The deconvolved data with decon operator length of 80 ms and operator prediction distance of 35 ms. A bandpass filter of 15-20-70-90 Hz was also applied.....	63
Figure 4.7: Event identification by calculating two-way travel times. Reflection events are labeled on the physical modelling dataset. (a) Synthetic data generated from the same parameters as physical modelling data; (b) physical modelling data.....	64
Figure 4.8: The zero-offset trace from physical modelling data (a) and the zero-offset trace from synthetic data (b).	65
Figure 4.9: The ray paths of the four dominant internal multiples expected from the physical model. IM2 consists of two peg-leg paths, whose travel times are identical.....	67
Figure 4.10: Comparison of input data (a) with prediction output (b). The red lines indicate the positions of internal multiples.....	69
Figure 4.11: Details of internal multiple predictions. (a) Input data: the zero-offset trace from the physical modelling data; (b) prediction output: the zero-offset trace from the prediction output in Figure 4.10; (c) the zero-offset trace from the synthetic data.	70
Figure 4.12: Prediction algorithm in the code (from Innanen, 2012).	71
Figure 4.13: Comparison of two internal multiple prediction outputs with different maximum and minimum frequencies. (a) 30-80 Hz; (b) 10-50 Hz.....	72
Figure 4.14: Fourier amplitude spectrums of the zero-offset trace using decibel scale.	72
Figure 4.15: The algorithm input is generated using the input data and the single reference velocity. Note that this is only one side of the data; the other side can be filled later through conjugate symmetry.....	73

Figure 5.1: The 4.5 km Hussar seismic line is shown along with the locations of the three wells (from Lloyd, 2013).	78
Figure 5.2: Well 12-27 P-wave sonic log with geological markers.....	79
Figure 5.3: A blocked P-wave velocity profile. (a) Shows the original log in black and the blocked log in red; (b) shows only the blocked log. The depth step of the log being blocked is 100 m.	81
Figure 5.4: Velocity model based on the blocked P-wave velocity profile.	82
Figure 5.5: Shot record generated from the velocity model.	83
Figure 5.6: The algorithm input is generated using the input data and single reference velocity.....	83
Figure 5.7: Comparison of prediction output with input. (a) Prediction output; (b) input data....	84
Figure 5.8: Comparison of prediction output with input. (a) Prediction output; (b) input data....	85
Figure 5.9: A blocked P-wave velocity profile. (a) Shows the original log in black and the blocked log in red; (b) shows only the blocked log. The depth step of the log being blocked is 50 m.	86
Figure 5.10: Velocity model based on the new blocked P-wave velocity profile.	87
Figure 5.11: Shot record generated from the new velocity model.....	87
Figure 5.12: Comparison of prediction output with input. (a) Prediction output; (b) input data..	88

List of Symbols, Abbreviations, Nomenclatures

Symbol	Definition
AVO	Amplitude variation with offset
AVAZ	Amplitude variation with azimuth
CREWES	Consortium for Research in Elastic Wave Exploration Seismology
IM	Internal multiple
FSM	Free-surface multiple
FWI	Full waveform inversion
PVC	Polyvinyl chloride
P-wave	Compressional wave
S-wave	Shear wave
SRME	Surface-related multiple elimination
ϵ	Search-limiting parameter
τ	Intercept time
p	Ray parameter
τ - p	Intercept time-ray parameter
t - x	Time-offset
f - k	Frequency-wavenumber
k_g	Geophone lateral wavenumber
k_s	Source lateral wavenumber
k_z	Vertical wavenumber
q_g	Geophone vertical wavenumber
q_s	Source vertical wavenumber
t	Travel time
ω	Temporal frequency
c_0	Reference velocity
z	Pseudo-depth
G	Green's function
L	Differential operator
δ	Source disturbance
V	Perturbation operator

G_s	Scattered field
D	Measured data
R	Reflection coefficient
T	Transmission coefficient
ϵ_{\min}	Minimum value of ϵ
ϵ_{\max}	Maximum value of ϵ
$k_g \text{ End}$	End of geophone lateral wavenumber

Chapter One: Introduction

1.1 Statement of the problem

There are numerous examples of multiple reflection events being interpreted as primaries that resulted in the loss of millions of dollars drilling dry holes (Ikelle et al., 1997). Seismic data processing techniques assume that reflection data consist only of primaries (Weglein, 1999), and multiples are noise to be removed. Multiples need to be attenuated or removed prior to migration, conventional inversion, amplitude-variation-with-offset (AVO) analysis, and interpretation. Otherwise, multiple events can be mistaken for primary reflections, distort primary events, and obscure the task of interpretation (Hernandez, 2012).

Multiple removal has been a longstanding and only partially solved problem in the field of exploration seismology for decades (Weglein, 1999) because assumptions and pre-requisites required for existing multiple removal methods are difficult to fulfill. However, interest in internal multiple prediction remains high (Wu and Weglein, 2014; De Melo et al., 2014; Zhou and Weglein, 2013; Weglein, 2014).

The prediction and removal of internal multiples can be even more challenging for onshore targets. These problems require high processing costs, a more complete sampling and strict definition of the seismic experiment (Weglein, 1999). The characteristics of land seismic data are major obstacles for internal multiple elimination, including low signal-to-noise ratio, statics, fine layers, and poor spatial sampling. Surface-related multiple elimination (SRME) is a well-known method in the application of marine seismic data. However, it is not always suitable for land cases due to the characteristics of land seismic data. Instead, the inverse scattering series

approach (Weglein et al., 1997; 2003) can be a better solution for land application but with much higher computation cost. Luo et al. (2011) reported significant improvements in tests of the inverse scattering series approach; recently Hernandez and Innanen (2014) has demonstrated clear predictions based on the latter theory on poststack land datasets.

1.2 Previous work concerning multiple attenuation

Sloat (1948) was the first geophysicist to identify multiples as “echo reflections” because of its periodic nature. Since then many methods have been developed to attenuate or remove multiples. Methods that attenuate multiples can be classified into three broad categories: (1) deconvolution methods that use the periodicity of multiples; (2) filtering methods that exploit the difference between the normal moveout for primary events and that for multiples; and (3) wavefield prediction and subtraction methods that are based on the predictions from modelling or inversion of the recorded seismic wavefield.

1.2.1 Method I: Deconvolution methods

Deconvolution methods use periodicity to attenuate multiples. This method is useful for surface-related multiples because they arrive many times whereas primaries arrive once for each reflector. In theory, this periodic assumption is only valid at zero-offset in the time-space domain and is less effective with increasing offsets. In practice, deconvolution methods can still be used in situations where there are small violations of the assumption of one-dimensional layers and are more effective by transforming the data into the *tau-p* domain.

Deconvolution methods include predictive deconvolution, adaptive deconvolution and multichannel deconvolution. Predictive deconvolution is based on the autocorrelation function of the time series that can be used to remove the periodicity, and hence, the multiples (Henley and Wong, 2013). Thus, it is useful in suppressing short period free-surface multiples generated at shallow reflectors (Peacock and Treitel, 1969). Adaptive deconvolution has been successfully applied to field datasets (Verschuur et al., 1992; Verschuur and Prein, 1999). It suppresses multiples within a short time varying period, but it is expensive to apply and can become unstable in the presence of noise (Hardy and Hobbs, 1991). Multichannel deconvolution has been proposed to remove the effects of strong lateral inhomogeneity which are not addressed by conventional deconvolution methods (Lamont et al., 1999; Morley and Claerbout, 1983). It has been extended to suppress free-surface multiples generated by the sea floor and a strong reflector below the water bottom (e.g. the top of a salt or basalt layer) (Landa et al., 1999a; Landa et al., 1999b; Lokshantov, 1999).

1.2.2 Method II: Filtering methods

Filtering methods utilize differential moveout between primaries and multiples in τ - p , f - k or t - x domains. These methods suppress multiples at moderate to deep reflectors where multiples and primaries are well separated. If the moveout differences are small, these methods can lead to erroneous results. Also, filtering methods may fail for data with near-offsets, because differential moveout diminishes with near offsets and thus an inner mute is often applied to eliminate traces in this range (Yilmaz, 1989).

The τ - p transform is a special case of the Radon transform, which transforms seismic data from the time-offset (t - x) domain to the intercept time-ray parameter (τ - p) domain. Events such as direct arrivals, ground roll and multiples are difficult to separate in the t - x domain. However, in the τ - p domain, they can be easily separated, since they have different incident angles or different p values (Yan, 2002). In order to avoid the distortion of primaries, a mute is usually applied to remove the primaries after the τ - p transform. The multiples are transformed back to the t - x domain, and subtracted from the original dataset to obtain primaries only. Figure 1.1 illustrates how the τ - p transforms work.

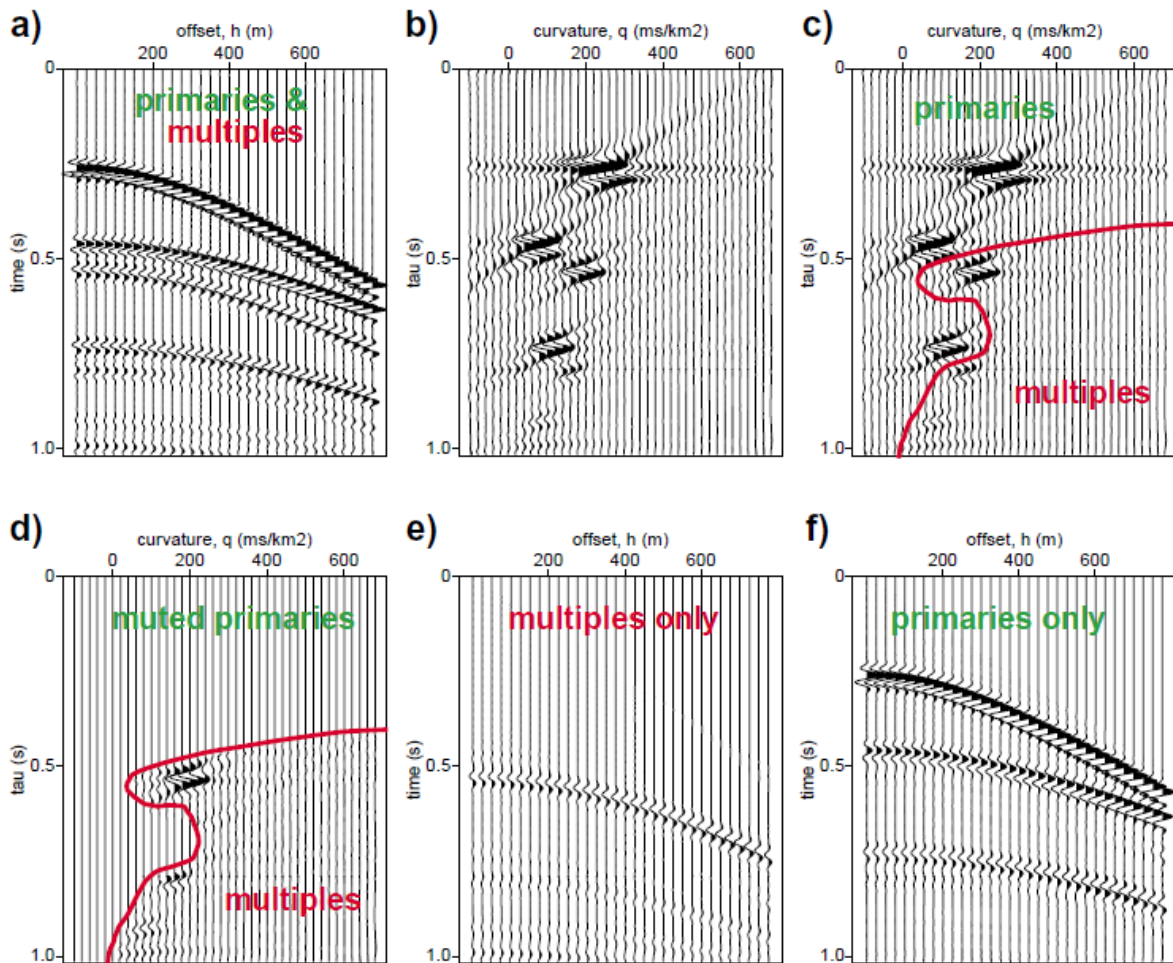


Figure 1.1: Multiple removal using τ - p transforms (from Kabir and Marfurt, 1999). (a) Original data with primaries and multiples. (b) and (c) after forward transformation, in which primaries and multiples are well separated. (d) Primaries are muted. (e) Inverse transformation to estimate multiples. (f) Primaries remaining after subtracting the multiples in (e).

1.2.3 Methods III: Wavefield prediction and subtraction methods

Wavefield prediction and subtraction methods are based on the wave equation, using recorded data or models to predict and subtract multiples. These methods seek data with minimum energy by adaptive subtraction of the predicted multiples, given the knowledge of the source signature or the reflectivity (Xiao et al., 2003). The most exceptional advantage of these methods is their

ability to suppress multiples without harming primaries. This is especially useful in cases where primaries and multiples interfere. However, wavefield prediction and subtraction methods are expensive, and are more limited by data acquisition parameters and processing procedures than other methods.

There are three different wavefield prediction and subtraction techniques: wavefield extrapolation, SRME, and inverse scattering series. Each technique is based on a unique concept concerning the prediction and removal of multiples, and each requires a different level of a priori and/or a posteriori information (Weglein, 1999). Wavefield extrapolation is a modelling and subtraction method; whereas, SRME and inverse scattering methods are based on the prediction mechanisms within two different inversion procedures (Berkhout, 1982; Verschuur et al., 1992; Verschuur, 1991; Weglein et al., 1997).

There is no optimal method for all cases of multiple attenuation because the performance of each technique depends on how well a dataset can fit into the assumptions of the methods. The choice of which multiple attenuation methods to use should be dependent on effectiveness, cost, and processing objectives (Xiao et al., 2003).

1.3 Theoretical background

1.3.1 Classification of seismic events

An event is a distinct arrival of wave energy. The basic classification scheme by which reflection seismic events are discriminated is as follows. The direct arrival travels in a straight line from the source to receivers, without hitting any reflector; see Figure 1.2 (a). The direct-arrival ghost

propagates upward from the source, reflects off of the water surface, and then travels straight to the receiver; see Figure 1.2 (b). Other types of ghost events are source ghost, receiver ghost and source-receiver ghost. Ghosts only exist when there is a free-surface. Source ghosts are events that propagate upward from the source, reflect off the free-surface and are recorded as upgoing waves at a receiver (Figure 1.3 (a)). Receiver ghosts travel downward from the source, interact with the free-surface and are recorded as downgoing waves at a receiver (Figure 1.3 (b)). Source-receiver ghosts have source and receiver attributes of source and receiver ghosts, respectively (Figure 1.3 (c)).

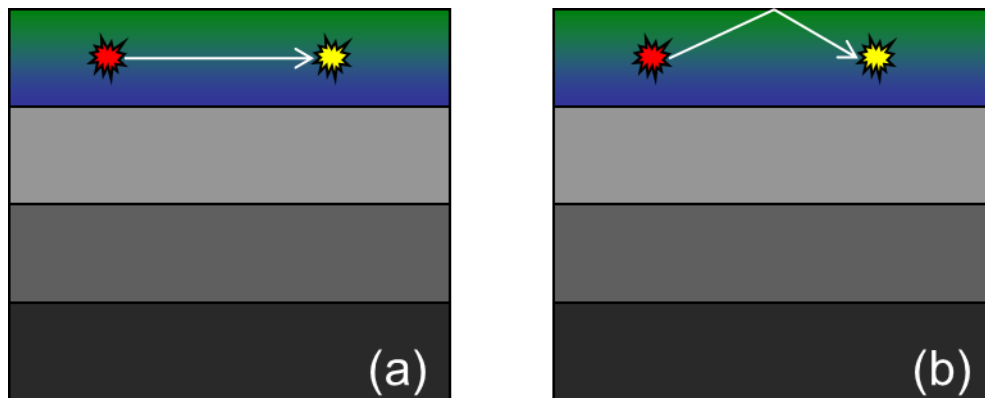


Figure 1.2: Examples of the direct-arrival and the direct-arrival ghost (modified from Weglein and Dragoset, 2005). (a) The path of the direct arrival. (b) The path of the direct-arrival ghost. The blue-green area represents the water layer. The red and yellow dots indicate the positions of seismic sources and receivers, respectively. The white lines are raypaths of the events being defined.

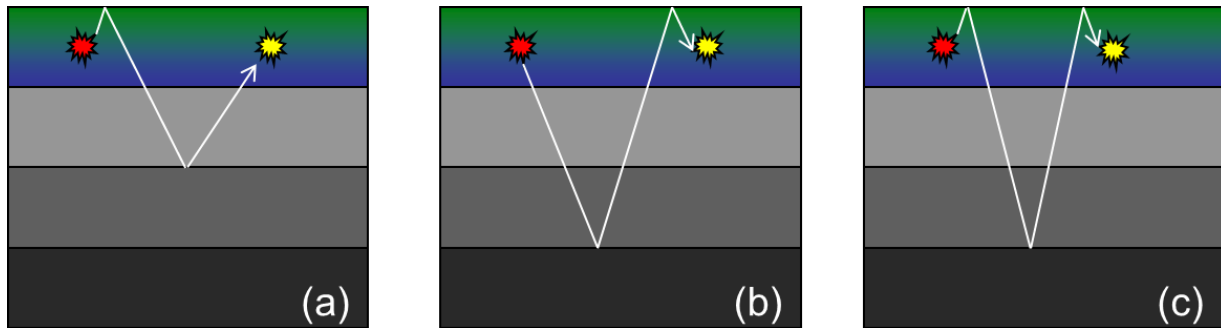


Figure 1.3: Ghost events that move upward from the source and/or downward to the receiver, and interact with the free-surface (modified from Weglein and Dragoset, 2005). (a) The source ghost; (b) the receiver ghost; (c) the source-receiver ghost.

Generally, multiple reflections are considered as noise. However, for some inversion methods (e.g. least-squares inversion) multiples can be considered as signals (Lines, 1996). Primary reflections are the only events that are always considered to be signals (Figure 1.4). Primaries are events that have experienced one upward reflection and no downward reflections. Multiple reflections have two or more upward reflections and they occur when there are strong impedance contrasts between subsequent layers. There are two major types of multiple: free-surface multiple (FSM) and internal multiple. A multiple with at least one downward reflection at the free-surface is called a free-surface multiple (FSM) and they are classified by how many times they reflect off the free-surface (Figure 1.5). A FSM that reflects once from the free-surface is a first-order FSM; a FSM that reflects twice from the free-surface is second order and so on. Events consist of at least one downward reflection in the subsurface, and never interact with the free-surface, are called interbed or internal multiples. Internal multiples are classified by how many times they reflect downwards (Figure 1.6). Note that no matter how many subsurface reflections it undergoes, if it ever hits the free-surface, it is a FSM (see for instance in Figure 1.5 (a)).

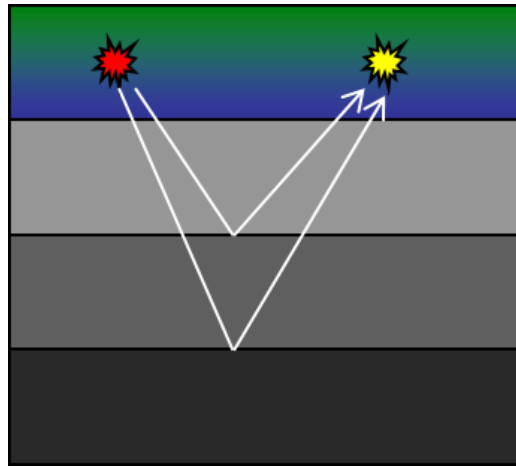


Figure 1.4: Illustration of primary reflections (modified from Weglein and Dragoset, 2005).

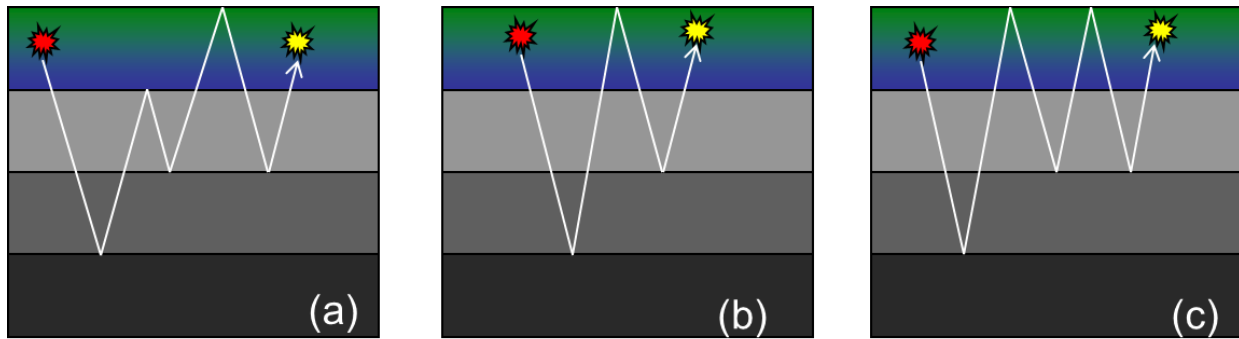


Figure 1.5: FSMs (modified from Weglein and Dragoset, 2005). (a) A FSM reflection; (b) first-order FSM reflects once from the free-surface; (c) second-order FSM reflects twice from the free-surface.

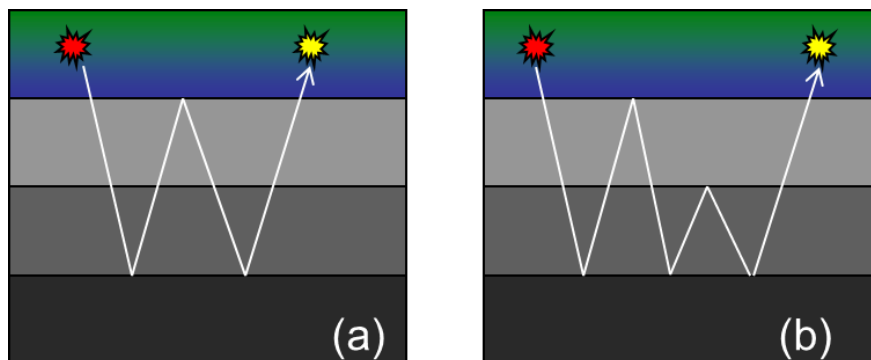


Figure 1.6: Internal multiples (modified from Weglein and Dragoset, 2005). (a) A first-order internal multiple; (b) a second-order internal multiple.

1.3.2 Scattering theory

The scattering theory describes the relationship between the physical properties of an actual medium, the physical properties of a reference medium, and the impulse response for the actual and reference media (Weglein et al., 1997). This theory provides the foundation for the forward scattering series and the inverse scattering series. The forward scattering series is a basis for modelling events, and the inverse scattering series is a basis for processing events (Weglein and Dragoset, 2005). Both are generalized Taylor series that have provided new methodologies for removing FSMs and internal multiples.

The basic concept of the theory will be shown in this section. Assuming we have a medium through a wavefield, G , which is propagating because of a source disturbance, δ . The equation that describes the propagation is

$$LG = \delta, \quad (1.1)$$

where L is a differential operator that is a function of the properties of the medium. This equation is difficult to solve in a straightforward manner, a simpler equation is introduced:

$$L_0 G_0 = \delta, \quad (1.2)$$

where G_0 is the wavefield that propagates through a reference medium, and L_0 is the differential operator for the medium. An assumption that all properties affecting the acoustic propagation in this medium are constant is applied. The perturbation operator V and the scattered field G_s are defined as

$$V = L - L_0, \quad (1.3)$$

and

$$G_s = G - G_0, \quad (1.4)$$

respectively. The Lippmann-Schwinger equation is an operator identity that relates the actual and reference wavefield propagation to the difference between the actual and reference media, V (see Taylor, 1972) as

$$G_s = G - G_0 = G_0 V G. \quad (1.5)$$

The above equation can provide an iterative solution for G_s in terms of G_0 and V .

$$G_s = G_0 V G_0 + G_0 V G_0 V G_0 + \dots = (G_s)_1 + (G_s)_2 + \dots, \quad (1.6)$$

where $(G_s)_n$ is an n th-order function of V . Equation 1.6 is a forward series which models a scattered field in terms of reference wavefield propagation and perturbation operator V .

The inverse scattering series, which is similar to the forward scattering series in equation 1.6, expresses V as a power series that is a function of measured data, D :

$$V = V_1 + V_2 + V_3 + \dots, \quad (1.7)$$

where V_n is the portion of V that is an n th-order function of the data, D . Substituting equation 1.7 into equation 1.6, evaluating it on the measurement surface, and then equating equal orders in the data, we obtain:

$$D = G_0 V_1 G_0 \quad (1.8)$$

$$G_0 V_2 G_0 = -G_0 V_1 G_0 V_1 G_0 \quad (1.9)$$

$$G_0 V_3 G_0 = -G_0 V_1 G_0 V_1 G_0 V_1 G_0 - G_0 V_1 G_0 V_2 G_0 - G_0 V_2 G_0 V_1 G_0. \quad (1.10)$$

⋮

Equation 1.8 is the linear form and allows V_1 to be determined from the data D . V_2 is computed from V_1 in equation 1.9, and V_3 in equation 1.10 is determined from V_1 and V_2 . This process continues until the entire series for V is constructed. This procedure for solving V does not require any a priori subsurface information; therefore, the inverse scattering series allows removal of internal multiples when a priori information is not available.

1.3.3 Internal multiple prediction algorithms

Weglein et al. (2003) described the inverse scattering series as “a comprehensive seismic data processing tool from which distinct task-specific subseries can be isolated to perform specific tasks”. The inverse scattering series internal multiple attenuation algorithm was introduced to geophysics literature in the 1990s by Araújo et al. (1994) and Weglein et al. (1997). The two key characteristics of the inverse scattering series based method are: it does not require any a priori information from the subsurface, and it will compute first-order internal multiples from all possible generators with accurate times and approximate amplitudes. Furthermore, the primary reflections are not affected by this algorithm. The output of the algorithm is a dataset containing the predicted internal multiples. In this section, internal multiple prediction algorithms in 1D, 1.5D and 2D will be introduced.

1.3.3.1 Internal multiple prediction in 2D

The 2D prediction algorithm (Weglein et al., 1997) is

$$PRED(k_g, k_s, \omega) = \left(\frac{1}{2\pi}\right)^2 \int_{-\infty}^{\infty} \int_{-\infty}^{\infty} dk_1 dk_2 \times \Gamma(k_g, k_1, k_2, k_s | \epsilon), \quad (1.11)$$

where

$$\Gamma(k_g, k_1, k_2, k_s | \epsilon) = \int_{-\infty}^{\infty} dz e^{i(q_g + q_1)z} b_1(k_g, k_1, z) \int_{-\infty}^{z-\epsilon} dz' e^{-i(q_1 + q_2)z'} b_1(k_1, k_2, z') \int_{z'+\epsilon}^{\infty} dz'' e^{i(q_2 + q_s)z''} b_1(k_2, k_s, z''), \quad (1.12)$$

and the

$$q_x = \frac{\omega}{c_0} \sqrt{1 - \frac{k_x^2 c_0^2}{\omega^2}} \quad (1.13)$$

are vertical wavenumbers associated with the various lateral wavenumbers k_x , the reference velocity c_0 and temporal frequency ω . b_1 is the input to the prediction algorithm, which is defined in terms of the original pre-stack data with FSMs eliminated. The search limiting parameter epsilon (ϵ) is related to the width of the wavelet and z , z' and z'' are pseudo-depth positions defined by $z = c_0 t / 2$.

1.3.3.2 Internal multiple prediction in 1D

The 2D prediction algorithm can be reduced to 1D, using the replacement

$$k_g = k_s = 0. \quad (1.14)$$

Then the prediction algorithm for the 1D normal incidence case can be obtained,

$$PRED(\omega) = \int_{-\infty}^{\infty} dz e^{i2\frac{\omega}{c_0}z} b_1(z) \int_{-\infty}^{z-\epsilon} dz' e^{-i2\frac{\omega}{c_0}z'} b_1(z') \int_{z'+\epsilon}^{\infty} dz'' e^{i2\frac{\omega}{c_0}z''} b_1(z''). \quad (1.15)$$

The basis of the prediction is a set of three nested integrals over pseudo-depth. The 1D algorithm requires one such set for each output frequency ω . The 2D algorithm requires many such sets, the nested integration is repeated for every value of the integration variables k_1 and k_2 for every

frequency, over which the results are summed (Innanen, 2012). Then this repeats for all output k_g and k_s pairs.

1.3.3.3 Internal multiple prediction in 1.5D

If the data have offset but the earth is nearly layered, computationally simple 1.5D form of the algorithm can be used. In these cases, contributions to multiples only arise from lateral source and receiver wavenumber values

$$k_g = k_s . \quad (1.16)$$

The general 2D form of the prediction algorithm becomes

$$PRED(k_g, \omega) = \int_{-\infty}^{\infty} dz e^{ik_z z} b_1(k_g, z) \int_{-\infty}^{z-\epsilon} dz' e^{-ik_z z'} b_1(k_g, z') \int_{z'+\epsilon}^{\infty} dz'' e^{ik_z z''} b_1(k_g, z''), \quad (1.17)$$

where $k_z = 2q_g$ and

$$q_g = \frac{\omega}{c_0} \sqrt{1 - \frac{k_g^2 c_0^2}{\omega^2}} , \quad (1.18)$$

is the vertical wavenumber calculated from the lateral wavenumber, the reference velocity and the frequency. Compared to the 2D algorithm (see equation 1.12), the 1.5D computational cost is significantly reduced and is faster because fewer wavenumber combinations are required in the calculation.

1.3.4 Lower-higher-lower relationship

In the equations above, the internal multiple prediction algorithms predict internal multiples based on the convolution and correlation of the data. Figure 1.7 is an example of a construction of the travel times of an internal multiple. The red primary has travel time t_1 , the green primary

has travel time t_2 , and the dashed line primary has travel time t_3 . The travel time of the internal multiple is equal to $t_1 + t_2 - t_3$. In this example, the sums and differences of travel times produce internal multiple travel times, but not all combinations of sums and differences do. Figure 1.8 shows internal multiple being computed from two combinations of sums and differences; the first combination worked, whereas the second case produces spurious events that does not correspond to any physical event.

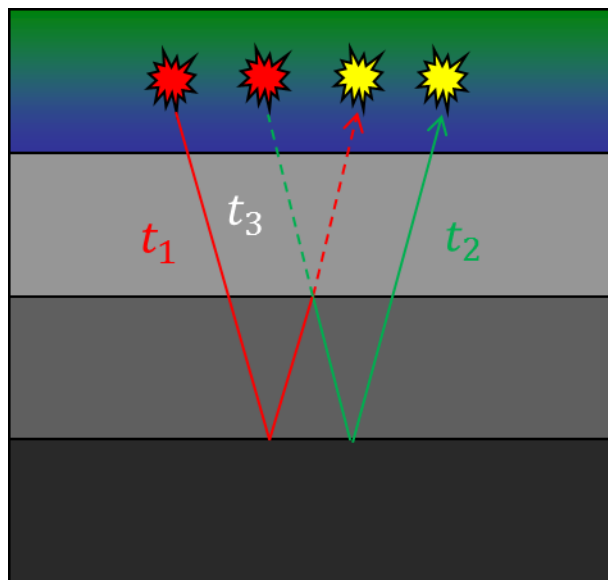


Figure 1.7: Construction of the travel times of an internal multiple.

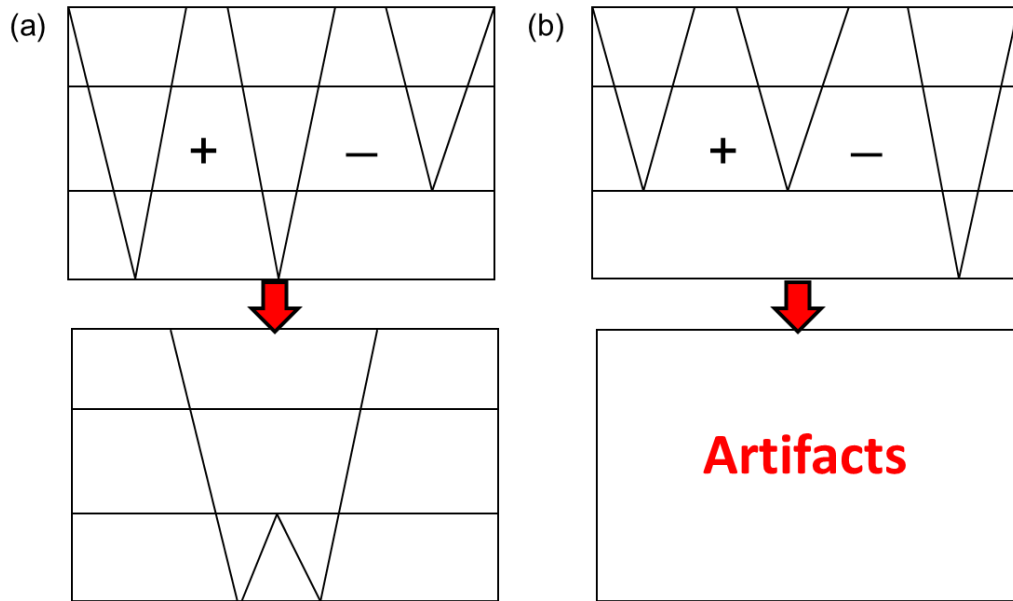


Figure 1.8: Two combinations of sums and differences of primary travel times. In (a) the combination of sums and difference produces an internal multiple, whereas in (b) it produces artifacts that does not correspond to any physical event.

In fact, artifacts come from subtraction of travel times which are larger than those being summed. Changes can be applied to the internal multiple prediction algorithms to limit the size of the event being subtracted. For example, the 1D algorithm (equation 1.15) can be expressed in pseudo-depth, $z = c_0 t / 2$, instead of time; the subtraction of larger travel times is prevented by disallowing subtraction of “lower” events. The trace whose events are to be subtracted is the middle one $b_1(z')$ because this event is incorporated through correlation (a ‘-’ sign in the Fourier kernel). Values obtained from the middle integral of events in this trace that are “higher” than the two traces $b_1(z)$, and $b_1(z'')$ are used, whereas “lower values” are discredited. To achieve this, the three events ($b_1(z)$, $b_1(z')$ and $b_1(z'')$) need to satisfy $z'' > z'$ and $z > z'$. Therefore, the z'' integration can be restricted so that it begins at z' . By the same principle, the z' integration can be restricted such that it ends at z , disallowing contributions from any z' value greater than z .

(Innanen, 2011). The search-limiting parameter ϵ is included to prevent intra-event prediction from happening. For band-limited data, ϵ is different for every dataset and is related to the width of the wavelet.

1.4 1D example

1.4.1 Subevent interpretation of internal multiples

In this section, the inverse scattering series based internal multiple attenuation algorithm is demonstrated using the concept of subevents. This reproduces the results of Weglein and Matson (1998), and allows essential concepts of internal multiple prediction to be clearly discussed.

Figure 1.9 shows a simple model in which an internal multiple is generated (blue ray path) from the convolution and correlation of the three subevents.

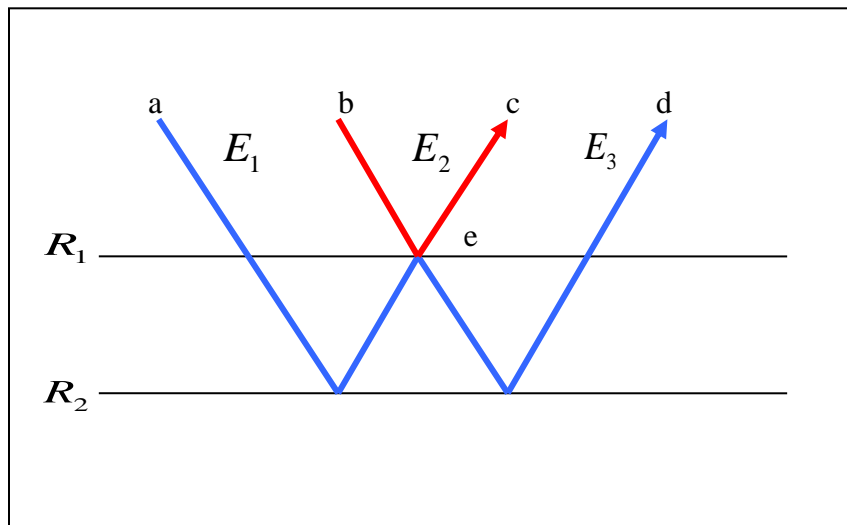


Figure 1.9: Construction of an internal multiple using subevents (modified from Weglein and Matson, 1998). The first subevent is a primary reflection that travels from point ‘a’, reflected from the second reflector, and is received at point ‘c’. The second subevent is a primary that propagates from point ‘b’, reflected from the first interface ‘e’, and received at point ‘c’. The third one is a primary from point ‘b’ to ‘d’, reflected from the second interface.

The first subevent in Figure 1.9 is

$$E_1(\omega) = T_{01}R_2T_{10}e^{i\omega t_2}, \quad (1.19)$$

which is a primary reflection that propagates from a source at ‘a’, reflected from the second reflector, and is measured at ‘c’. The second subevent is a primary that propagates from ‘b’ to ‘c’, reflected from the first reflector which is ‘e’,

$$E_2(\omega) = R_1e^{i\omega t_1}, \quad (1.20)$$

The third one propagates from ‘b’, reflected from the second interface, and is measured at ‘d’,

$$E_3(\omega) = T_{01}R_2T_{10}e^{i\omega t_2}. \quad (1.21)$$

The internal multiple attenuation algorithm predicts an internal multiple from these subevents by performing a convolution and a correlation. Substituting the three subevents in pseudo-depth into equation 1.15, the result is:

$$PRED(k_z) = \int_{-\infty}^{\infty} dz e^{ik_z z} E_1(z) \int_{-\infty}^{z-\epsilon} dz' e^{-ik_z z'} E_2(z') \int_{z'+\epsilon}^{\infty} dz'' e^{ik_z z''} E_3(z''), \quad (1.22)$$

where $k_z = 2\omega / c_0$ is the vertical wavenumber, which is the conjugate of the pseudo-depth. The integration limits may be extended to $\pm\infty$ because the three subevents are discrete localized events and satisfy the conditions that $z'' > z'$ and $z > z'$. The equation can be written as

$$PRED(k_z) = \int_{-\infty}^{\infty} dz e^{ik_z z} E_1(z) \int_{-\infty}^{\infty} dz' e^{-ik_z z'} E_2(z') \int_{-\infty}^{\infty} dz'' e^{ik_z z''} E_3(z''). \quad (1.23)$$

Applying the Fourier transform to the above equation changing to the frequency domain, the equation becomes:

$$PRED(\omega) = E_1(\omega)E_2(-\omega)E_3(\omega). \quad (1.24)$$

This equation describes the correlation of subevent 1 with subevent 2 followed by a convolution with subevent 3. Substituting the three subevents into equation 1.24 gives

$$PRED(\omega) = R_1 R_2 T_{01}^2 T_{10}^2 e^{i\omega(2t_2 - t_1)}. \quad (1.25)$$

The actual internal multiple in the frequency domain is written as

$$ACT(\omega) = T_{01} R_2 (-R_1) R_2 T_{10} e^{i\omega(2t_2 - t_1)}. \quad (1.26)$$

Comparing equations 1.25 and 1.26, the predicted amplitude is always less than the actual internal multiple. The difference occurs because the actual multiple does not experience a transmission loss at the downward reflection point ‘e’, whereas the internal multiple algorithm models the multiple from subevents that have experienced a transmission loss at point ‘e’. This difference is a factor known as the attenuation factor of the predicted internal multiple ($T_{01}T_{10}$).

Weglein and Matson (1998) pointed out that the attenuation factor could result from the leading order term in the internal multiple attenuation series not properly taking account transmission effects. For typical earth velocities, this attenuation factor is very small and the predicted multiples from the prediction algorithm give satisfactory results (Hernandez, 2012).

For time prediction, the prediction algorithm takes the time of the first event, plus the time of the third event minus the time of the second event. This subtraction can be seen in the negative phase of the second depth integral in equation 1.22. This process gives the correct arrival time and phase (Ramirez and Weglein, 2005).

1.4.2 1D numerical example

A simple case of 1D internal multiple prediction is shown in this section. Three primaries and two associated first-order internal multiples are generated and plotted for a three interface velocity model (Figure 1.10). The internal multiple prediction algorithm is implemented and the

results are plotted in Figure 1.11. Table 1.1 illustrates the detail information of this synthetic model.

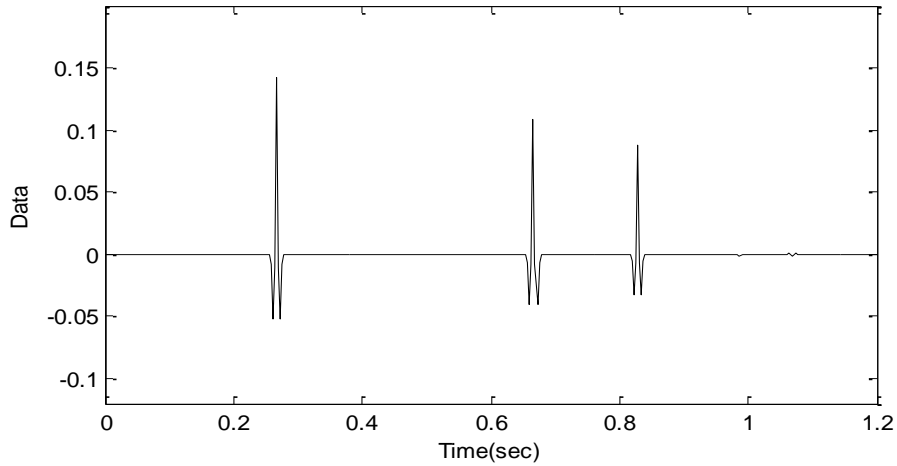


Figure 1.10: A numerical example of 1D internal multiple prediction. The zero-offset trace with three primaries and two associated first-order internal multiples. The arrival times for the two internal multiples are $t_1 = 0.98s$ and $t_2 = 1.07s$, respectively.

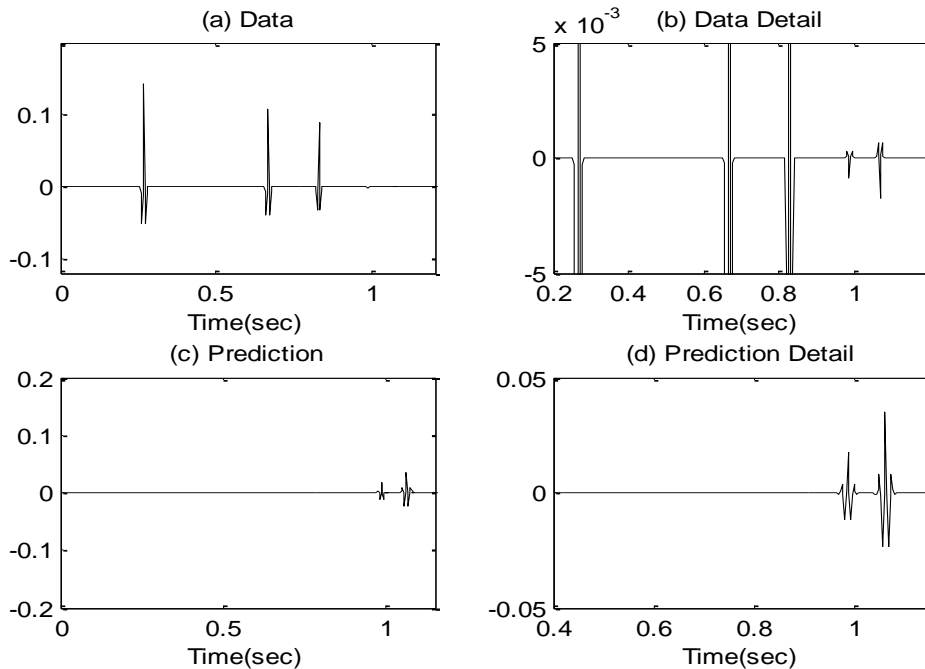


Figure 1.11: Applying the 1D internal multiple attenuation algorithm to the synthetic model. (a) Input data; (b) input data with focus on internal multiples; (c) prediction output; (d) prediction output with focus on internal multiples.

Table 1.1: Parameters of the synthetic model

Parameter	Value
Sample number	512
Interval sample time	3 ms
Velocity and depth of the first interface	2000 m/s at 200 m
Velocity and depth of the second interface	2500 m/s at 600 m
Velocity and depth of the third interface	3000 m/s at 800 m
Wave speed of the source/receiver medium	1500 m/s
Type of wavelet	Ricker
Optimum epsilon (ϵ)	7 ms
Wavelet central frequency	80 Hz

The search-limiting parameter ϵ value is listed here, as several values of ϵ are tested with the optimal value shown to be 7 ms. For smaller ϵ values, artifacts will be seen at the arrival times of primaries in the output data. While larger ϵ values could damage important information (e.g. internal multiples) present in the output data. The output data will not show any events at all if the overestimation of ϵ is too large.

1.5 Thesis overview

This thesis is presented in 6 chapters. Chapter 2 continues the study by Hernandez (2012) and presents a systematically study of how the presence offset and the existence of dipping angle in the reflectors affect the 1D internal multiple prediction algorithm. Chapter 3 to Chapter 5 will examine three case studies of 1.5D internal multiple prediction. The main objective of this thesis is to examine the efficiency of the 1.5D version of the inverse scattering series internal multiple prediction algorithm for various datasets.

In Chapter 3 the prediction procedure is introduced using a synthetic dataset and the effect of variation of the search-limiting parameter ϵ is analyzed. Large-dip artifacts are also discussed and they can be mitigated by the employment of a k_g -dependent integration-limiting parameter ϵ .

In Chapter 4 the acquisition, processing and multiple prediction procedures of a physical modelling dataset are illustrated. This dataset is acquired by University of Calgary Seismic Physical Modelling Facility, the benefits of which are controlled acquisition geometry and physical model properties.

In Chapter 5 the Hussar dataset is introduced. The synthetics are acquired by blocking the well 12-27 with different depth steps. Prestack data are analyzed with the 1.5D version of the algorithm, in particular with an eye for the success with which the multiples reverberating in the relatively thin-layering of the blocked log model can be predicted, and for the influence of realistic offsets on the generation of far-offset artifacts in the prediction. Finally, in Chapter 6 the conclusions from Chapters 2 to 5 are summarized.

1.6 Hardware and software

The physical modelling experiment presented in this thesis was done using the Seismic Physical Modelling Facility operated by the Consortium for Research in Elastic Wave Exploration Seismology (CREWES) project of the Department of Geoscience at the University of Calgary. The physical modelling data were acquired by Dr. Joe Wong with the assistance of Mr. Kevin Bertram. The author was involved in the majority of geometry design, acquisition and processing

procedures. The computer software used to run the physical modelling machine was written by Dr. Joe Wong and operated by Mr. Kevin Bertram.

The main software used in this thesis is MATLAB® which is a high-level programming language developed by MathWorks. This software is optimized for matrix algebra making it ideal for seismic data. A toolbox developed by CREWES with a variety of processing, modelling and utility functions that can be used for seismic data processing was used extensively in this thesis. The 1.5D version of internal multiple prediction algorithms will be available in the toolbox in 2015. The other software used in this thesis is ProMAX® developed by Landmark which contains intuitive analysis tools, state-of-the-art geophysical algorithms and an optimized parallel infrastructure. This software was used for the purpose of processing the physical modelling data. Microsoft Office 2010 software was used for the editing and assembling of this thesis.

Chapter Two: 1D internal multiple prediction

2.1 Chapter overview

In this chapter, a 1D version of the internal multiple prediction algorithm developed by Weglein and collaborators in the 1990s is analyzed. An important advantage of the 1D algorithm as compared to the 1.5D, 2D and 3D versions is its fast computation time but it is more prone to errors with increasing reflector dip and offset. The 1D algorithm was tested on synthetic datasets with dipping reflectors and different offsets. The effectiveness of this algorithm was determined by the rate of percent error increase with increasing dip and offset. Recommendations for ranges of reflector dips and ratios of offset to generator depths suitable for the 1D internal multiple prediction algorithm were made based on the results.

2.2 Synthetic example

The acoustic finite difference forward modelling codes developed by CREWES (www.crewes.org) were used to create a velocity model and a shot record to test the 1D internal multiple prediction. The velocity model is shown in Figure 2.1 and the shot record built from the velocity model is shown in Figure 2.2 (a). The zero-offset trace from this shot record is illustrated in Figure 2.2. The boundary conditions were set to be absorbing for all four sides to avoid FSMs. The data were generated with lowcut, lowpass, highpass and highcut frequencies of 10 Hz, 20 Hz, 80 Hz and 100 Hz, respectively. The parameters of this synthetic dataset are listed in Table 2.1.

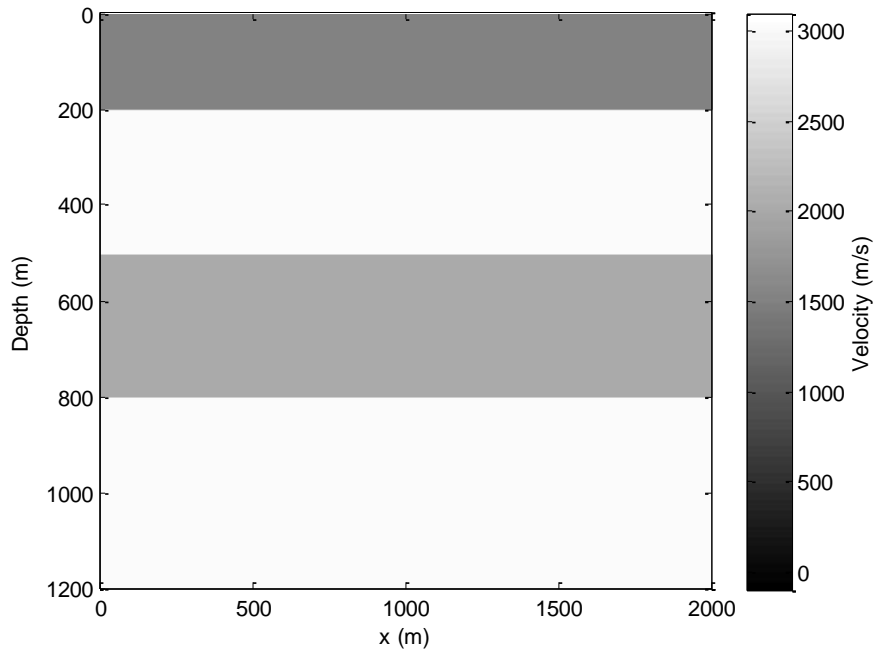


Figure 2.1: Four-layer velocity model.

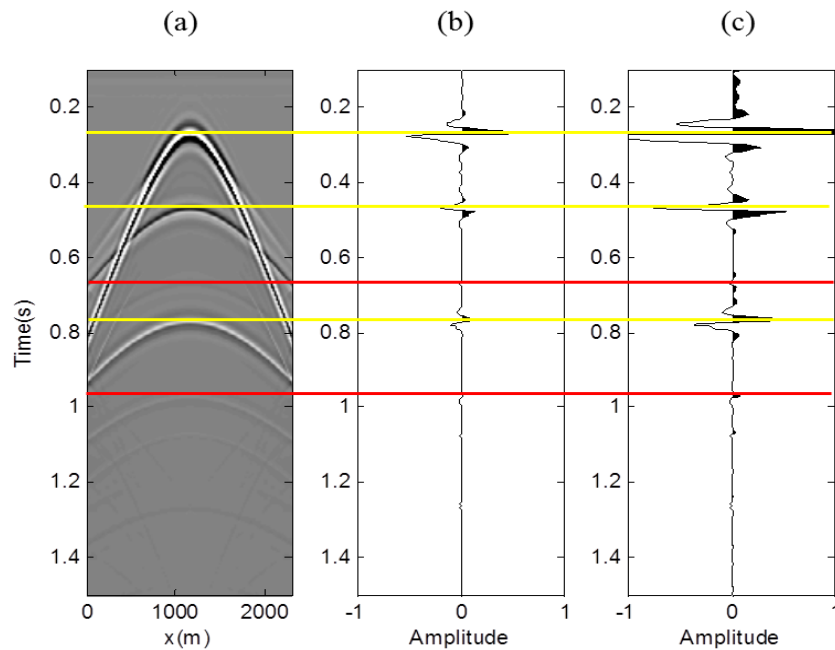


Figure 2.2: (a) Shot record of the model with the direct wave removed. (b) Zero-offset trace. (c) The same trace as (b) with a larger scale. Yellow lines show the positions of primaries, and red lines indicate the positions of internal multiples.

Table 2.1: Parameters of the velocity model and shot record

Parameter	Value
Number of t	1024
Number of x	1024
Number of z	1024
Interval sample time	3 ms
Velocity and depth of the first interface	3000 m/s at 200 m
Velocity and depth of the second interface	2000 m/s at 500 m
Velocity and depth of the third interface	3000 m/s at 800 m
Wave speed of the source/ receiver medium	1500 m/s
Time step	0.4 ms
Maximum time of the shot record	3 s
Location of the source	(1, 512)
Frequency band	[10 20 80 100] Hz
Optimum epsilon (ϵ)	60 ms

Traces from this shot record were input into the internal multiple prediction algorithm. The 1D internal multiple algorithm is expected to accurately predict multiple arrival times at zero-offset trace (in the center of the shot record). Several tests were made with the zero-offset trace to determine the optimum ϵ value of 60 sample points. Artifacts from poorly chosen ϵ values often occurred at the arrival times of the primaries in the output. Figure 2.3 illustrates the result of applying the 1D algorithm on the zero-offset trace. The red circles indicate the positions of the internal multiples in the input and output data. The travel times of the two dominant internal multiples are $t_1 = 0.67$ s and $t_2 = 0.97$ s. The ray paths for those two internal multiples are shown in Figure 2.4. There are two superimposed events labelled peg-leg multiple IM2, which have

different paths but the same arrival times. With this benchmark test in place and an optimum ϵ value determined, the offset tests are ready to proceed.

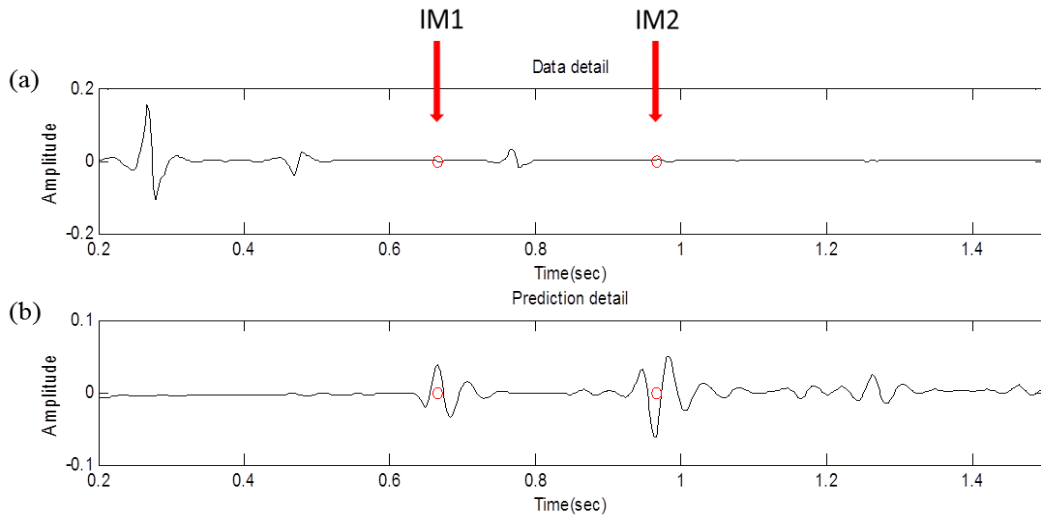


Figure 2.3: Application of the 1D internal multiple prediction algorithm to the zero-offset trace. (a) Input data. (b) Prediction output. The red circles indicate the positions of the internal multiples in the input and output data.

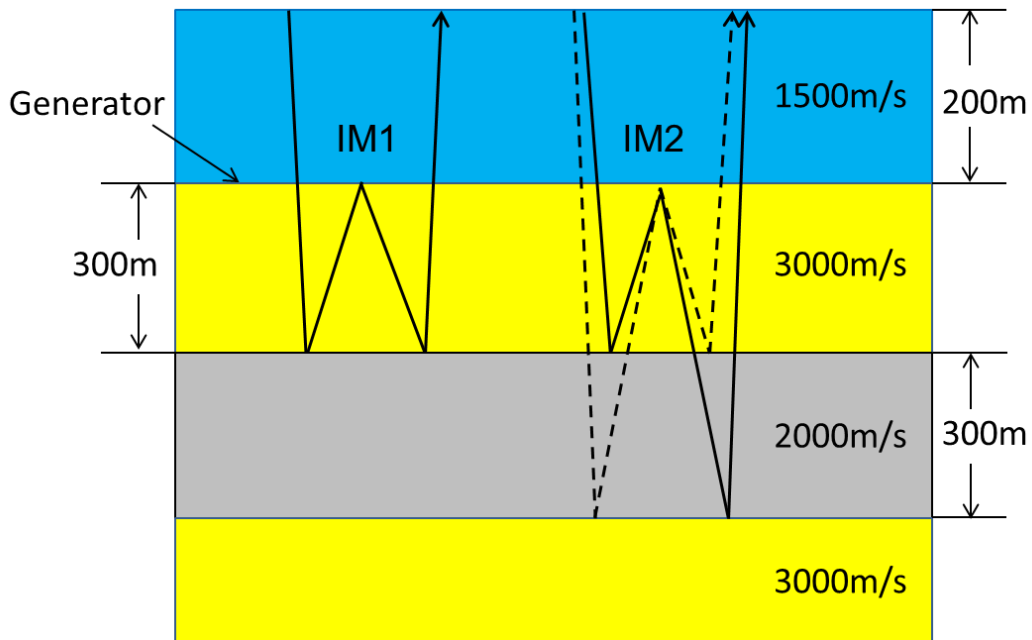


Figure 2.4: The ray paths of the two dominant internal multiples.

2.3 Systematic study of prediction errors

2.3.1 The influence of offset

The errors produced in the prediction of internal multiples 1 and 2 were measured with increasing offset of the input trace. The relative travel time errors between predicted and actual multiples (referred to hereafter as “prediction errors”) were picked manually. The increase in prediction errors is proportional to the increase in offset (Figure 2.5). At an offset of 360 m, 1.8 times the depth of the generator (200 m), the prediction errors are above 8% for the first internal multiple and 6% for the second internal multiple. At 300 m offset, 1.5 times the depth of the generator, both internal multiple errors are less than 5%. This can be a qualitative threshold below which the error level is acceptable.

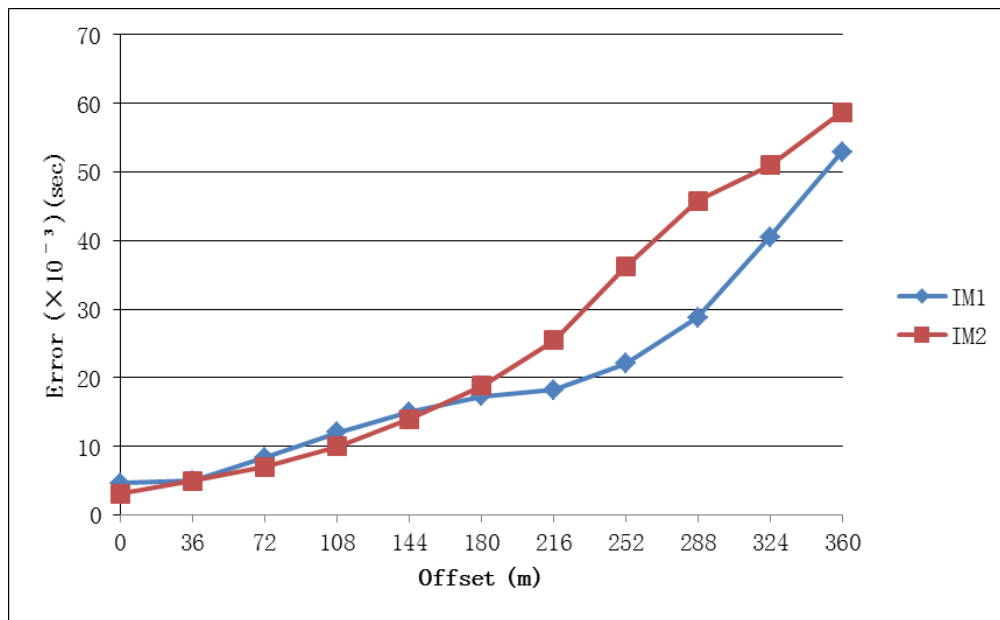


Figure 2.5: The relative travel time errors between predicted and actual multiples plotted against increasing offset.

2.3.2 The influence of dipping angles

Next, the prediction errors from the zero-offset trace taken from dipping interfaces were analyzed. The dip angles were increased gradually from 0 to 15 degrees. The three cases examined were:

- (1) where the first interface (i.e., the generator) is the dipping interface;
- (2) where the second interface is the dipping interface;
- (3) where the third interface is the dipping interface.

2.3.2.1 Case I

In the first case, the generator is the dipping interface. In Figure 2.6, the blue line is the prediction errors of the internal multiple 1 and the red line is the prediction errors of the internal multiple 2. All errors are within 1% in the dipping angle range of 0 to 10 degrees and there is a sharp increase at dipping angles greater than 10 degrees. This suggests that when the first interface is the dipping interface, the algorithm will yield acceptable results in the range of 0 to 10 degrees.

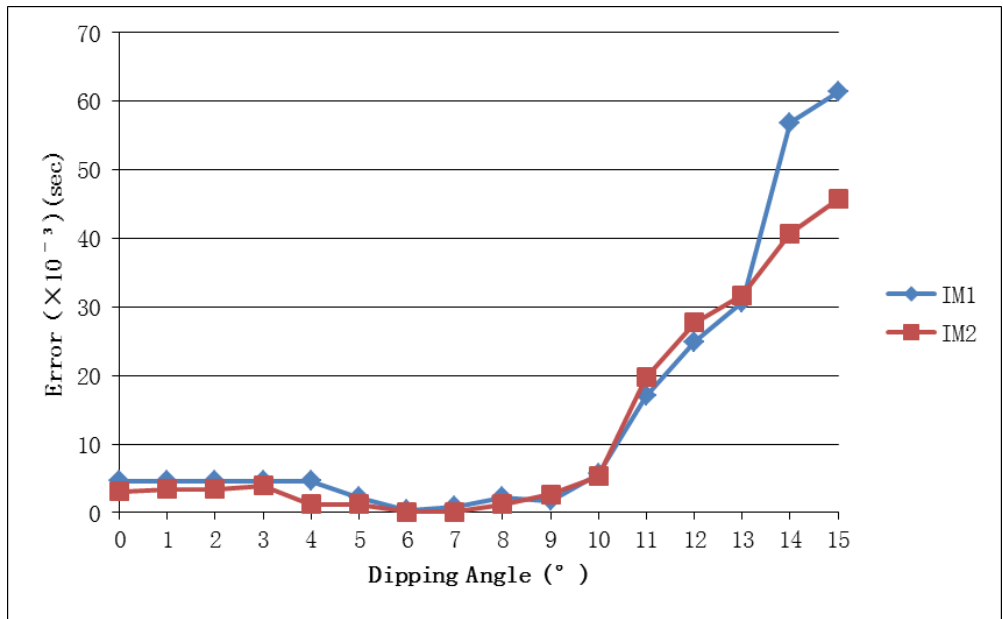


Figure 2.6: The relative travel time errors between predicted and actual multiples in the zero-offset trace plotted against an increasing series of dipping angles, with the generator as the dipping interface.

2.3.2.2 Case II

Case II examined the effects of the second interface as the dipping interface. In Figure 2.7, larger fluctuations are present in the first internal multiple as compared to the second internal multiple. This implies that a dipping second interface has greater effects on the first internal multiple. Errors of internal multiple 1 are within 1% for the range of 0 to 11 degrees, and increase sharply after. Errors of internal multiple 2 remain within 1% for the range of 0 to 15 degrees.

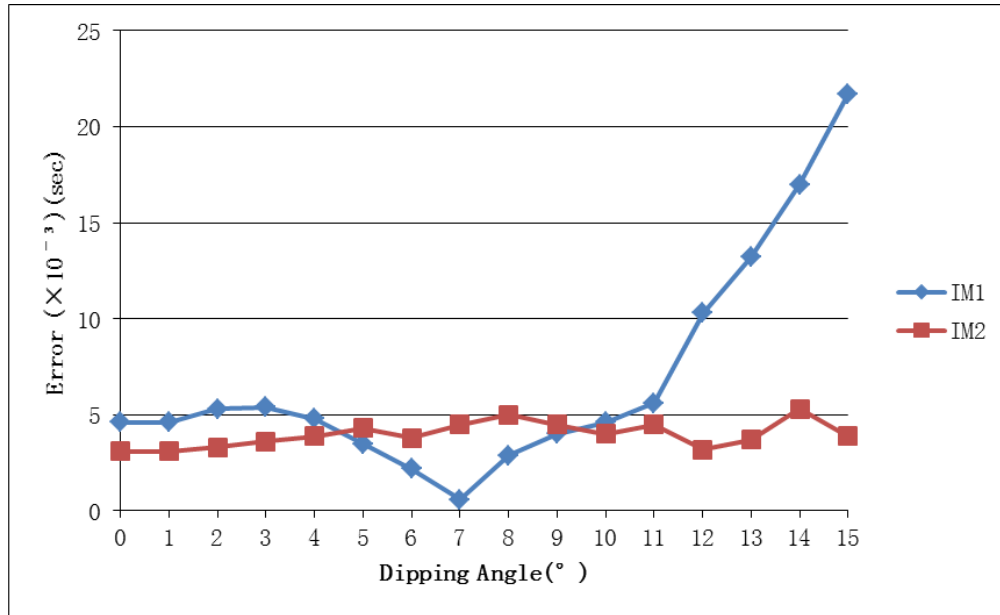


Figure 2.7: The relative travel time errors between predicted and actual multiples in the zero-offset trace plotted against an increasing series of dipping angles, with the second interface as the dipping interface.

2.3.2.3 Case III

The third case examined the effects of the third interface as the dipping interface. In Figure 2.8, the prediction errors of the first internal multiple remain constant with increasing dipping angle of the third interface and the positions of the first internal multiple are unaffected. The second internal multiple prediction errors decrease with increases in the dipping angle up to 10 degrees, and sharply increase after. However, errors are within 1% for dipping angles of 0 to 15 degrees, therefore, indicating a negligible influence on the algorithm for 0 to 15 degrees range of dipping angles.

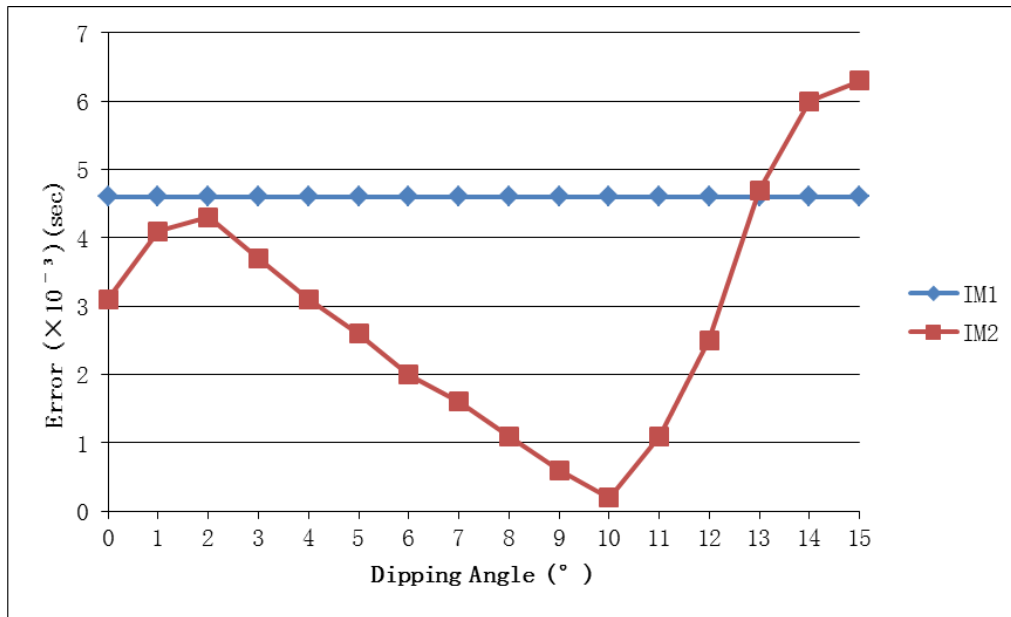


Figure 2.8: The relative travel time errors between predicted and actual multiples in the zero-offset trace plotted against an increasing series of dipping angles, with the third interface as the dipping interface.

2.4 Towards making practical recommendations

The 1D internal multiple prediction algorithm based on the inverse scattering series has been investigated in situations where the seismic data require higher dimensional versions of the algorithm. If the acceptable error range is set to be 5%, horizontal reflectors with offset greater than 1.5 times the generator depth will generate unacceptable errors. The influence of dipping angles on the prediction algorithm was tested on the zero-offset trace and the results can be applied to relatively near-offset cases. The algorithm is most affected when the generator is the dipping interface. In this case, the error is above the chosen threshold of 1% when the dipping angle exceeds 10 degrees. In the case where the second interface is the dipping interface, the measured error exceeds 1% at dipping angles greater than 11 degrees. Lastly, when the third interface is the dipping interface, the error crosses the threshold at dipping angles greater than 15

degrees. These cases suggest that, 10 degrees is a reasonable upper limit to generate acceptable results.

What could be done with these results? For any particular seismic dataset, given sufficient prestack data coverage, the prediction errors mentioned above can be avoided by using 1.5D, 2D, or 3D versions of the algorithm. The 1D version runs more quickly than higher dimensions algorithms, so it may be valuable to derive as much information as possible from the 1D algorithm prior to using other versions. Our results can provide general recommendations about when the use of the 1D algorithm is appropriate.

2.5 Chapter summary

The 1D internal multiple algorithm was studied. Internal multiples from possible generators were computed and shown in the output. The performance of the 1D algorithm was demonstrated using different synthetic datasets and some recommendations for the application of this method were given based on the results.

We do not recommend this method when offset is greater than 1.5 times generator depth. This theory is based on a flat layered structure but the result of small dipping angle interface is also acceptable. All multiple predications are within a reasonable error range (<1%) for dipping angles less than 10 degrees. The main priority for future research is to move beyond the arbitrary choice of allowable error level. A possible way to achieve this goal is to quantify the error by studying the effects on adaptive subtraction of increasing travel time shift between predicted and measured multiples.

Chapter Three: Numerical analysis of 1.5D internal multiple prediction

3.1 Chapter overview

In this chapter, a 1.5D (i.e., pre-stack data over a layered geology) version of the inverse scattering series internal multiple prediction algorithm is examined. For modern processing tools (such as full waveform inversion (FWI), AVO and amplitude-variation-with-azimuth (AVAZ) analysis, etc.), it is important to analyze the effectiveness of multiple attenuation on prestack data (Ikelle et al., 1997). The prediction operation is discussed, and the procedure is illustrated with a prestack synthetic example. The effect of variation of the search-limiting parameter ϵ is more complicated in 1.5D than it is in 1D. This was numerically investigated with the ultimate aim of finding an efficient method of choosing the optimum ϵ value. The effect on prediction accuracy of dipping interface was analyzed. Large-dip artifacts, noticeable in unfiltered 1.5D internal multiple predictions were identified, and they can be mitigated by implementing a k_g -dependent integration-limiting parameter ϵ .

3.2 Synthetic example

3.2.1 Velocity model and shot record

The 1.5D internal multiple prediction algorithm was applied on synthetic data, generated by the finite difference method using a four-layer velocity model (Figure 3.1). The parameters of this synthetic dataset are listed in Table 3.1. A single shot record is illustrated in Figure 3.2 with three primaries indicated by yellow lines and two internal multiples indicated by red lines. The goal is to use the primaries (Figure 3.2 (a)) as subevents to predict the two internal multiples (Figure 3.2 (b)) at all offsets. A fourth order acoustic finite difference forward modelling algorithm was implemented (see www.crewes.org) to create the data. Absorbing boundary conditions were

applied to all four sides to avoid FSMs. The receiver spacing was 10 m, the record length is 3 s, and the sampling rate was 2 ms. The data were generated with lowcut, lowpass, highpass and highcut frequencies of 5 Hz, 10 Hz, 30 Hz and 40 Hz, respectively. Also, the direct wave was removed because the algorithm only requires the upgoing wavefield to be measured at the geophones. Deconvolution and deghosting are useful steps in pre-processing, but they can be neglected if the internal multiples are resolvable in the dataset without these steps.

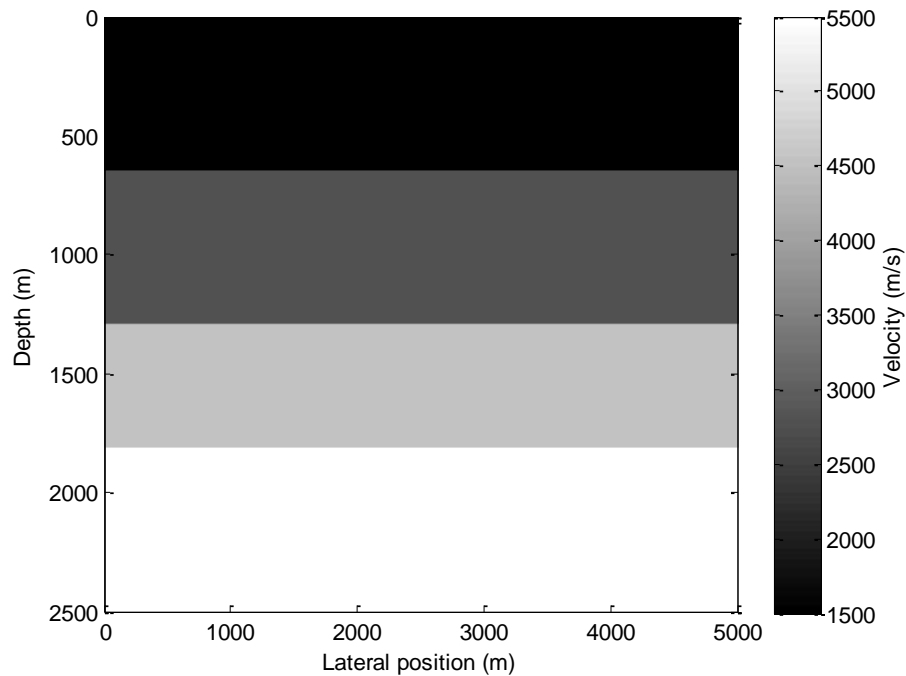


Figure 3.1: Four-layer velocity model used to generate synthetic data to test the 1.5D internal multiple prediction algorithm.

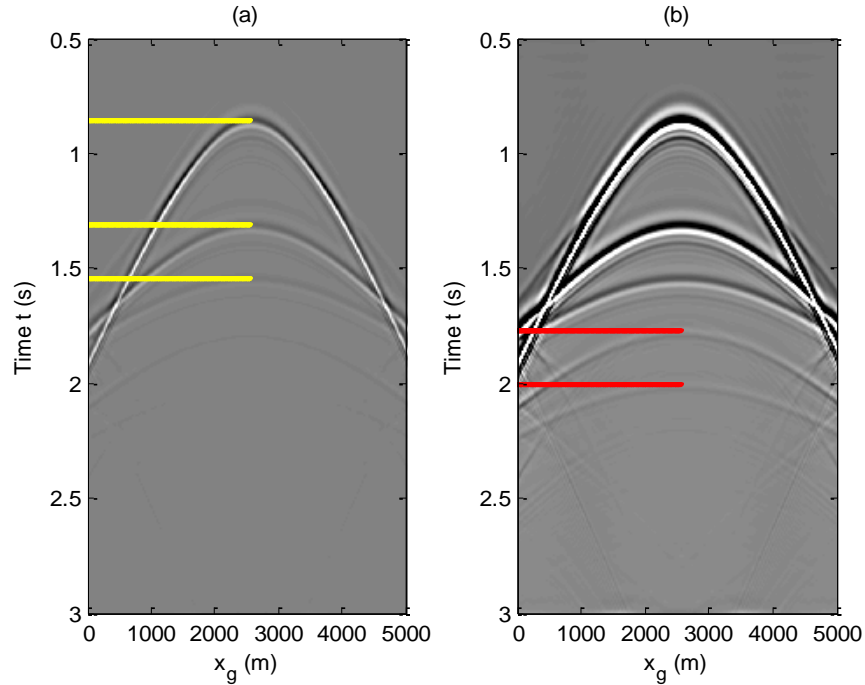


Figure 3.2: Shot record calculated using the velocity model in Figure 3.1. (a) Zero-offset travel times of primaries are indicated by yellow lines; (b) zero-offset travel times of internal multiples are indicated by red lines.

Table 3.1: Parameters of the velocity model and shot record

Parameter	Value
Number of x	512
Number of z	512
Interval sample time	2 ms
Velocity and depth of the first interface	2800 m/s at 640 m
Velocity and depth of the second interface	4500 m/s at 1280 m
Velocity and depth of the third interface	5500 m/s at 1800 m
Wave speed of the source/ receiver medium	1500 m/s
Time step	1 ms
Maximum time of the shot record	3 s
Location of the source	(2, 256)
Frequency band	[5 10 30 40] Hz

Optimum epsilon (ϵ)	200 ms
Receiver spacing	10 m

3.2.2 Making the pseudo-depth domain input $b_1(k_g, z)$

Secondly, the pseudo-depth domain input $b_1(k_g, z)$ was created. The data were Fourier transformed from the time domain (x_g, t) grid to the frequency domain (k_g, ω) grid. Then a change of variables was made from ω to k_z using the following relationship:

$$k_z = \frac{2\omega}{c_0} \sqrt{1 - \frac{k_g^2 c_0^2}{\omega^2}}, \quad (3.1)$$

to generate a regular output grid on (k_g, k_z) . Since the wavenumber k_z is conjugate to the pseudo-depth $z = c_0 t / 2$, an optimum grid was chosen for resampling vectors by starting with the input time vector:

$$t = dt * ((1 : N) - 1); \quad (3.2)$$

where dt was the sampling interval. Then the time vector was mapped to pseudo-depth domain,

$$z = 0.5 * c_0 * t, \quad (3.3)$$

where c_0 was the reference P-wave velocity (1500 m/s is commonly used for marine data). The associated $dz = z(2) - z(1)$ was determined, and then the regularly sampled output depth wavenumber was defined as:

$$k_z = -N / 2 : N / 2 - 1; \quad (3.4)$$

$$k_z = k_z / (N * dz); \quad (3.5)$$

A direct change of variables from the regular grid would lead to a dataset on an irregular (k_g, k_z) grid because the relationship between (k_g, ω) and (k_g, k_z) is nonlinear (Innanen, 2012). To overcome this problem, a regular (k_g, k_z) grid (with k_z chosen as described above) was computed and a linear interpolation of the data onto these irregularly spaced values was performed.

Figure 3.3 shows the input to the prediction algorithm. The input was constructed for positive k_g values only; the negative wavenumbers can be filled later using conjugate symmetry. Three primaries are visible on the graph when $k_g > 0$. Figure 3.4 is the comparison between the zero-offset trace input and constructed $b_1(k_g, z)$ input stacked over k_g . In Figure 3.4 (b), positions of primaries are indicated by the red circles and internal multiples are indicated by the blue circles.

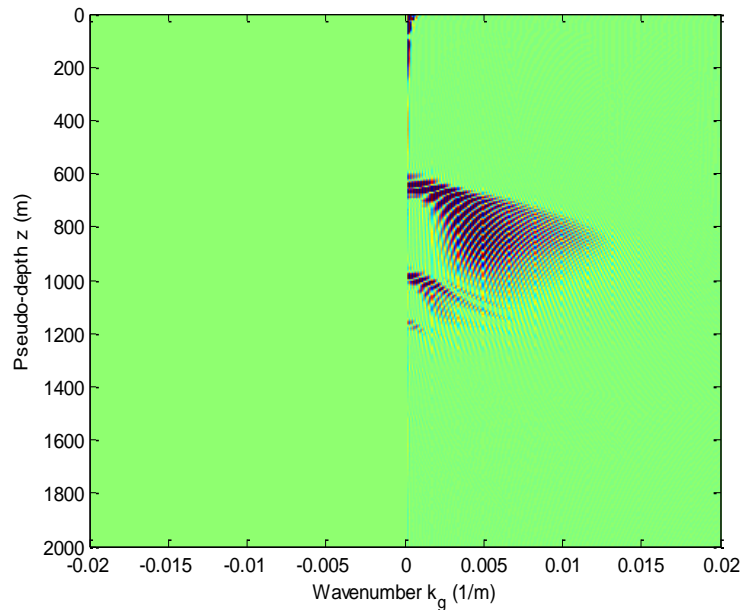


Figure 3.3: The input $b_1(k_g, z)$ is generated using the input data and reference velocity c_0 .

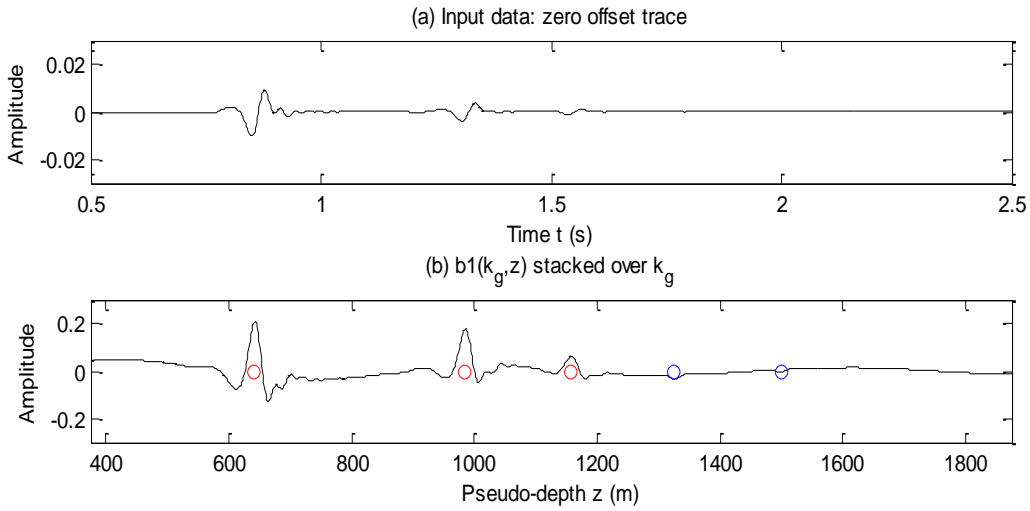


Figure 3.4: Comparison of the input zero-offset trace and constructed input. (a) Input data: zero-offset trace; (b) constructed input stacked over the wavenumbers. The red circles and the blue circles show locations of primaries and internal multiples, respectively.

3.2.3 Internal multiple prediction

Finally, the input $b_1(k_g, z)$ was loaded into the prediction algorithm. This 1.5D prediction algorithm contains three integrations over lateral wavenumber, temporal frequency and nested sums over pseudo-depth. Figure 3.5 is the output of the 1.5D internal multiple prediction. In Figure 3.5 (a), the prediction output matches well with the travel times of internal multiples in Figure 3.5 (b). Internal multiples around 1.8 s and 2.0 s are correctly predicted. The zero-offset travel times and moveout patterns of the internal multiples are correctly displayed in the prediction output, which means the 1.5D internal multiple prediction algorithm works well on layered synthetic data.

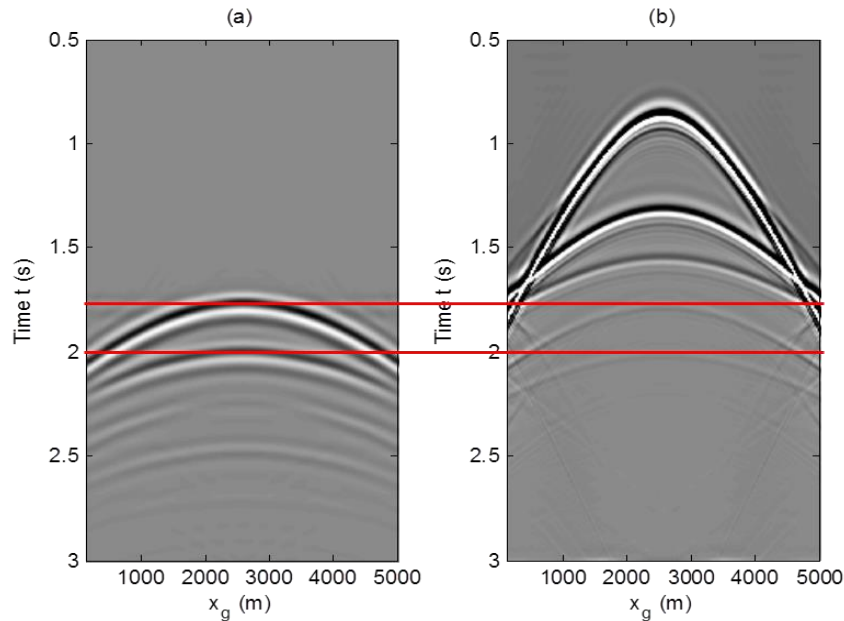


Figure 3.5: The output of the 1.5D internal multiple prediction with an ϵ value of 200 ms. (a) The two predicted internal multiples. (b) The original data with both primaries and internal multiples.

Another scenario with interfering primaries and internal multiples was examined. All the parameters were the same as the case above except for the velocity and depth of each layer (Table 3.2). Figure 3.6 is the prediction output for this case. The internal multiple at 1.8 s, that is mixed with a primary has been correctly predicted. The results from Figure 3.6 suggested that internal multiples which interfere with primaries are correctly predicted using the 1.5D prediction algorithm.

Table 3.2: Parameters of the new velocity model

Parameter	Value
Velocity and depth of the first interface	2800 m/s at 640 m
Velocity and depth of the second interface	4000 m/s at 1280 m
Velocity and depth of the third interface	5000 m/s at 2000 m

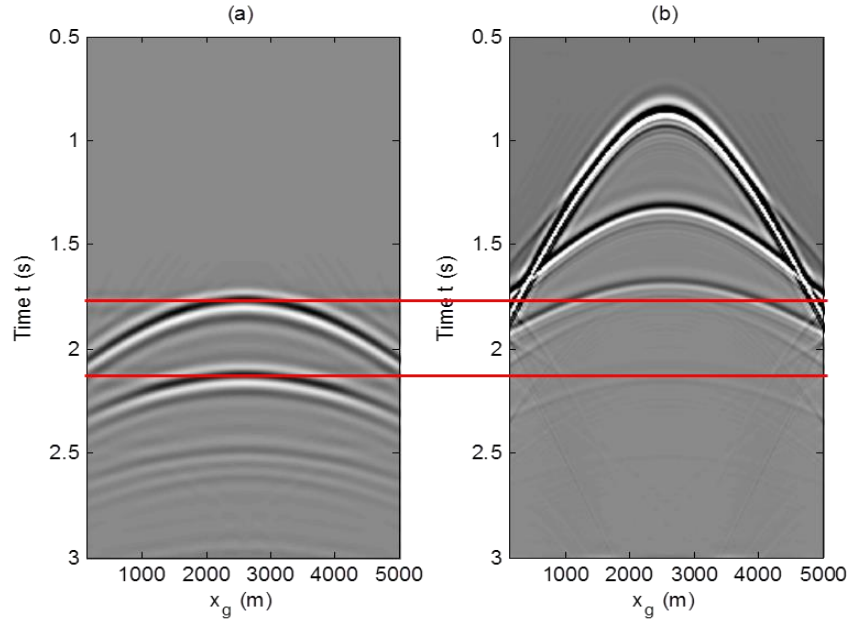


Figure 3.6: The output of the 1.5D internal multiple prediction with an ϵ value of 200 ms. In this case, a primary and an internal multiple interfere. (a) The two predicted internal multiples. (b) The original data with both primaries and internal multiples.

3.3 Analysis on the effects of ϵ values

In this section, the effects of various ϵ values on the accuracy of the 1.5D prediction algorithm were analyzed. Three ϵ values of 100, 200 and 300 time samples were considered and the optimal ϵ value was determined to be 200 ms. The first velocity model (Figure 3.1) and shot record (Figure 3.2) were used to implement the test. Figure 3.7 (a), (b), and (c) show the outputs with ϵ values of 100 ms, 200 ms, and 300 ms, respectively.

Far-offset artifacts arise at the arrival times of primaries when the ϵ value is smaller than the optimal value. Whereas, ϵ values greater than the optimal value damage the prediction output

preferentially at near offsets. There are no equations to calculate ϵ directly. For band-limited data, ϵ values can generally be selected by using the width of the wavelet as a guide. This examination suggests that in 1.5D, an iterative procedure, in which ϵ is gradually increased from an erroneously low value, until far-offset artifacts with the arrival times of primaries are suppressed, could act as an additional guide.

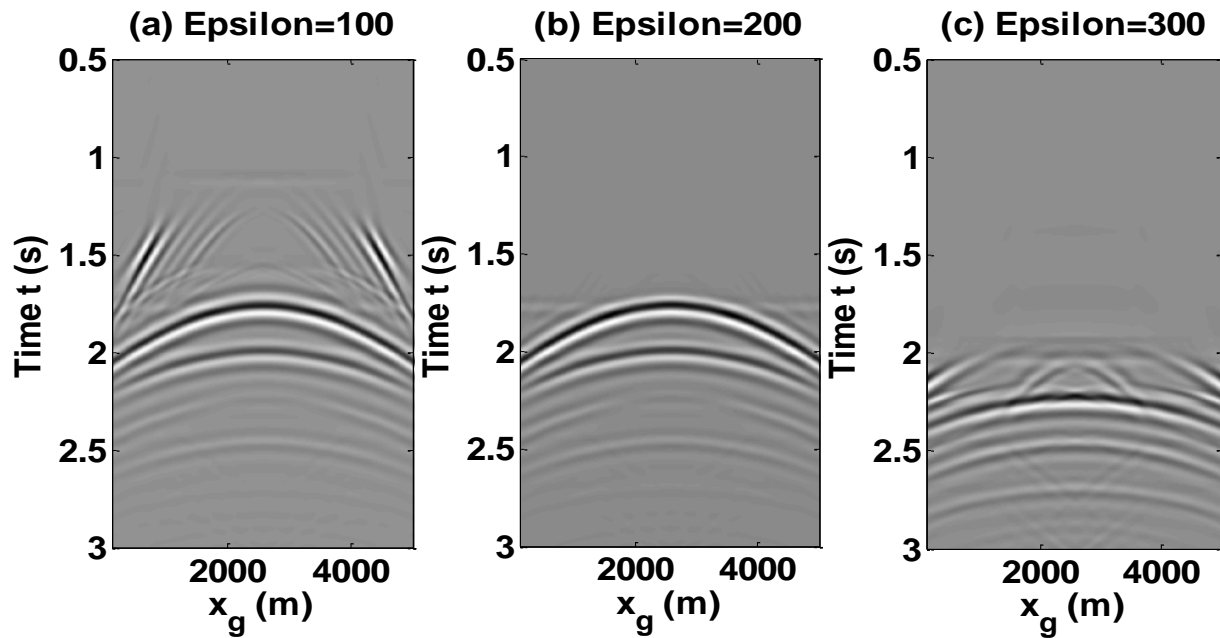


Figure 3.7: Comparison of outputs of the 1.5D internal multiple predictions with ϵ values of 100, 200, and 300 respectively. (a) The output with an ϵ value of 100 ms. (b) The output with an ϵ value of 200 ms. (c) The output with an ϵ value of 300 ms.

3.4 Analysis on the effects of dipping angles

The 1.5D internal multiple algorithm correctly predicts internal multiples provided that the geological volume under study is flat. The effects of dipping angles on the accuracy of the 1.5D algorithm were analyzed using synthetic records generated from models with dip. Figure 3.8 is a velocity model where the generator is the dipping interface with a dipping angle of 2 degrees.

Figure 3.9 is the resulting synthetic data. The arrival times of the internal multiples are affected by the dipping generator. The prediction output of 1.5D algorithm is displayed in Figure 3.10.

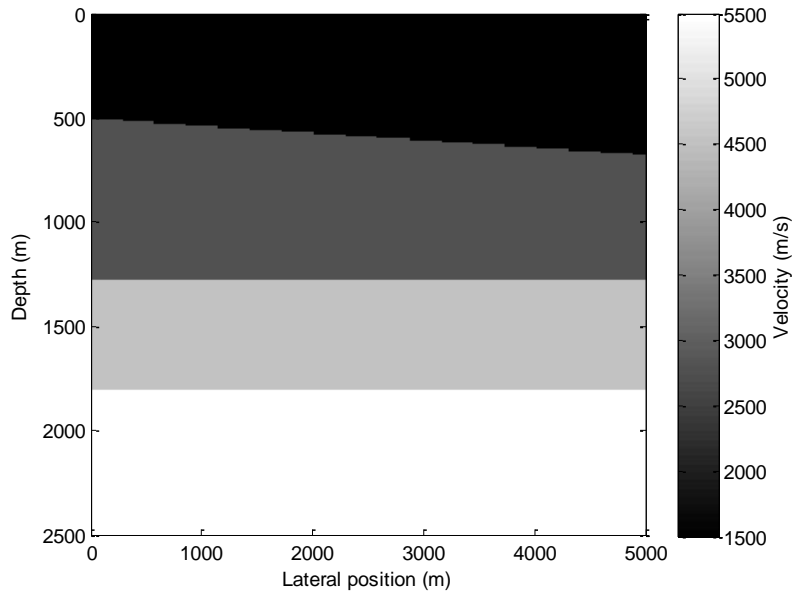


Figure 3.8: Four-layer velocity model with the first interface's dipping at 2 degrees.

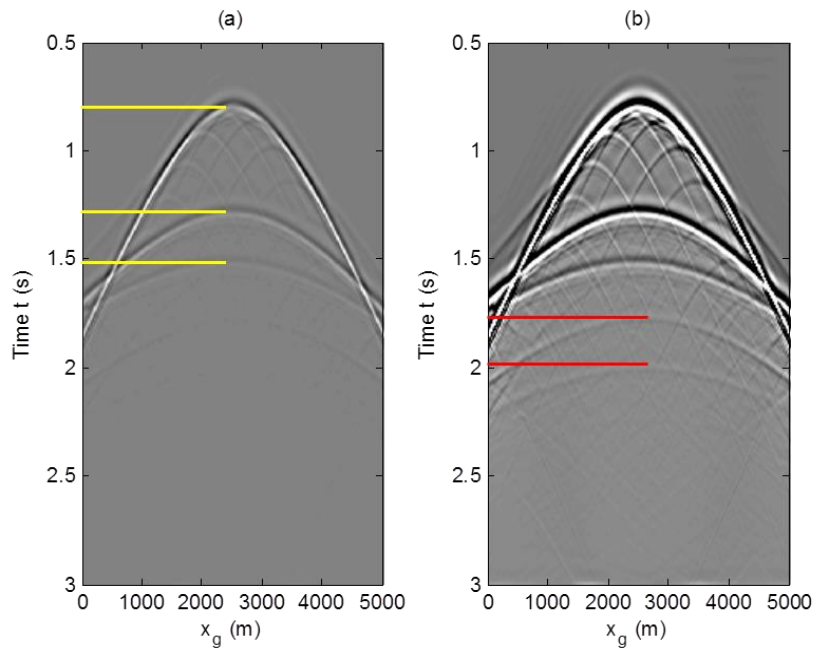


Figure 3.9: Shot record calculated using the velocity model in Figure 3.8. (a) Zero-offset travel times of primaries are indicated by yellow lines; (b) zero-offset travel times of internal multiples are indicated by red lines.

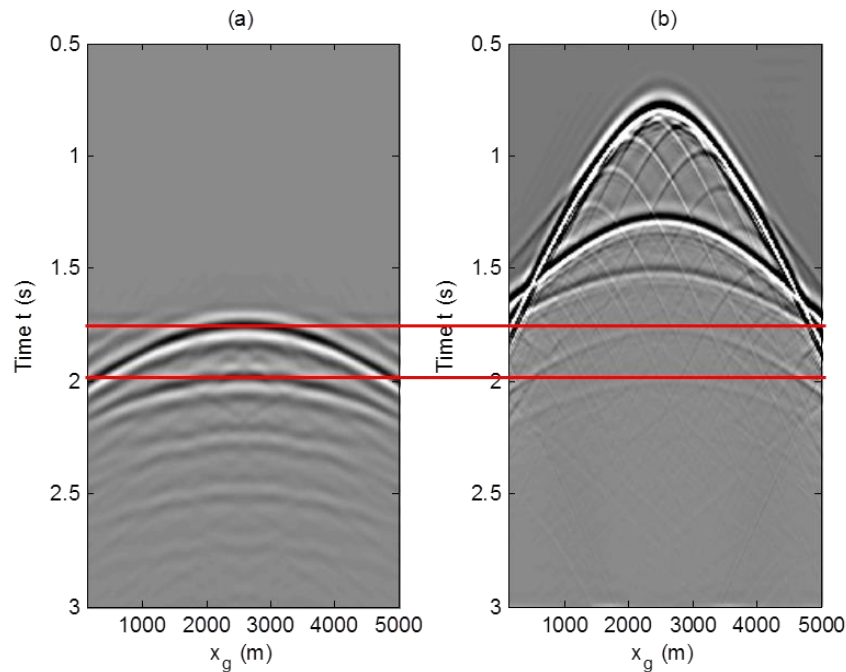


Figure 3.10: The output of the 1.5D internal multiple prediction with an ϵ value of 200 ms. (a) The two predicted internal multiples. (b) The original data with both primaries and internal multiples. Red lines indicate the positions of the internal multiples.

Another test using a dip angle of 5 degrees was performed. Figures 3.11, 3.12 and 3.13 are the velocity model, shot record and prediction output, respectively.

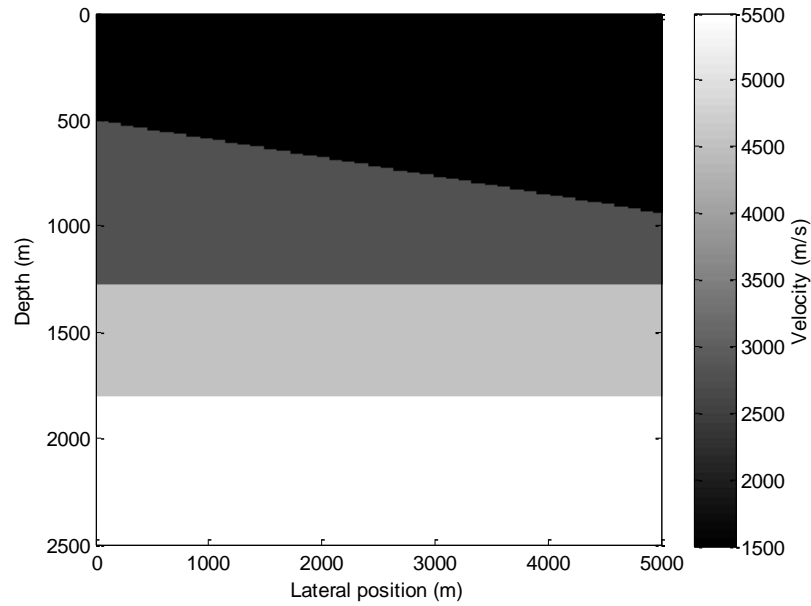


Figure 3.11: Four-layer velocity model with the first interface dipping at an angle of 5 degrees.

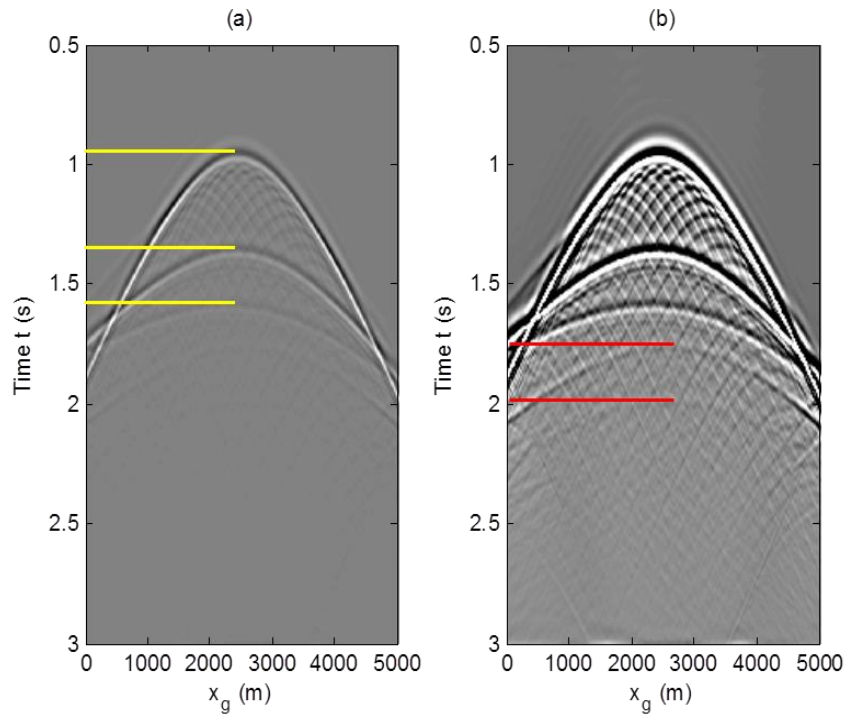


Figure 3.12: Shot record calculated using the velocity model in Figure 3.11. (a) Zero-offset travel times of primaries are indicated by yellow lines; (b) zero-offset travel times of internal multiples are indicated by red lines.

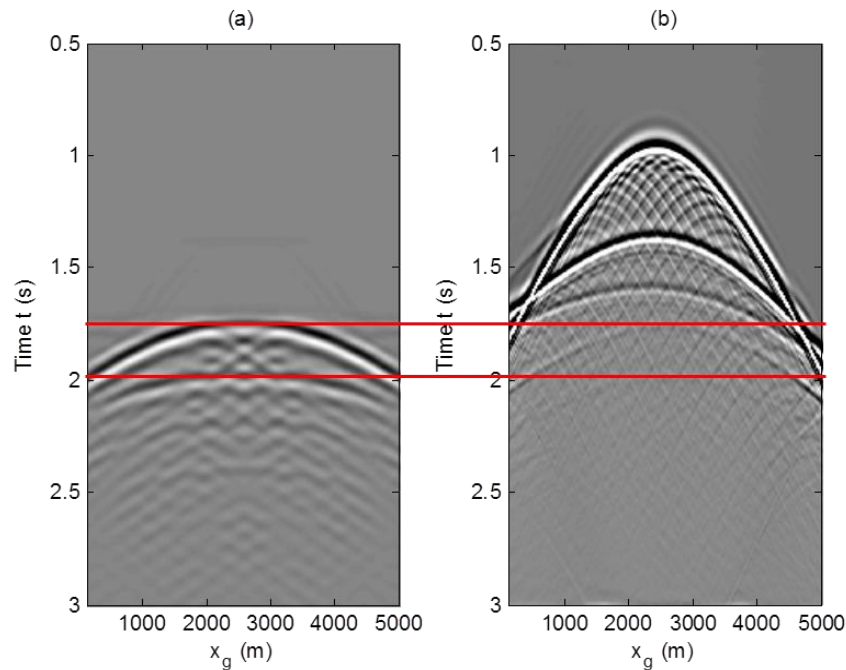


Figure 3.13: The output of the 1.5D internal multiple prediction with an ϵ value of 180 ms. (a) The two predicted internal multiples. (b) The original data with both primaries and internal multiples. Red lines indicate the positions of the internal multiples.

Comparing Figure 3.10 and Figure 3.13, it can be seen that as the generator dip angle increases, near-offset oscillations from missing lateral wavenumber combinations (with some influence of the modelling noise in the synthetic data) become increasingly noticeable in the prediction record.

Next, the prediction errors of IM1 and IM2 from the zero-offset trace (trace 256), near-offset trace (trace 200), and far-offset trace (trace 100) taken from dipping interfaces were analyzed respectively. The dip angles were increased gradually from 0 to 10 degrees. In Figure 3.14 and Figure 3.15, the blue line represents the prediction errors of the zero-offset trace, the red line represents the prediction errors of the near-offset trace, and the green line represents the

prediction errors of the far-offset trace. In both figures, larger error fluctuations are present in the far-offset trace than the other traces. This implies that the dipping interface has greater influence on far-offset traces compared to near-offset traces. As well, errors in both IM1 and IM2 generally increase with dipping angle. Anomalies can be attributed to the interference of artifacts and internal multiples. Since the travel times of internal multiples were manually picked, occasionally artifacts may be mistakenly chosen as internal multiples.

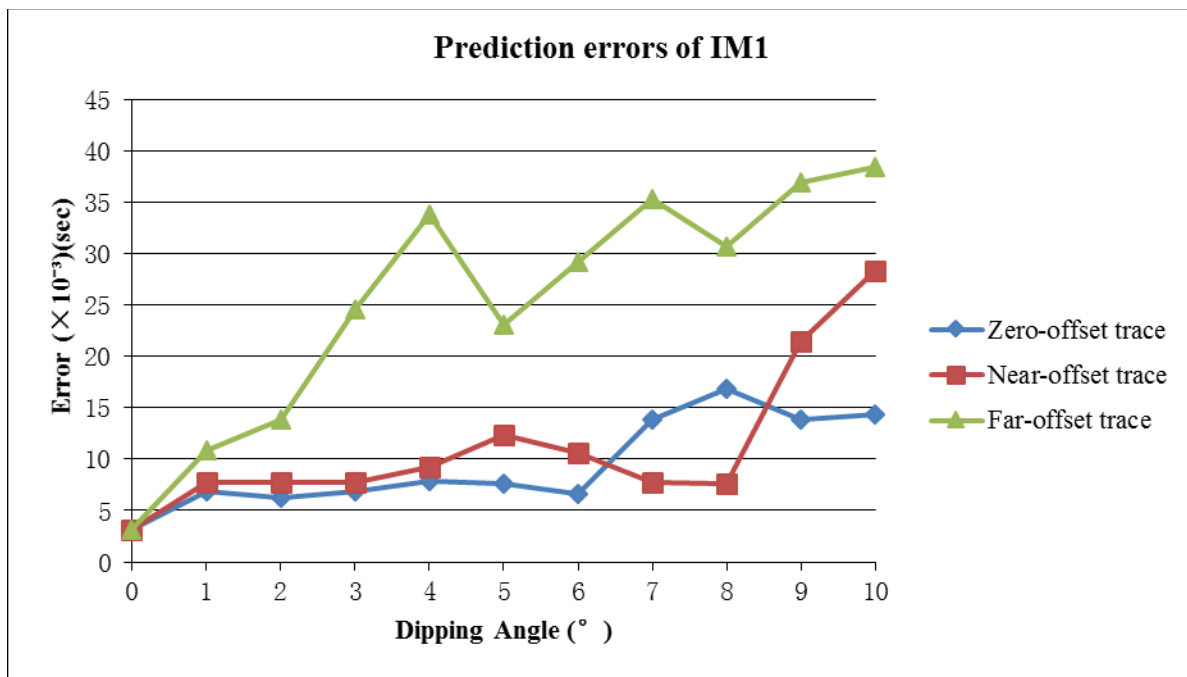


Figure 3.14: Prediction errors of IM1 plotted against an increasing series of dipping angles.

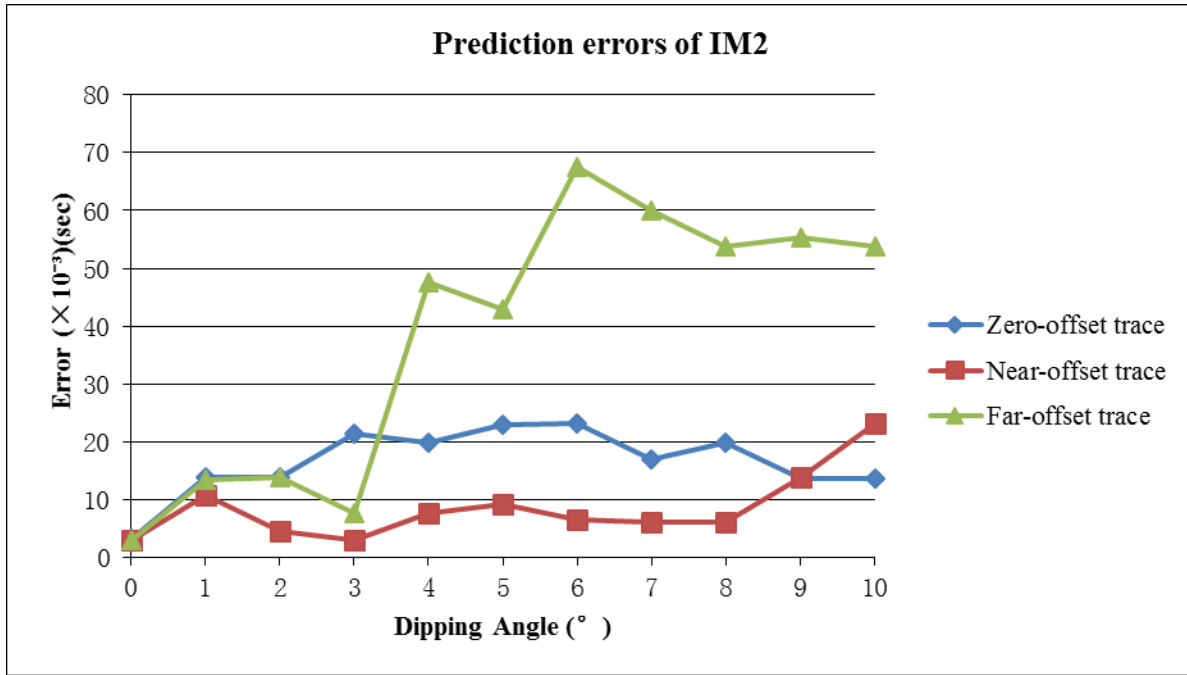


Figure 3.15: Prediction errors of IM2 plotted against an increasing series of dipping angles.

3.5 Analysis on large-dip artifacts

In this section, large-dip artifacts in unfiltered 1.5D internal multiple predictions are analyzed.

Here, large-dip refers to dip of data event. The implementation of a k_g -dependent integration-

limiting parameter ϵ can reduce large-dip artifacts. A new dataset was created to address the

problem because in previous sections a fixed ϵ value was used to perform the prediction. A three-

layer velocity model with large impedance contrasts was created (Figure 3.16) and a

corresponding shot record is shown in Figure 3.17. The first primary event intersects with two internal multiple events, and this may create problems using the fixed ϵ value prediction method.

The parameters for this new model are listed in Table 3.3. The absolute values of $b_1(k_g, z)$ are

plotted in Figure 3.18. On the left edge of the panel, two primaries intersect with the z axis at

their pseudo-depths, and the relationship between pseudo-depth and time is $z = c_0 t / 2$. In this case, an assumed velocity of $c_0 = 1500 \text{ m/s}$ was used. The internal multiple prediction using the optimum fixed ϵ value (200 ms) is illustrated in Figure 3.19. The two internal multiple events have been predicted correctly in the prediction output. However, there are large-dip artifacts intersecting the x axis at roughly 1000 m and 4000 m, which is related to the large-offset arms of the first primary. The artifacts in Figure 3.19 (a) match with primaries, and emerge at large dips suggesting that the ϵ value, which was chosen based on the zero-offset trace (i.e., lateral wavenumber $k_g = 0$) is too small in application to the larger k_g values.

Weglein et al., (2003) pointed out that the role of ϵ is to limit the ability of the algorithm to classify the subevents which satisfy the “lower-higher-lower” relationship. However, a finite-length wavelet has lobes, and the lobes of a single wavelet also obey a lower-higher-lower relationship. If the internal lobes of a wavelet are treated as sub-events, both internal multiples and primaries are predicted which might cause a significant threat to the primary signal energy when performing subtraction procedure (Innanen and Pan, 2014).

As per section 3.3, far offset artifacts occur when ϵ values are less than 200 ms and near offset artifacts occur when ϵ values are greater than 200 ms. The ϵ value of 200 ms is optimum for the zero-offset trace, but this optimum ϵ value does not reduce artifacts for far offset traces.

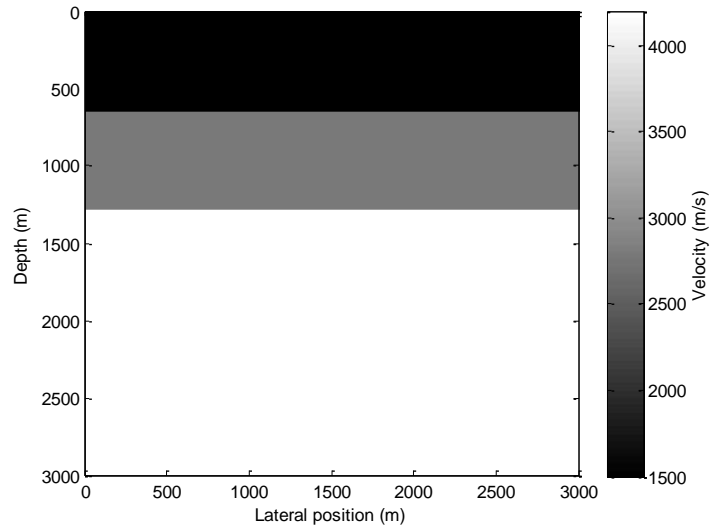


Figure 3.16: Three-layer velocity model used to test the large-dip artifacts. Medium velocities range from 1500 m/s (top) to 2800 m/s (middle) to 4200 m/s (bottom).

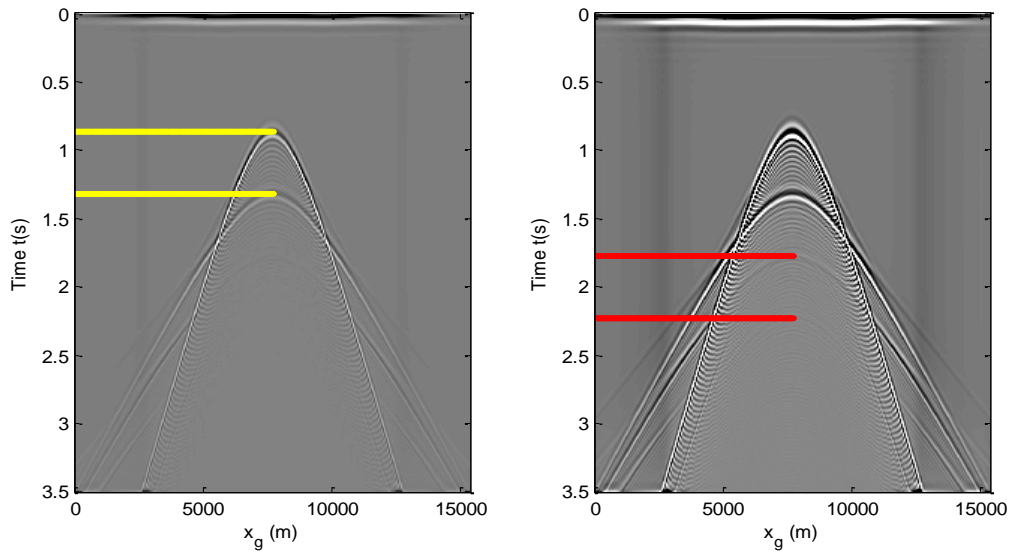


Figure 3.17: Shot record calculated using the synthetic model in Figure 3.16. (a) Zero-offset travel times of primaries are indicated by the yellow lines; (b) zero-offset travel times of internal multiples are indicated by the red lines.

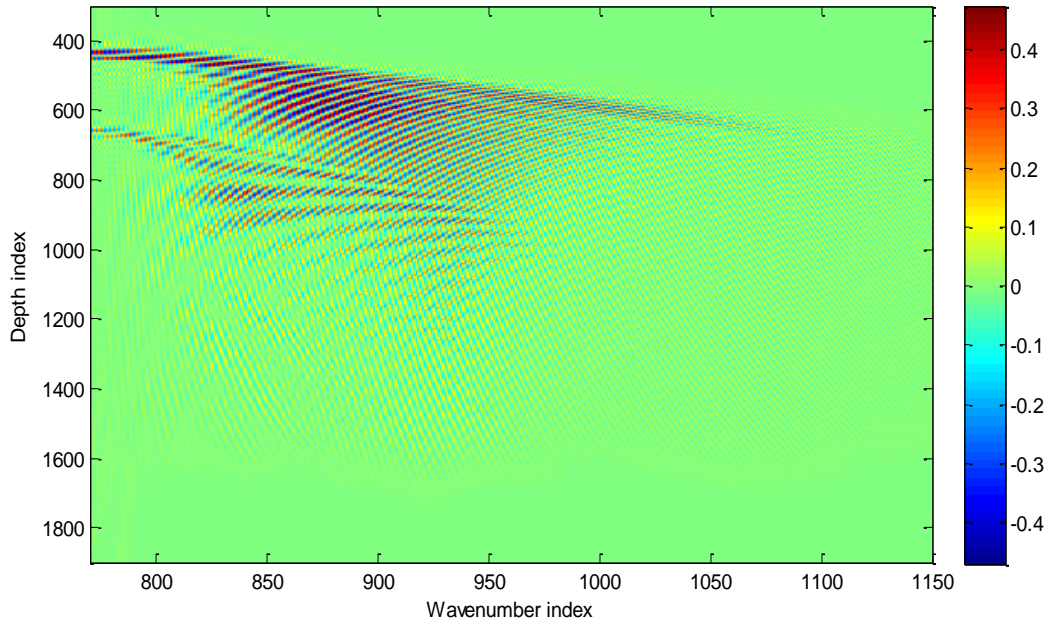


Figure 3.18: The input for the internal multiple prediction algorithm.

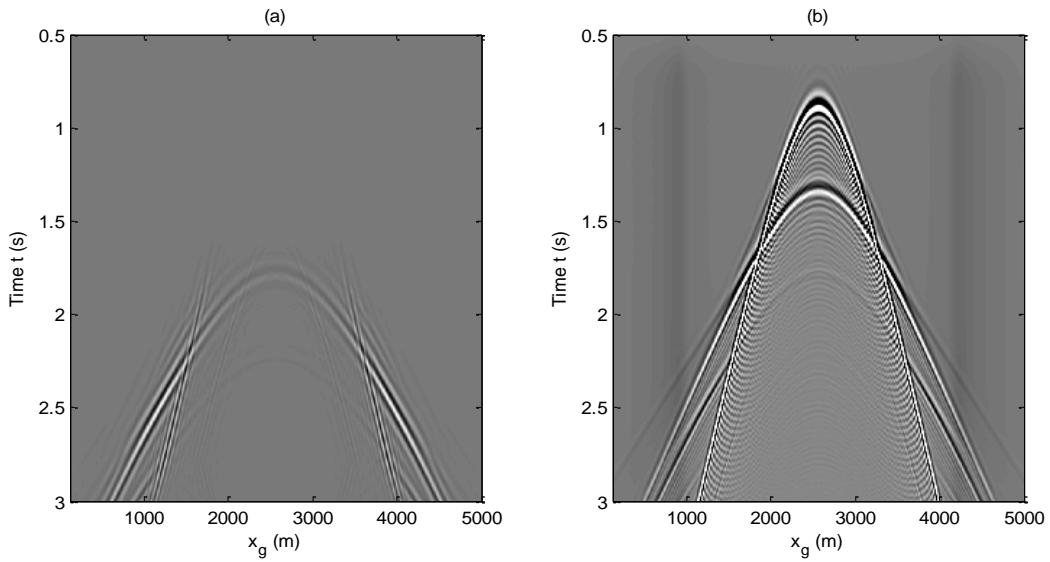


Figure 3.19: The output of the 1.5D internal multiple prediction with a fixed ϵ value of 180 ms. (a) The two predicted internal multiples. (b) The original data with both primaries and internal multiples.

Table 3.3: Parameters of the new velocity model and shot record

Parameter	Value
Number of x	1024
Number of z	1024
Interval sample time	2 ms
Velocity and depth of the first interface	2800 m/s at 640 m
Velocity and depth of the second interface	4200 m/s at 1280 m
Wave speed of the source/ receiver medium	1500 m/s
Time step	1 ms
Maximum time of the shot record	3.5 s
Location of the source	(2, 512)
Frequency band	[5 10 30 40] Hz
Optimum ϵ (fixed)	180 ms
Receiver spacing	15 m

To solve this problem, different ϵ values were assigned to different k_g values so that each k_g value has an associated ϵ value (Figure 3.20). The input $b_1(k_g, z)$ for the prediction algorithm is depicted in Figure 3.20 (a). The left edge of the graph is $k_g = 0$. The variation of $|b_1(k_g, z)|$ is not as simple as in the case of 1D algorithm, but it has some general properties. The event in Figure 3.20 (c) spreads out in depth with increasing k_g suggesting that ϵ is a growing function of k_g .

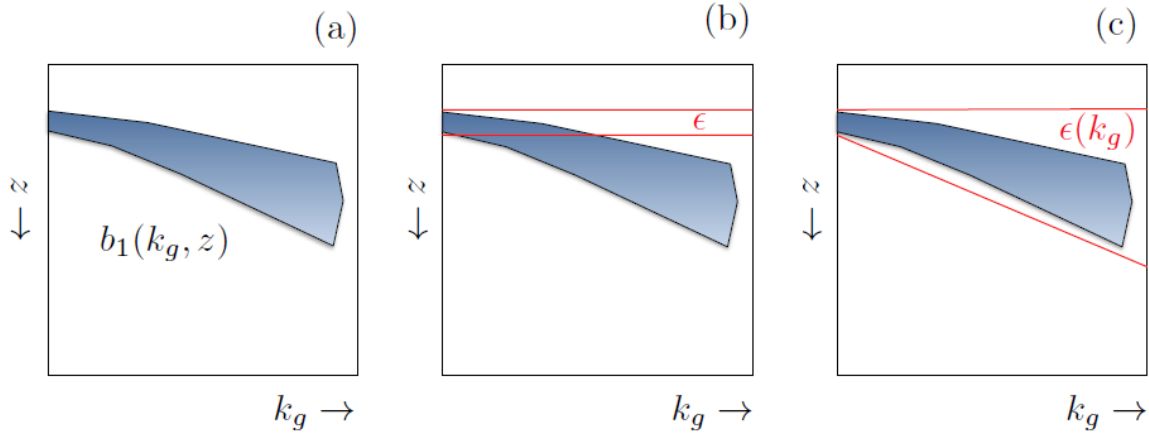


Figure 3.20: The scheme to mitigate large-dip artifacts. (a) Illustration of the input consisting of one event to the prediction algorithm; (b) a fixed ϵ value chosen based on pseudo-depth at $k_g = 0$; (c) coping method used to account for the tendency of $b_1(k_g, z)$ to spread out in z as k_g increases (from Innanen and Pan, 2014).

Figure 3.21 illustrates the method used to derive a function, $\epsilon(k_g)$, relating ϵ to k_g . First, the minimum value of ϵ (ϵ_{\min}), the maximum value of ϵ (ϵ_{\max}) and the end value of k_g ($k_g \text{ End}$) were chosen from Figure 3.18. The minimum value of ϵ has been chosen to be 150 ms for $k_g = 0$. The end of k_g value was determined to be 1150 so that the maximum value of ϵ was set to be 1100 ms. Based on Figure 3.21, a relationship for a linear ϵ was derived:

$$\epsilon(k_g) = \epsilon_{\min} + \left(\frac{\epsilon_{\max} - \epsilon_{\min}}{k_g \text{ End}} \right) k_g \quad (3.6)$$

In Figure 3.22, the result of this prediction is shown. Compared to Figure 3.19, large-dip artifacts are not present, and there are no artifacts near the bottom axis. In this way, the artifacts can be tied to the actual origins, and in a manner which directly addresses the problem at its root.

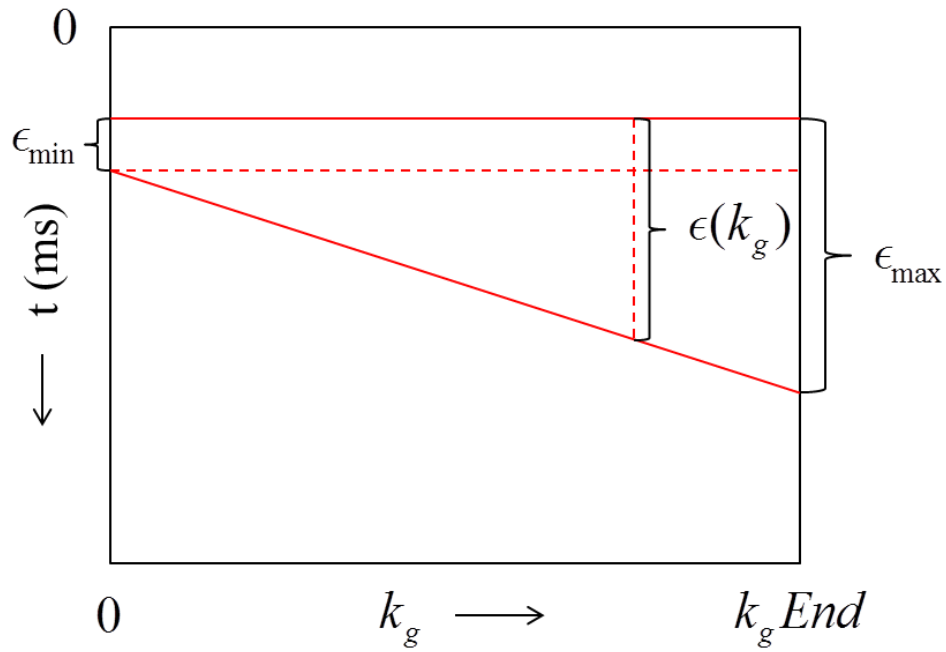


Figure 3.21: The scheme to derive the function of $\epsilon(k_g)$.

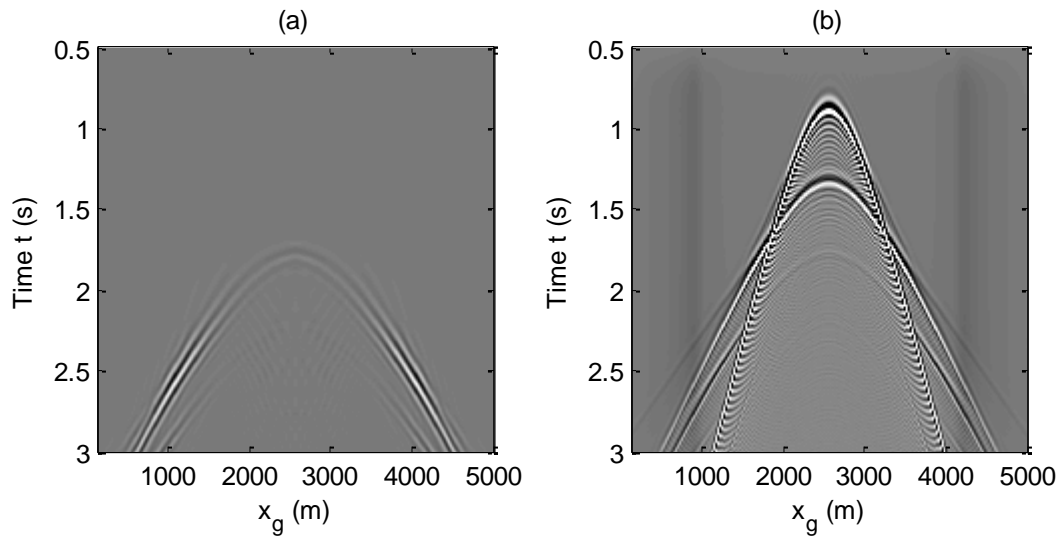


Figure 3.22: Internal multiple predictions using a linear $\epsilon(k_g)$ method. (a) Prediction result; (b) the original data.

3.6 Chapter summary

Chapter 3 examined the 1.5D version of the inverse scattering series internal multiple prediction algorithm. This method does not need any subsurface information and is suitable for the situations where primaries and internal multiples are mixed together. The effects of various ϵ values were analyzed. For a smaller ϵ value, artifacts are seen at the arrival times of primaries. For a larger ϵ value, important information in the prediction output is damaged. The ϵ value can be chosen more effectively by studying the changes of large offset artifacts as ϵ is gradually increased. The rate of error increase in the 1.5D internal multiple prediction algorithm was also examined using data for gradually increasing interface dip. For smaller dipping angles, the results of the algorithm are promising. The algorithm correctly predicts both the zero-offset travel times and moveout patterns. For larger dipping angles, errors become significant. However, the 1.5D algorithm is fast and is valuable for assisting in the verification of the positions of internal multiples. A method to mitigate large-dip artifacts that are noticeable in unfiltered 1.5D internal multiple predictions was developed. This is done by implementing a k_g - dependent integration-limiting parameter ϵ .

Chapter Four: Multiple prediction on physical modelling data

4.1 Chapter overview

Multiple attenuation is a key aspect of seismic data processing, with the completeness of multiple removal often significantly affecting the final results. In this chapter, 1.5D internal multiple prediction on physical modelling data simulating a marine seismic survey designed to generate significant internal multiples are analyzed. First, a processing flow of how to prepare the data for input into the multiple prediction algorithm is described. Then a 1.5D (i.e., pre-stack data over a layered geology) implementation of the inverse scattering series internal multiple prediction is examined. The results show good agreement of multiple predictions between the synthetic data and physical modelling data. The selection of the integration-limiting parameter ϵ and the influence of FSMs are discussed. Also the results suggest that the beginning and ending integration points of frequencies, wavenumbers, and pseudo-depths in the code can be optimally chosen to reduce computational burden.

The scientific purpose of this chapter is to examine the response of the 1.5D internal multiple prediction algorithm as implemented in MATLAB on physical modelling data, and seek out an approach which can reduce computational burden and support interpretation. The laboratory experiment is designed to produce data with significant internal multiple contamination.

4.2 Physical modelling experiment overview

4.2.1 Introduction to physical modelling systems

Seismic physical modelling provides scaled simulations of real world scenarios, the benefits of which are controlled acquisition geometry and physical model properties (Lawton et al., 1998).

Seismic physical modelling surveys have been conducted at the University of Calgary Seismic Physical Modelling Facility since 1985. Data are written into SEG-Y files, and gathers of seismograms can be read directly by processing software such as ProMAX (Wong et al., 2009a). Data are collected with a source transducer and a receiver transducer, each of which is moved independently by four linear motors mounted on a gantry with digital position encoders and motor drives. Two of these motors are responsible for moving the gantry in the X direction, and the remaining two motors move the source or receiver transducer in the Y and Z direction. The eight motors on the two gantries are controlled through a desktop PC running the Windows XP system (Wong et al., 2009b). Additional details regarding the modelling systems are described by Lawton et al. (1989), and Wong et al. (2009a, 2009b).

4.2.2 The physical model set-up

The first step to build a physical model is the selection of materials. The materials used in this case were water, polyvinyl chloride (PVC), Plexiglas and aluminum; these choices introduce several large impedance contrasts which subsequently produce significant internal multiples. The schematic diagram of the physical modelling experiment is illustrated in Figure 4.1, along with its scaled length and elastic parameters. A similar model was investigated by Hernandez in the context of purely 1D internal multiple prediction (Hernandez, 2012; Hernandez and Innanen, 2014). The model consisted of five layers: water (scaled thickness: 858 m), PVC (scaled thickness: 247 m), water (scaled thickness: 368 m), aluminum (scaled thickness: 132 m), and Plexiglas (scaled thickness: 254 m). The physical models were immersed in a tank of water to simulate a marine environment.

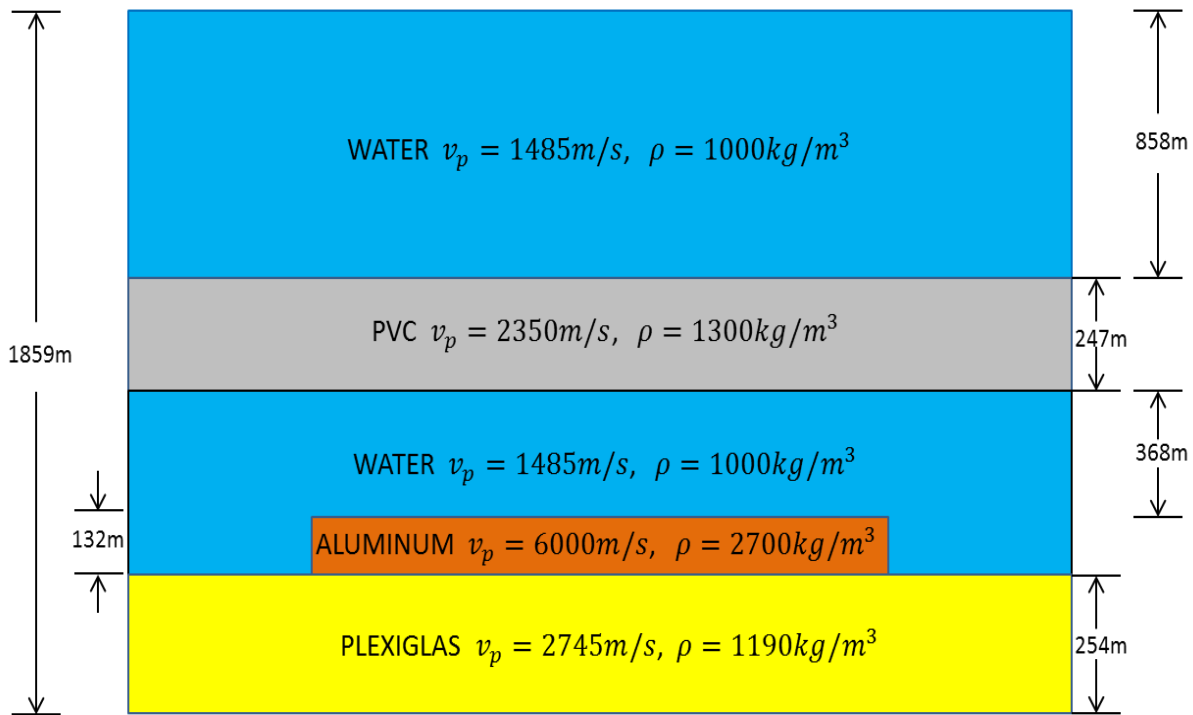


Figure 4.1: Schematic diagram of the physical modelling experiment. All lengths are in scaled units (i.e., physical modelling units multiplied by 10000). The transducers are set just below the water surface.

4.2.3 Physical modelling data acquisition

A common-source seismic survey was conducted over the model (Figure 4.1), with the source and receiver at a fixed depth of 2 mm below the water surface to suppress the source-ghost and receiver-ghost. The source and receiver were 1.36 mm-diameter piezoelectric CA-1136 pin transducers. The source transducer generated ultrasonic seismic pulses and the receiver transducer acted as vertical component geophone. Figure 4.2 shows the 3D positioning system with the source and receiver transducers attached. The source and receiver transducers' initial locations were manually positioned according to a pre-defined coordinate axis on the PVC slab. The source and receiver transducers move in the Y direction along lines that are separated by 10 mm in the X direction (Figure 4.3). The standard model scale factor was $1:10^4$, such that 10 mm

in the model represented 100 m in the real world, and 1 μ s represented 10 ms. All measurement numbers in this chapter will hereafter be scaled to represent field values (which will be referred to as “field scale”) and have approximate errors of 5%. First the source arm was set and then the receiver was moved in the Y direction from left to right in increments of 25 m, covering a total distance of 3 km. A sample rate of 2 ms was used during the acquisition. The scaled frequencies of the vibration pulse varied from 20 to 100 Hz.

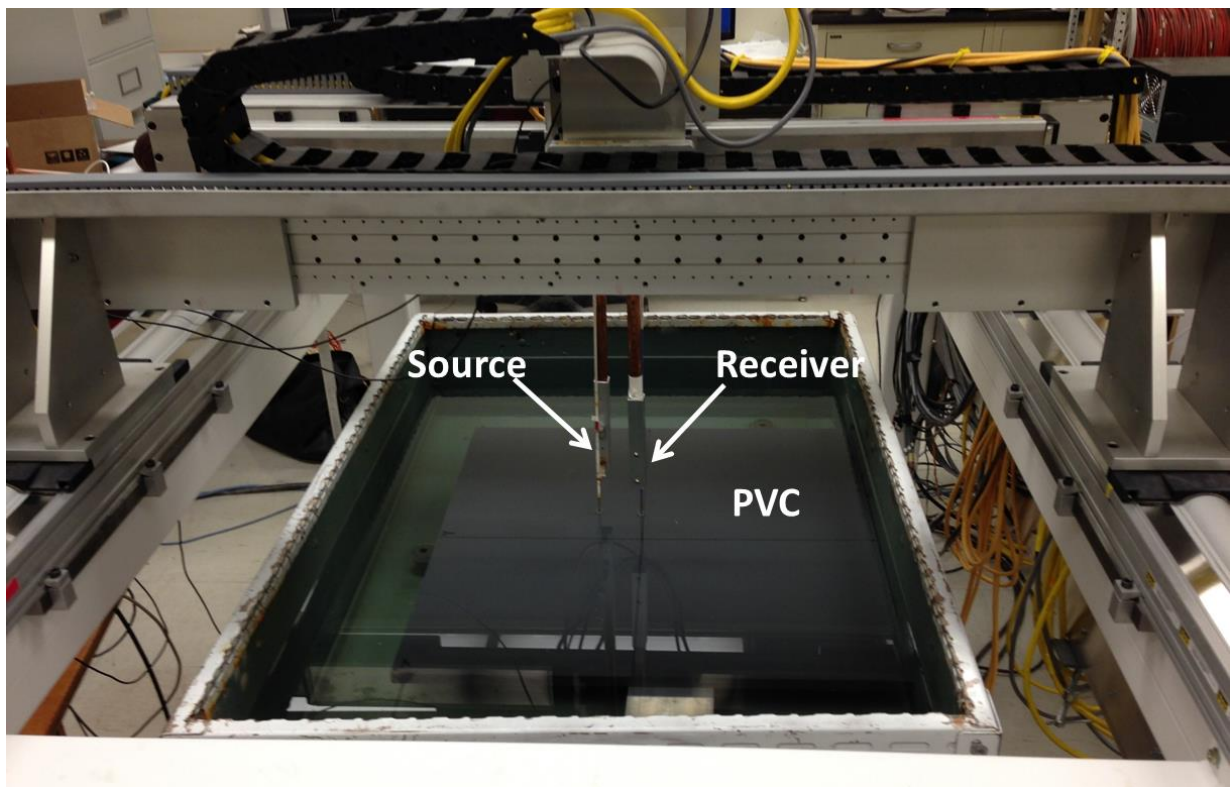


Figure 4.2: The 3D positioning system with source and receiver mounted on the gantries. Physical models are placed in a tank of water beneath the gantries.

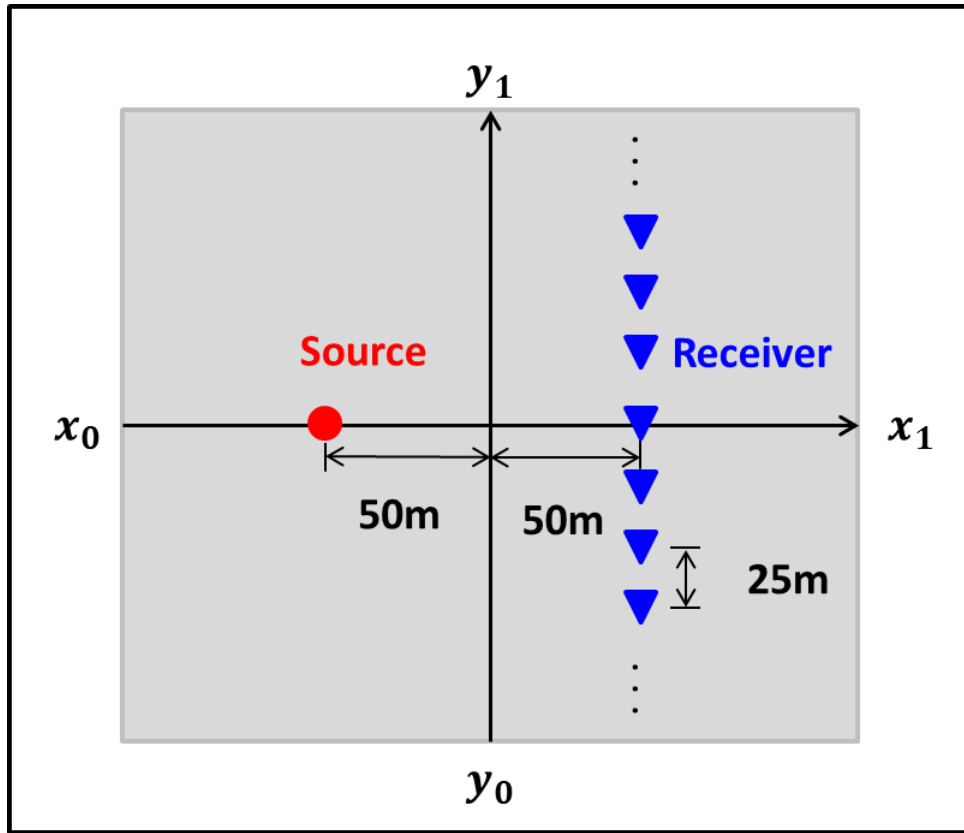


Figure 4.3: Plan view of the physical modelling data acquisition. All units are in field scale.

4.3 Seismic data processing

The physical modelling data were initially viewed in Seisee for quality control and then processed using the ProMAX seismic data processing software. The raw data are shown in Figure 4.4 and a work flow is shown in Table 4.1.

Table 4.1: A processing flow applied to the physical modelling data.

	Processing flow
1	Trace Header Math
2	Top Mute
3	Spiking Deconvolution
4	Bandpass Filter

The survey geometry was loaded from trace headers. From these basic headers, trace header math was used to re-create the source and receiver coordinates to ensure that the data were in sequential order (Wong et al., 2009a). Trace mute was then applied to mute the energy of the direct wave. Another option was to subtract the direct wave which was the linear moveout correction, but usually some residual remains as a consequence. If the direct wave intersects with the primaries, subtracting the direct wave will damage the information contained in the primaries. The raw data after trace mute are shown in Figure 4.5. Source wavelet reverberations (noticeable, for instance, between the first and second primaries at 1200 ms to 1600 ms) were strong, and next process was to suppress them. Spiking deconvolution appears to be an effective tool for this suppression, shortening the period of the embedded source wavelet to create a spike (Geldart and Sheriff, 2004). In this case, the operator length was 80 ms and the operator prediction distance was 35 ms. Predictive deconvolution was also investigated, however it seemed to suppress signal information at later times (about 2300 ms to 2600 ms). Predictive deconvolution should be avoided to retain the energy of multiples. After performing filter panel tests, a bandpass filter of 15-20-70-90 Hz was applied. The deconvolved data are shown in Figure 4.6.

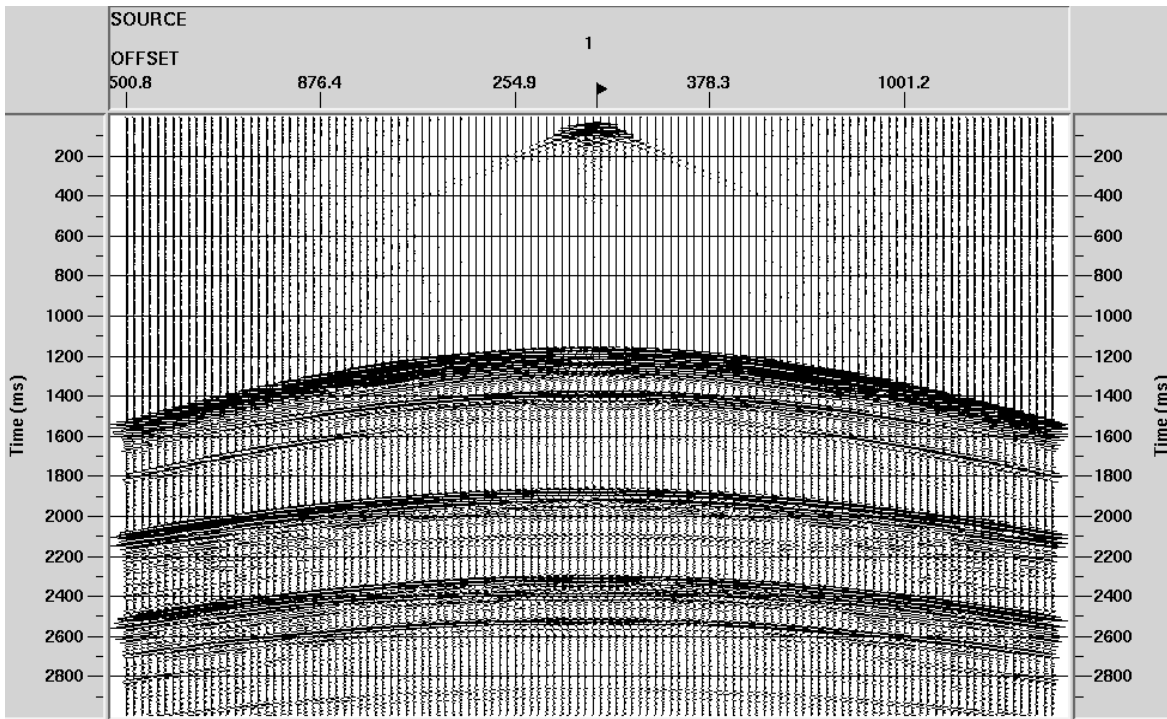


Figure 4.4: Raw data.

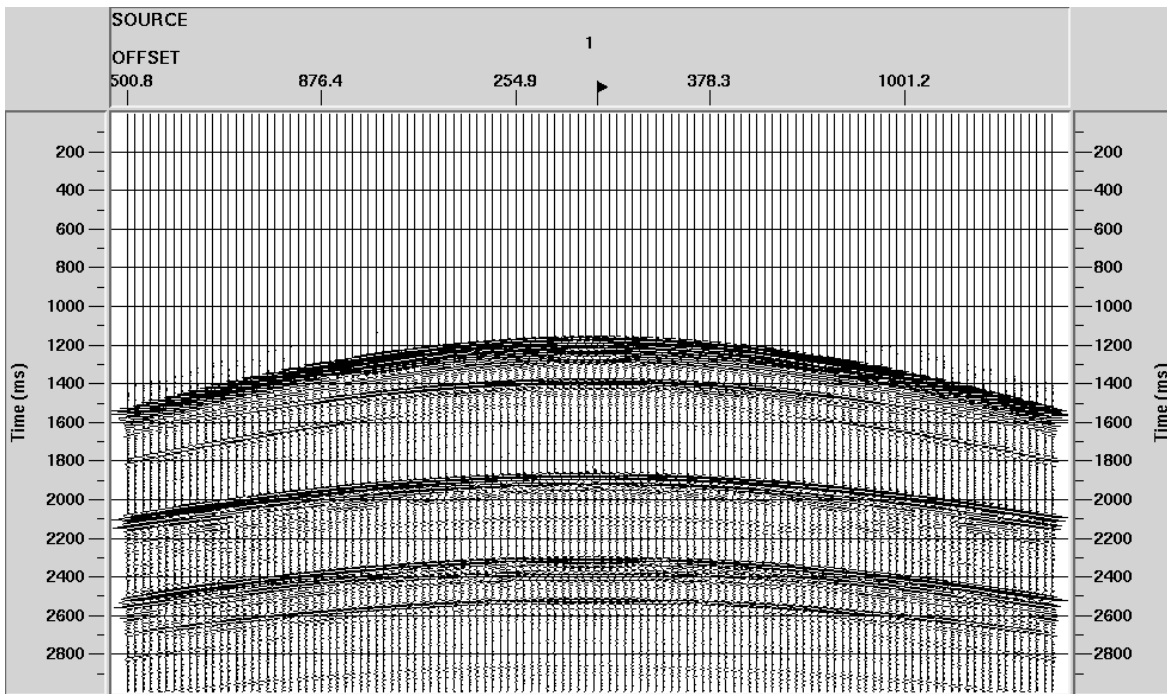


Figure 4.5: Raw data after applying trace mute.

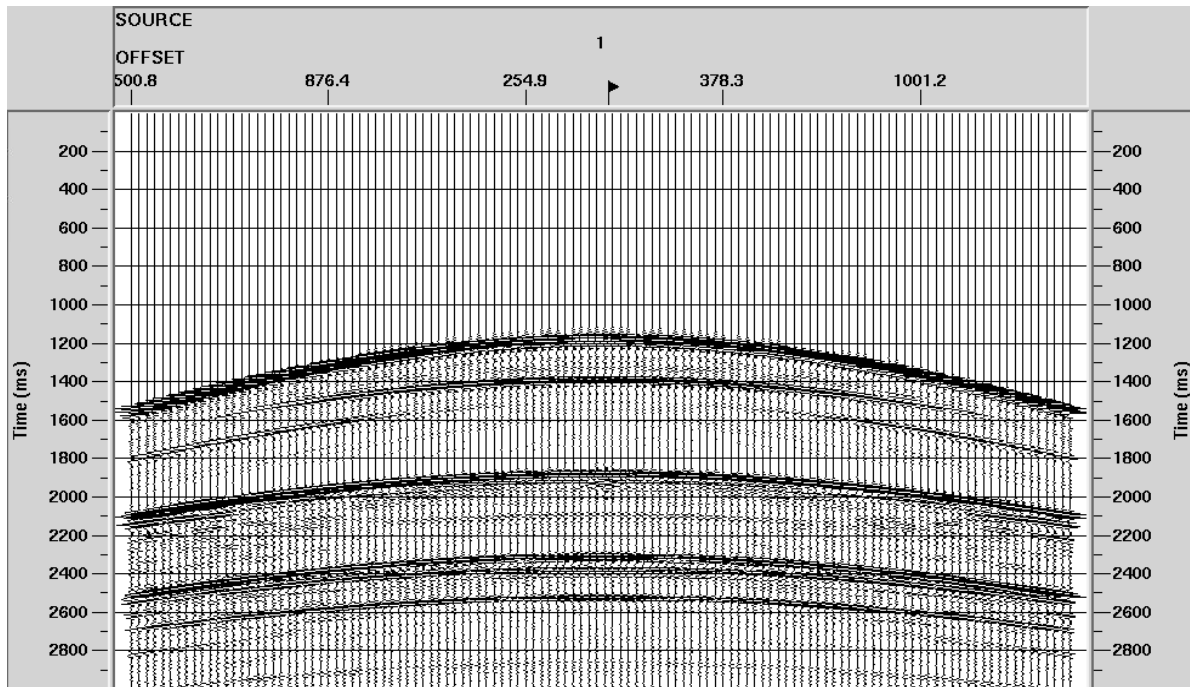


Figure 4.6: The deconvolved data with decon operator length of 80 ms and operator prediction distance of 35 ms. A bandpass filter of 15-20-70-90 Hz was also applied.

4.4 1.5D Internal multiple prediction

4.4.1 Event identification

After pre-processing, our input was then analyzed to provide a framework for interpretation of the output of the internal multiple prediction procedure. Reflection events were identified first. A numerical finite-difference acoustic model was also created using the same parameters as the physical model. The boundary conditions were set to be absorbing for all sides to ensure no FSMs in the synthetic data. The two-way travel times for primaries and multiples (1st order internal multiples and 1st order FSMs) were then calculated. The expected times were approximate because of the measurement error associated with the thickness of each block and the water depth. In Figure 4.7, the interpretations are illustrated. Events A, B, D, E are primaries

and C, F, H, J are first-order internal multiples. The two events G and I are first-order FSMs. The approximate travel time of each event is listed in Table 4.2.

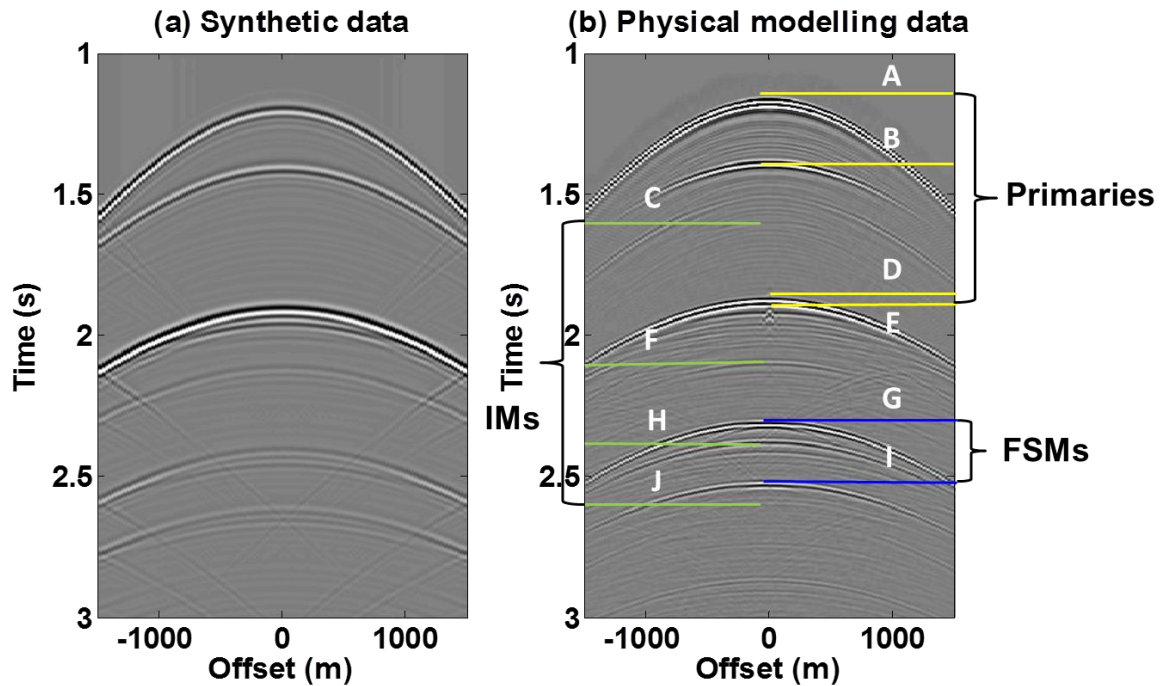


Figure 4.7: Event identification by calculating two-way travel times. Reflection events are labeled on the physical modelling dataset. (a) Synthetic data generated from the same parameters as physical modelling data; (b) physical modelling data.

The zero-offset trace from the synthetic data was also compared with the zero-offset trace from physical modelling data. Figure 4.8 (a) is the zero-offset trace from the physical modelling data, and Figure 4.8 (b) is the synthetic data zero-offset trace. The two traces are not identical; there are some travel time and amplitude differences between the two traces. The travel time differences are within the expected variability caused by non-welded contact between the various slabs (Mahmoudian, 2013), evaporation over time in the tank, and measurements of each slab's thickness. Amplitude differences can be caused by numerous factors such as geometrical spreading, transmission loss, interference of primaries, FSMs and ghost reflections, internal

multiples, and source/receiver array response (Spratt et al., 1993). In this case, the idealized nature of the numerical model (i.e., the assumption of an acoustic/fluid medium) and interference between FSMs and internal multiples are likely the main causes of amplitude discrepancies. The differences between the traces are within the expected variability, therefore it can be concluded that the synthetic and physical modelling data match.

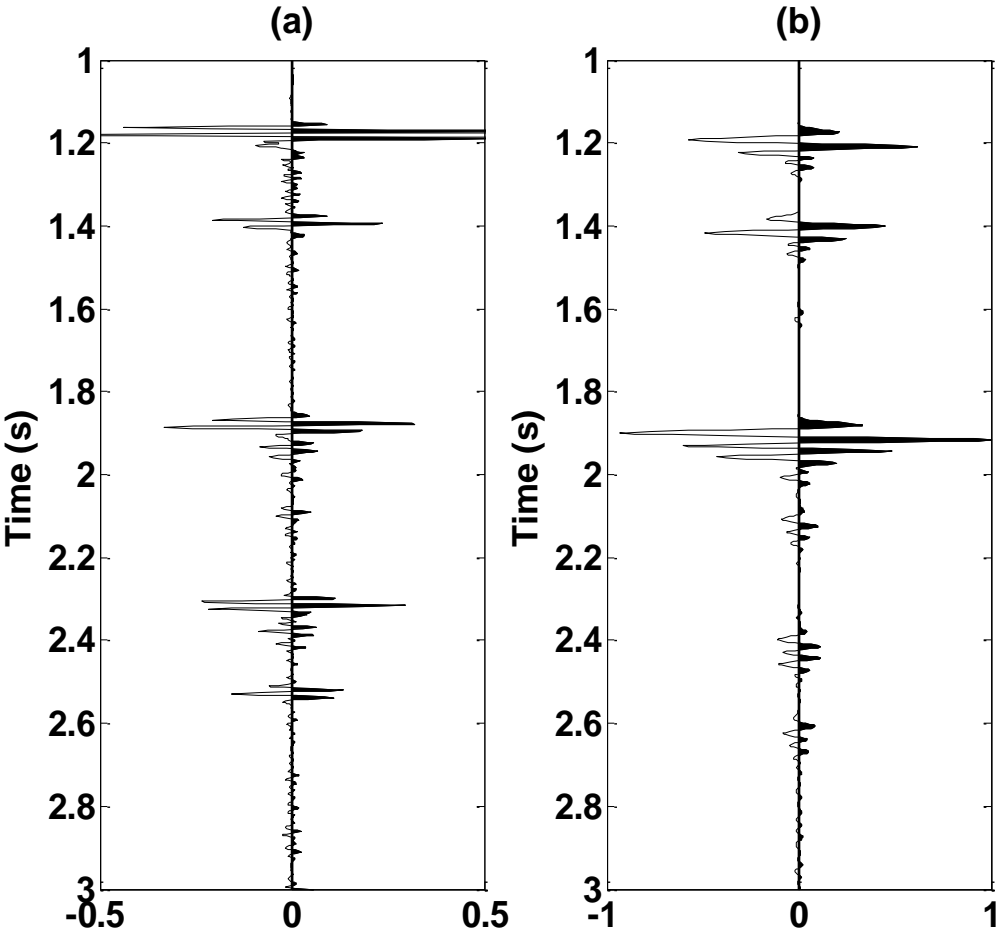


Figure 4.8: The zero-offset trace from physical modelling data (a) and the zero-offset trace from synthetic data (b).

Table 4.2: Summary of approximate travel times of the identified events

Label	Event	Approximate travel time
A	Top of PVC slab	1.155 s
B	Bottom of PVC slab	1.365 s
C	Internal multiple 1	1.575 s
D	Top of aluminum slab	1.861 s
E	Bottom of aluminum slab	1.905 s
F	Internal multiple 2	2.071 s
G	Free-surface multiple 1	2.310 s
H	Internal multiple 3	2.357 s
I	Free-surface multiple 2	2.520 s
J	Internal multiple 4	2.567 s

The ray paths for the internal multiples labelled IM1, IM2, IM3, and IM4 are illustrated in Figure 4.9. There are two superimposed events labelled peg-leg multiple IM2 that have different paths but the same arrival times.

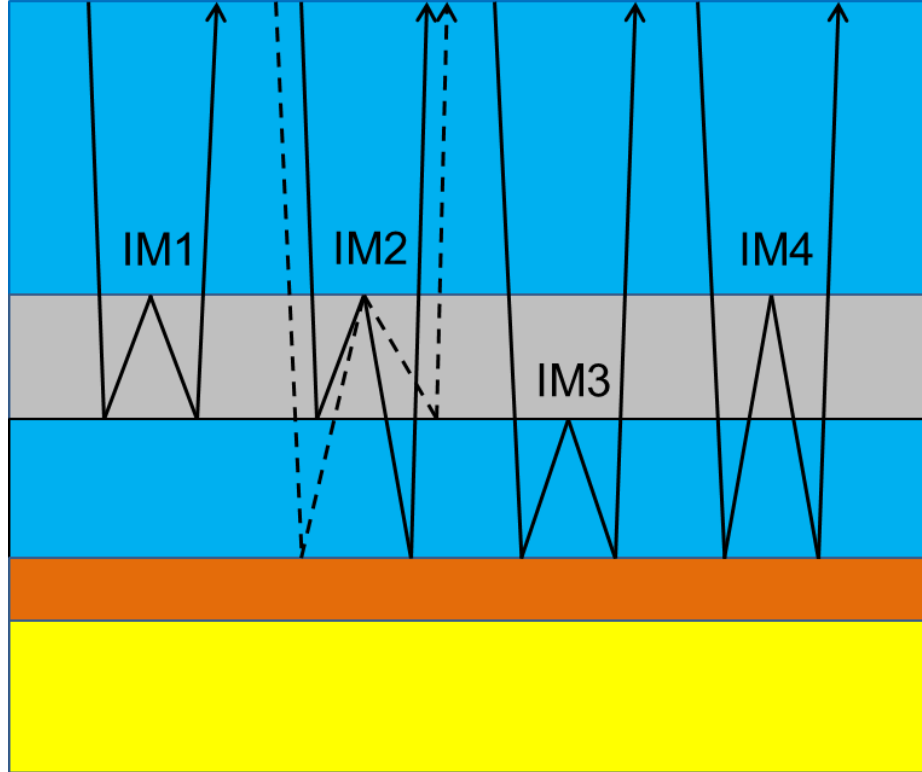


Figure 4.9: The ray paths of the four dominant internal multiples expected from the physical model. IM2 consists of two peg-leg paths, whose travel times are identical.

4.4.2 Internal multiple prediction

The prediction process was applied to the physical modelling data. The SEG-Y file of physical modelling data was loaded into the prediction algorithm. The data were transformed from the space/time domain to the wavenumber/pseudo-depth domain to create the input $b_1(k_g, z)$. The quantity $z = c_0 t / 2$ was the pseudo-depth defined in terms of reference P-wave velocity c_0 and vertical travel time t . After the construction of the input, the 1.5D algorithm, which can be thought of as a sequence of 1D internal multiple predictions, one per output k_g value, was run. An ϵ value, whose practical importance was first pointed out by Coates and Weglein (1996) was chosen based on the width of the wavelet. Effects of various ϵ values have been described in Pan

and Innanen (2014); a smaller ϵ value will result in far-offset artifacts at the arrival time of primaries, whereas, a larger ϵ value will damage the prediction output at near offsets. Here the optimal ϵ value was determined through trial and error to be 80 ms.

An important issue was raised by the notable absence of the prediction of internal multiples generated within the aluminum slab. The aluminum slab has a velocity of 6000 m/s and a thickness of 132 m which means the two reflections generated by the aluminum slab should be very close to each other. The internal multiple prediction relies on events being separated in time by at least the ϵ value, which is 80 ms in this case. The two-way travel time for the top of the aluminum slab is approximately 1.861 s and 1.905 s for the bottom, which means they are separated by 44 ms. Since this is within the time interval rejected by $\epsilon = 80$ ms, these two events will not be considered subevents, and the associated internal multiple will be neglected in the prediction.

The internal multiple algorithm was designed assuming FSMs have been removed (Weglein et al., 1997). Thus, the FSM events in the dataset are expected to cause artifacts, since the prediction algorithm will assume that the FSM events are primaries. In this study, the FSMs are present at later times in the shot record that are outside the time window of interest. For this reason FSM removal, normally a significant step in pre-processing, can be safely avoided in this study.

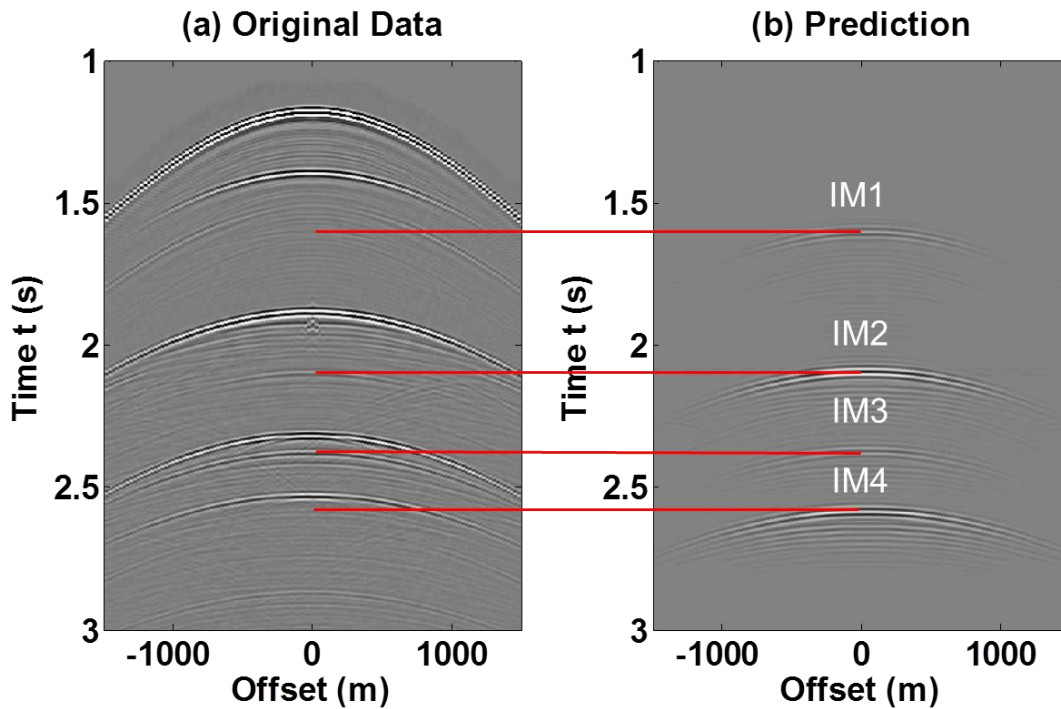


Figure 4.10: Comparison of input data (a) with prediction output (b). The red lines indicate the positions of internal multiples.

Figure 4.10 shows the physical modelling data input and the associated prediction output. The internal multiples indicated by the red lines are consistent with Figure 4.9. Artifacts in the form of near-offset oscillations from missing lateral wavenumber combinations (with some influence of the noise in the physical modelling data) are visible. The zero-offset trace from this output is also examined in detail in Figure 4.11. The zero-offset trace from the physical modelling data is plotted in Figure 4.11 (a), the prediction output in Figure 4.11 (b), and the zero-offset trace from the synthetic data is plotted for comparison in Figure 4.11 (c). Even though there are some non-negligible artifacts below each predicted internal multiple, the arrival times of the prediction and the synthetic data match well.

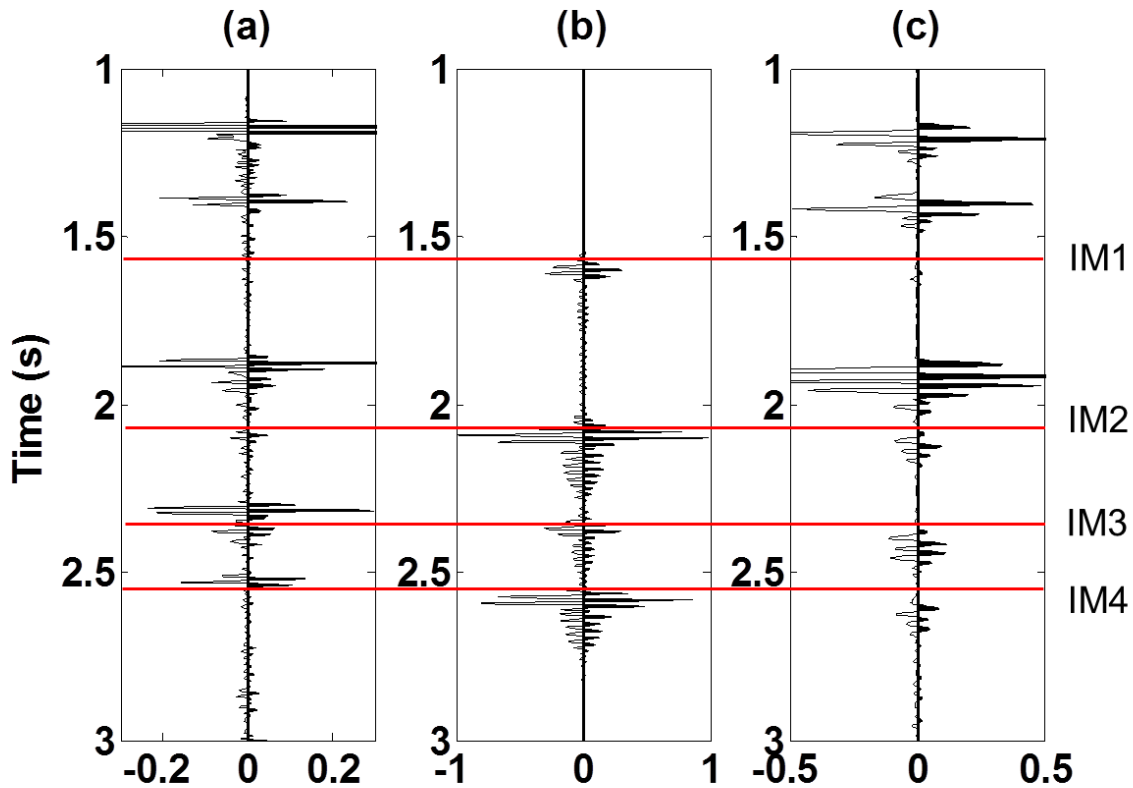


Figure 4.11: Details of internal multiple predictions. (a) Input data: the zero-offset trace from the physical modelling data; (b) prediction output: the zero-offset trace from the prediction output in Figure 4.10; (c) the zero-offset trace from the synthetic data.

4.4.3 Analysis of the three parameters chosen in the algorithm

The 1.5D prediction algorithm contains three nested loops. Figure 4.12 outlines the basic form in pseudo-code. The loops are over lateral wavenumber, temporal frequency, and pseudo-depth. In this section, the results of different beginning and ending integration points are evaluated.

Beginning and ending integration points in the nested integrals can be chosen optimally to reduce computational burden. Selecting proper frequencies affects both the computational cost and the quality of the final image. In Figure 4.13, two prediction frequencies of 30-80 Hz and 10-50 Hz respectively are illustrated. There is a lot of noise above and below each internal multiple event

(Figure 4.13 (b)), while the data in Figure 4.13 (a) are much cleaner. The frequencies can be chosen optimally from a simple Fourier decibel spectrum (Figure 4.14); the range of 30 to 80 Hz appears to contain the desired data and the rest of the data are buried in the noise.

```

For ii = xxB : xxE
   $F = \frac{xx(ii)^2 c_0^2}{w^2}$ 
   $qg = (w/c_0) * \text{sqrt}(1 - F)$ 
  For jj = wB : wE
     $A1 = i * 2 * qg(jj) * z$ ;
     $A2 = -i * 2 * qg(jj) * z$ ;
     $I1 = b1(:, ii) * \exp(A1)$ ;
     $I2 = b1(:, ii) * \exp(A2)$ ;
  For kk = zB : zE
     $S = \text{sum}(I1(kk + \epsilon : zE))$ ;
     $P = P + I2(kk) * S^2$ ;
  End
   $P = P * dz$ ;
End
End
```

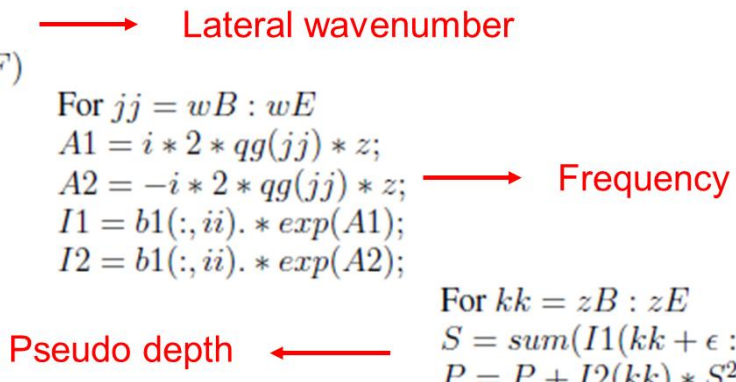


Figure 4.12: Prediction algorithm in the code (from Innanen, 2012).

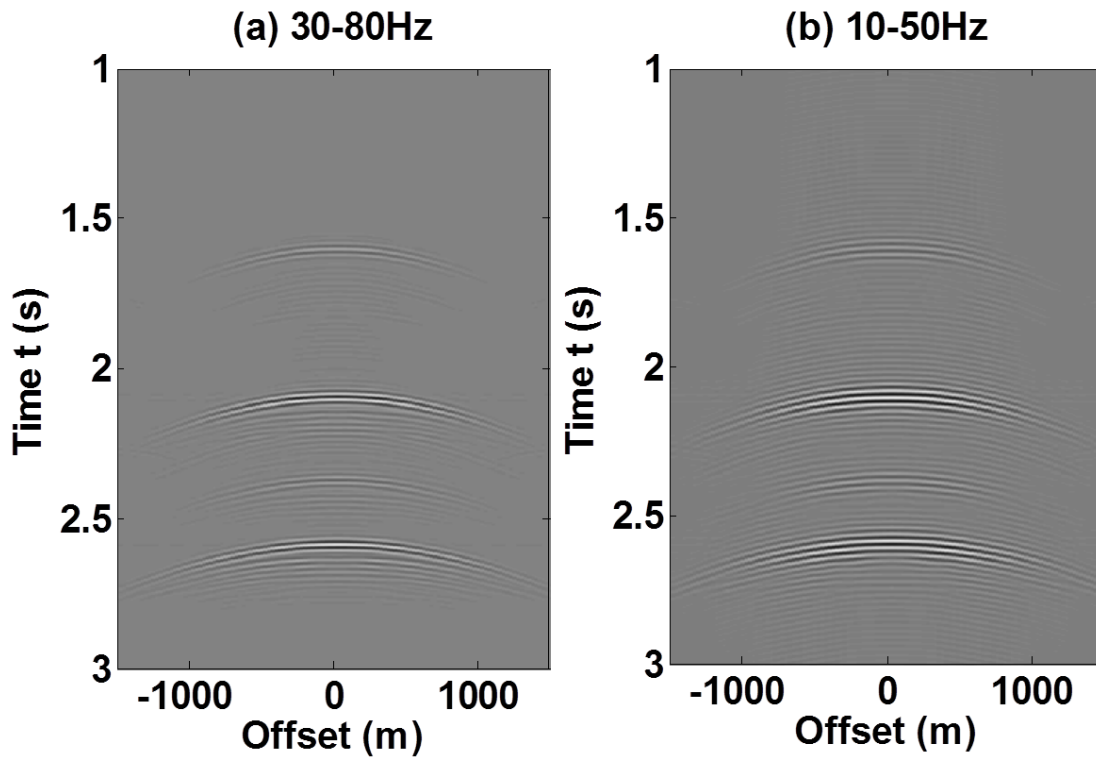


Figure 4.13: Comparison of two internal multiple prediction outputs with different maximum and minimum frequencies. (a) 30-80 Hz; (b) 10-50 Hz.

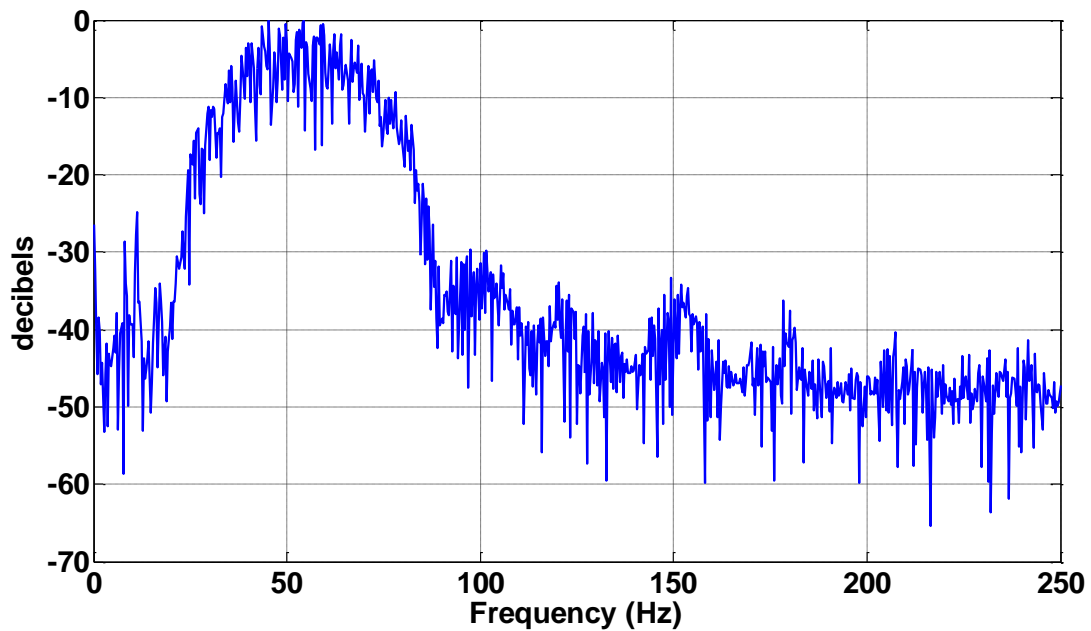


Figure 4.14: Fourier amplitude spectrums of the zero-offset trace using decibel scale.

The absolute values of $b_1(k_g, z)$ are plotted in Figure 4.15. On the left edge of the panel the primaries and internal multiples are intersecting the z axis at their proper pseudo-depths. This figure suggests that the shallowest contribution comes from the depth index of 540, and last contribution primary is roughly 1020. By the same principle, the smallest and largest contributing wavenumber indexes were chosen to be 513 and 1024. These parameters can be chosen by an iterative procedure, in which depth and wavenumber index ranges are gradually narrowed down until it reaches the points that will not destroy the final image. Table 4.3 illustrates a series of experiments that shows considerable computational savings by manipulating the parameters. The final result is compared with the first experiment, which shows a time cost savings of 114%.

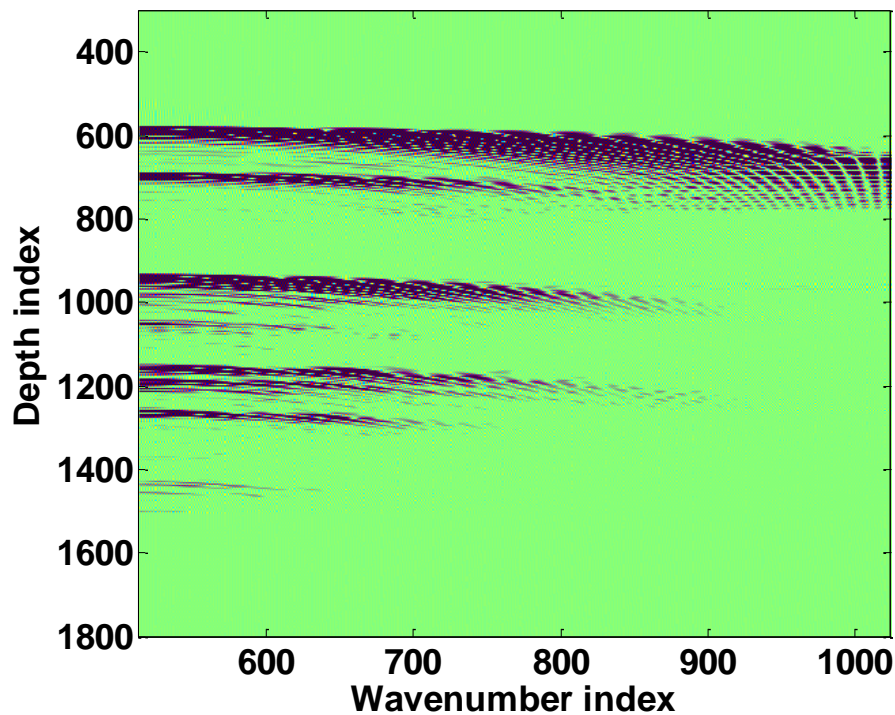


Figure 4.15: The algorithm input is generated using the input data and the single reference velocity. Note that this is only one side of the data; the other side can be filled later through conjugate symmetry.

Table 4.3: Time costs with different parameters chosen

freBEG (Hz)	freEND (Hz)	zBEG	zEND	kxBEG	kxEND	Time (s)
25	80	540	1020	513	1024	1256.96
25	80	560	1015	513	1024	1189.85
25	80	560	1015	513	900	856.57
25	80	560	1015	513	800	636.24
30	80	560	1015	513	800	588.51

4.5 Chapter summary

In this chapter, a MATLAB implementation of the 1.5D version of the inverse scattering series internal multiple prediction algorithm on marine physical modelling seismic data is examined. ProMAX was used to pre-process the data to suppress the source wavelet reverberations between the first two primaries. Usually, deconvolution and deghosting are important steps in pre-processing. In the physical modelling experiment, the source and receiver transducers were very close to the water surface so strong source and receiver ghosts were not expected, therefore the deghosting step was avoided. Spiking deconvolution was used as the deconvolution method. A synthetic dataset was also built using a finite-difference program for comparison. Prediction results show good agreement with both synthetic data and physical modelling data. The effect on the algorithm from the choice of a single ϵ value was also discussed. Even if subtraction is problematic, prediction results can lead to obtaining an “internal multiple probability map”, which is useful for identifying both internal multiples and primaries whose amplitudes experienced interference. However, it is also true that even a simple variable $\epsilon(k_g)$ may provide significantly improved prediction results permitting subtraction to proceed. Choosing the

beginning and ending integration points in the nested integrals optimally leads to considerable computation savings.

Chapter Five: The Hussar experiment

5.1 Chapter overview

In this chapter, the 1.5D internal multiple prediction algorithm is analyzed in the context of a synthetically generated dataset designed to simulate data from the 2011 CREWES Hussar field experiment (Margrave et al., 2012). Several well logs were available along the 2D Hussar seismic line. One was subjected to a process known as blocking, in order to infer a profile of seismic (elastic) properties versus depth which captures the key geological structures influencing reflection seismic data. An acoustic finite difference modelling procedure was enacted to create synthetic data (referred to hereafter as “Hussar synthetic”). Analysis of the internal multiple prediction algorithm using these data is suggestive that important internal multiples generated by the relatively thin layers of the Hussar geology can be effectively predicted with this technology.

Internal multiple prediction and attenuation has primarily applied in marine environments, particularly in deep water. The characteristics of land seismic data such as noise, statics, and coupling are major obstacles for internal multiple elimination (Luo et al., 2011). The layer/boundary approach introduced by Verschuur and Berkhout (2001) has been tested on land seismic data by Luo et al. (2007) and Kelamis et al. (2008) with some success. Extensive knowledge of the main multiple generators is required to use the layer/boundary approach. On land, most of the internal multiples are generated by a series of complex, thin layers encountered in the near surface (Kelamis et al., 2006). Therefore, this method is not always suitable. Luo et al. (2011) reported significant improvements of tests using the inverse scattering series approach (Weglein et al., 1997; 2003); recently Hernandez and Innanen (2014) demonstrated clear predictions based on the inverse scattering series approach are possible on poststack land dataset.

The purpose of this chapter is to examine the applicability of using the 1.5D internal multiple prediction algorithm on land data. An experiment was carried out on a synthetic land dataset using the sonic log synthetics acquired by CREWES near Hussar, Alberta. Prestack data were analyzed with the 1.5D algorithm, in particular with an eye for the success with which the multiples reverberating in the relatively thin-layering of the blocked log model can be predicted, and for the influence of realistic offsets on the generation of far-offset artifacts in the prediction.

5.2 The Hussar experiment overview

5.2.1 Introduction

On September 2011, CREWES collaborated with Husky Energy, Geokinetics, and INOVA to carry out a seismic experiment. The data were collected to test inversion methods and study the low frequency content of seismic data near Hussar, Alberta (Margrave et al., 2012). The line was 4.5 km crossing three wells, 12-27, 14-27 and 14-35, see Figure 5.1 (Lloyd, 2013). Several receiver and source types were applied during the seismic experiment. The receiver types that were used included 3-component 10 Hz SM-7 (ION-Sensor) geophones with 10 m spacing, 3-component Vectorseis (MEMS) accelerometers with 10 m spacing and 1-component 4.5 Hz geophones with 20 m spacing (Margrave et al., 2012). For sources, a 2 kg charge of dynamite at 15 m depth, a low dwell sweep using a standard production vibrator (Failing Y2400) and the INOVA AHV-IV (model 364) vibrator (INOVA 364) were used (Margrave et al., 2012).

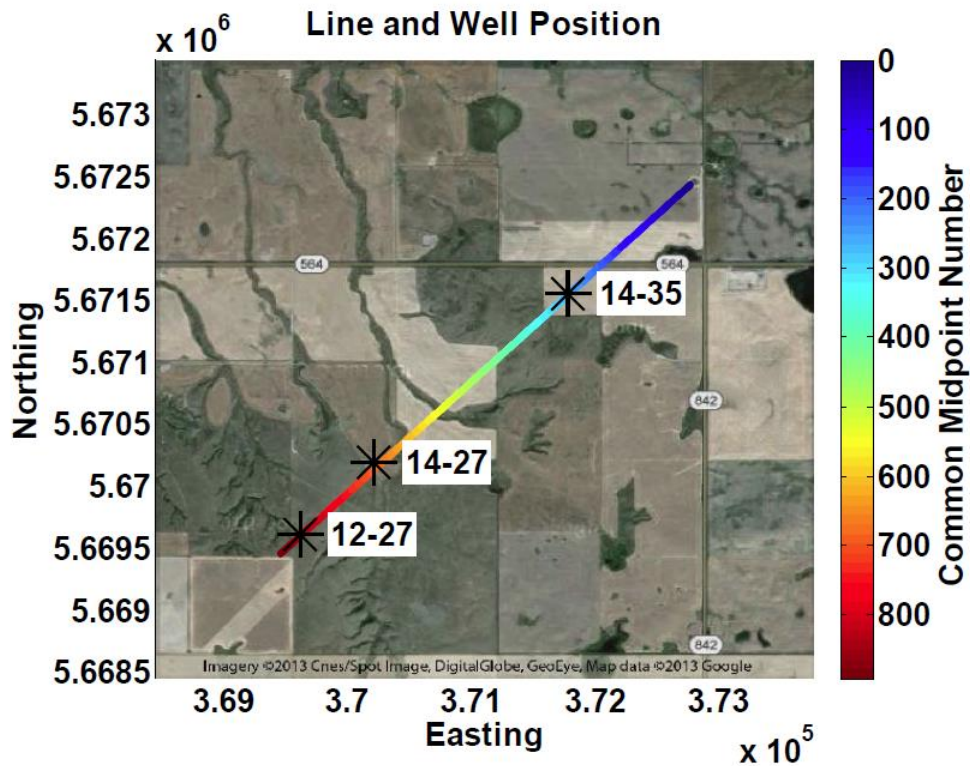


Figure 5.1: The 4.5 km Hussar seismic line is shown along with the locations of the three wells (from Lloyd, 2013).

5.2.2 Well log analysis

All the wells had P-wave sonics, density and gamma ray logs, while well 12-27 also had an S-wave sonic. For this study, only the P-wave sonic of well 12-27 was used, the depth of log extended from approximately 200 m to 1600 m. In Figure 5.2, only the P-wave sonic log is displayed to analyze and model the arrival times of the events for the seismic data. The tops of eight important geological markers shown are Belly River, Lea Park, Colorado, Medicine Hat, Viking, Mannville, Glauconitic and Pekisko.

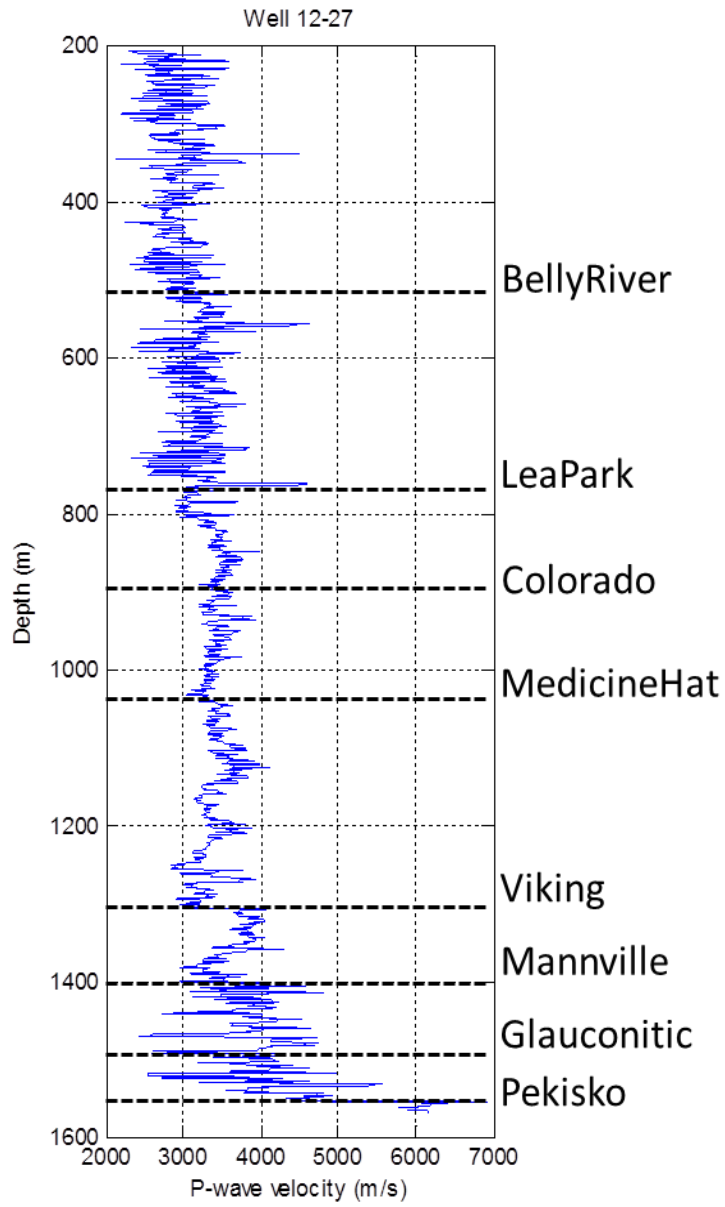


Figure 5.2: Well 12-27 P-wave sonic log with geological markers.

5.3 Hussar synthetics experiment

5.3.1 Block log

The well data illustrated in Figure 5.2 were used to develop a blocked P-wave velocity profile involving the eight markers using *blocklogs.m* from the CREWES toolbox. The algorithm eliminated all shoulder effects so that the log curves were resolved into zones of constant value, separated by horizontal boundaries. The geology became more ‘bed-like’ in appearance. Also, a gradient overburden was attached that extended from the surface to the local averages of values found at the top of the log. The P-wave velocity was chosen to be 2563 m/s to fill in a linear gradient overburden from the first logged depth to the surface. The original log is illustrated in black and the blocked log in red (Figure 5.3 (a)), opposite the blocked log alone (Figure 5.3 (b)). The depth step of the log being blocked was 100 m. Some details were ignored due to the size of the depth step. A smaller depth step for thin layers will be tested in a later section.

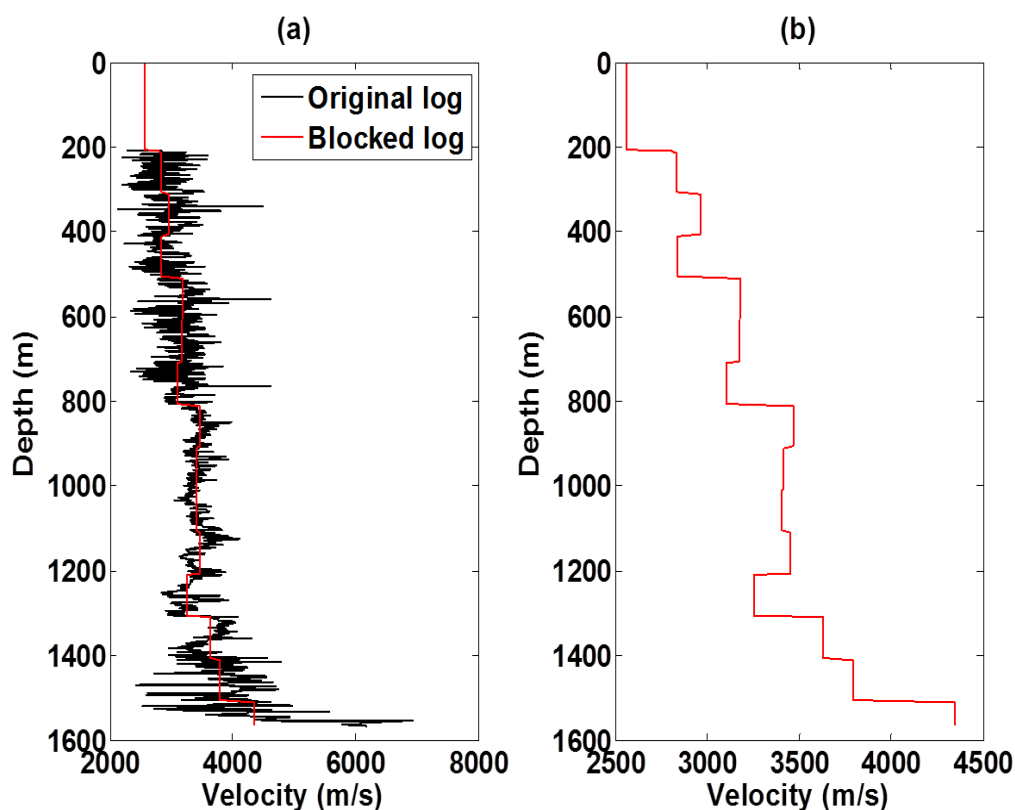


Figure 5.3: A blocked P-wave velocity profile. (a) Shows the original log in black and the blocked log in red; (b) shows only the blocked log. The depth step of the log being blocked is 100 m.

5.3.2 Internal multiple prediction

The velocity model based on the blocked log is illustrated in Figure 5.4. The lowest velocity is about 2600 m/s and the highest velocity is about 4500 m/s. Then acoustic finite difference forward modelling codes in the CREWES toolbox were used to create the data. Land data lack the well-defined FSMs that are present in marine data, but possess more complex near surface. To avoid FSMs, the boundary conditions were set to be absorbing on all four sides; surface wave effects were neglected in this analysis. The source and receiver interval was 5 m, and the record length was 1.5 s with a sampling rate of 4 ms. The data were generated with lowcut, lowpass,

highpass and highcut frequencies of 10 Hz, 20 Hz, 80 Hz and 100 Hz, respectively. As such the geology and geometry of the Hussar experiment is correctly represented but the full broadband character is not (this is to allow our numerical analysis to proceed more expediently). The algorithm requires only the upgoing wavefield as input, therefore the direct wave was removed, in this case by modelling and subtracting it (in practice a direct wave mute is normally applied). In Figure 5.5, the shot record containing only primary reflections and internal multiples is plotted. In Figure 5.6, the input $b_1(k_g, z)$ is illustrated from which the beginning and ending points of depth index and wavenumber index can be determined respectively. The input is only for one side of the data (positive k_g values); the wavenumbers for the other side can be filled later through conjugate symmetry.

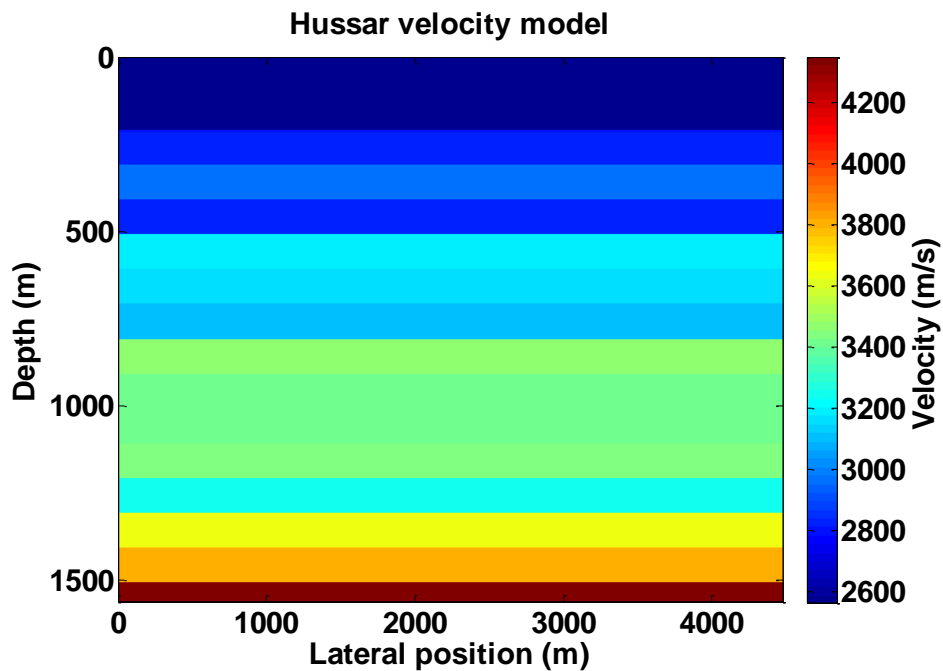


Figure 5.4: Velocity model based on the blocked P-wave velocity profile.

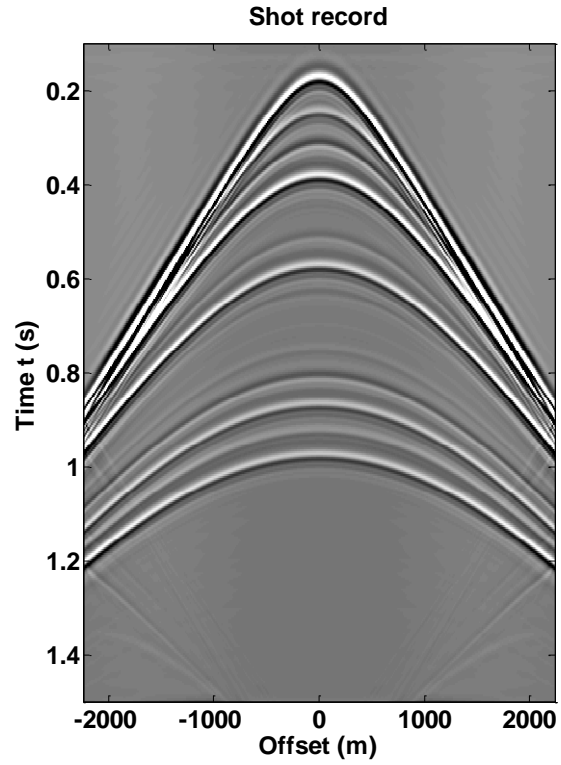


Figure 5.5: Shot record generated from the velocity model.

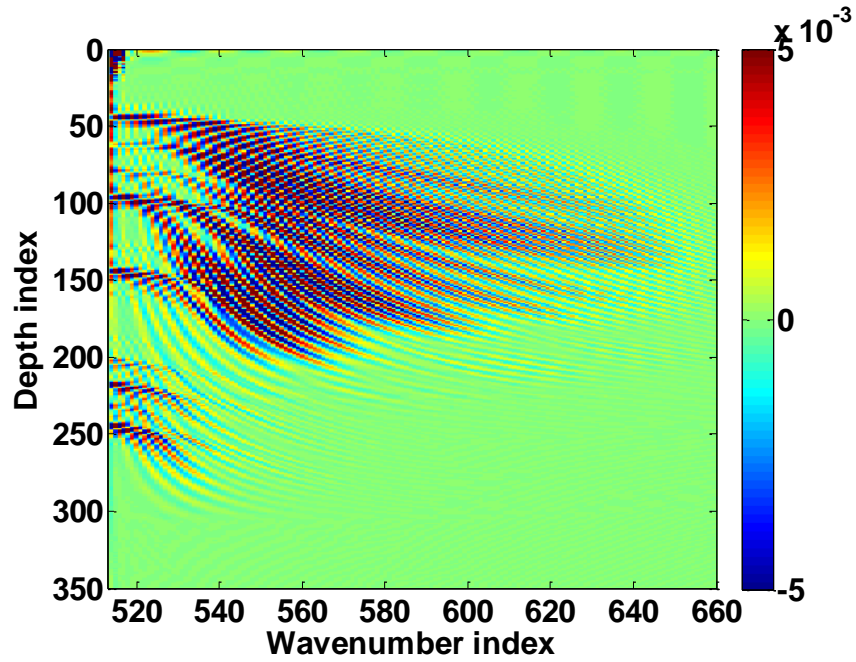


Figure 5.6: The algorithm input is generated using the input data and single reference velocity.

A chosen ϵ value of 50 ms is promising based on the comparison of the 1.5D internal multiple prediction (Figure 5.7 (a)) with the original shot record (Figure 5.7 (b)). The first internal multiple at approximately 0.6 s interferes with a primary, and has been correctly predicted. Also, internal multiples from possible generators are shown below 1.1 s in Figure 5.7 (a). The kinematics of the internal multiples appear to be correct. The amplitudes are also as expected, with discrepancies increasing with the number of transmission interactions the event experiences (Weglein and Matson, 1998).

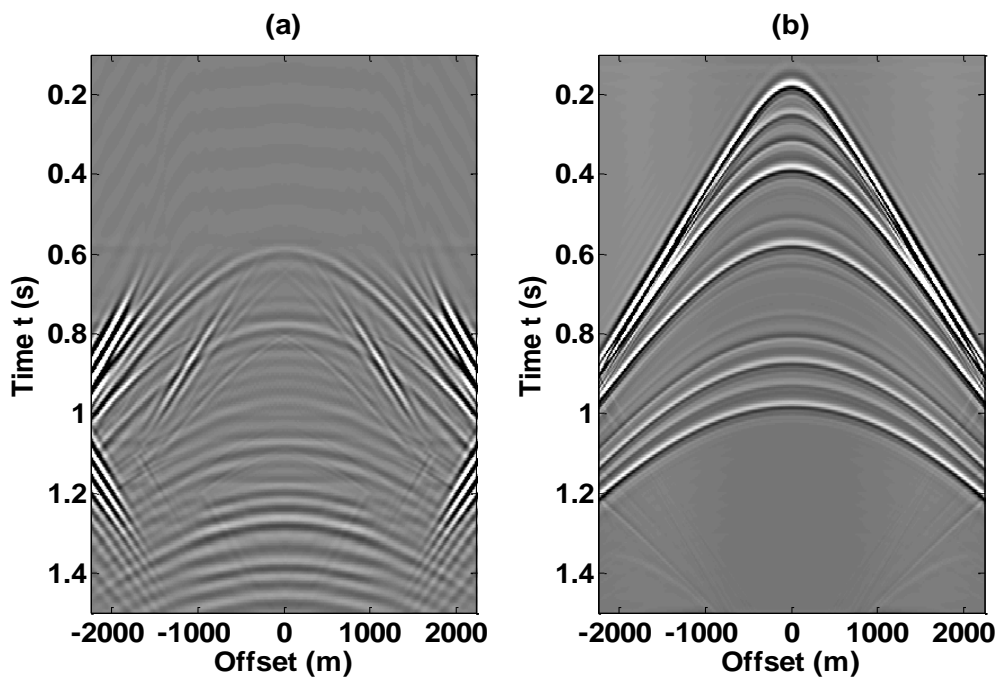


Figure 5.7: Comparison of prediction output with input. (a) Prediction output; (b) input data.

However, artifacts are prominent at far offsets of the prediction record. The explanation for this is the aperture. The prediction which is created in the Fourier domain is sensitive to sharp truncations in the signal. An inquiry was next made into whether by increasing the offset these artifacts can be reduced. Greater offset was simulated by increasing the receiver spacing to 10 m,

and the final result is shown in Figure 5.8. Compared with Figure 5.7, significant improvement can be seen in the prediction result. There are no artifacts in the far-offset, and the moveout pattern of each internal multiple event seems correct. Thus far-offset artifacts can be effectively eliminated with acquisition changes; when this is not possible, correction of this phenomenon must be achieved with tapering.

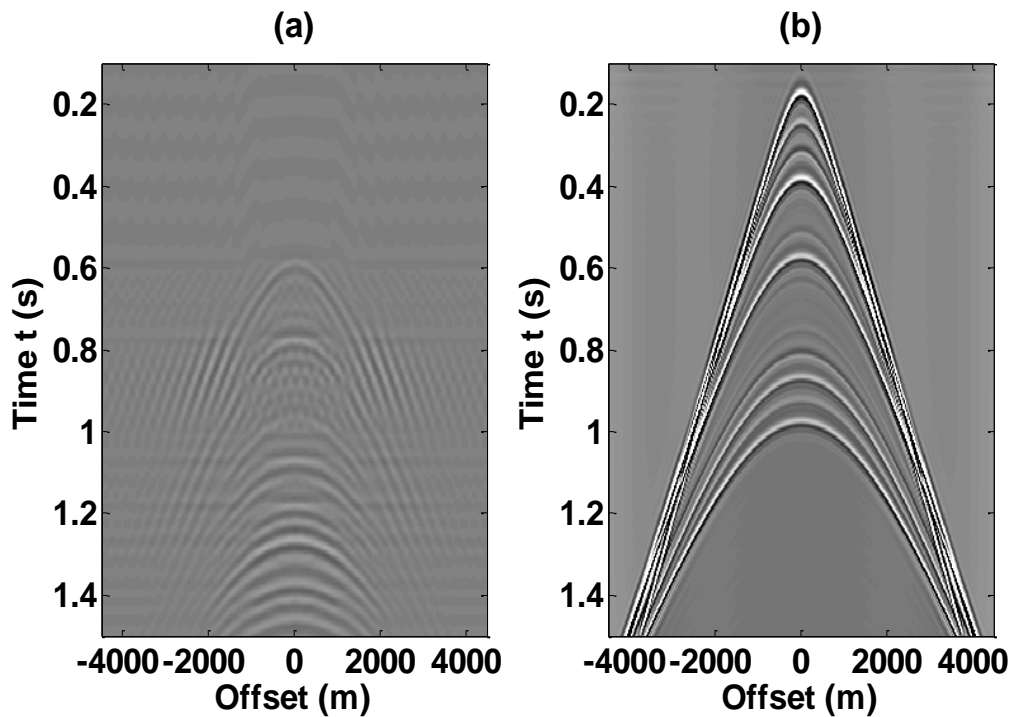


Figure 5.8: Comparison of prediction output with input. (a) Prediction output; (b) input data.

5.3.3 Relatively thin layers test

Next, the depth step of the log being blocked was decreased to 50 m. The goal was to study whether the internal multiple prediction algorithm could successfully predict internal multiples generated by relatively thin layers. Figure 5.9 illustrates the blocked log and Figure 5.10 shows the velocity model. In Figure 5.11, the shot record generated from the velocity model is plotted.

The model is composed of a large number of thin layers, with obvious presence of internal multiples in this dataset. The prediction result is shown on the left in Figure 5.12, and the original shot record is depicted on the right. The performance of the 1.5D internal multiple prediction algorithm is acceptable, especially at the zone between 0.6 s and 0.8 s where several internal multiples are interfering with primaries.

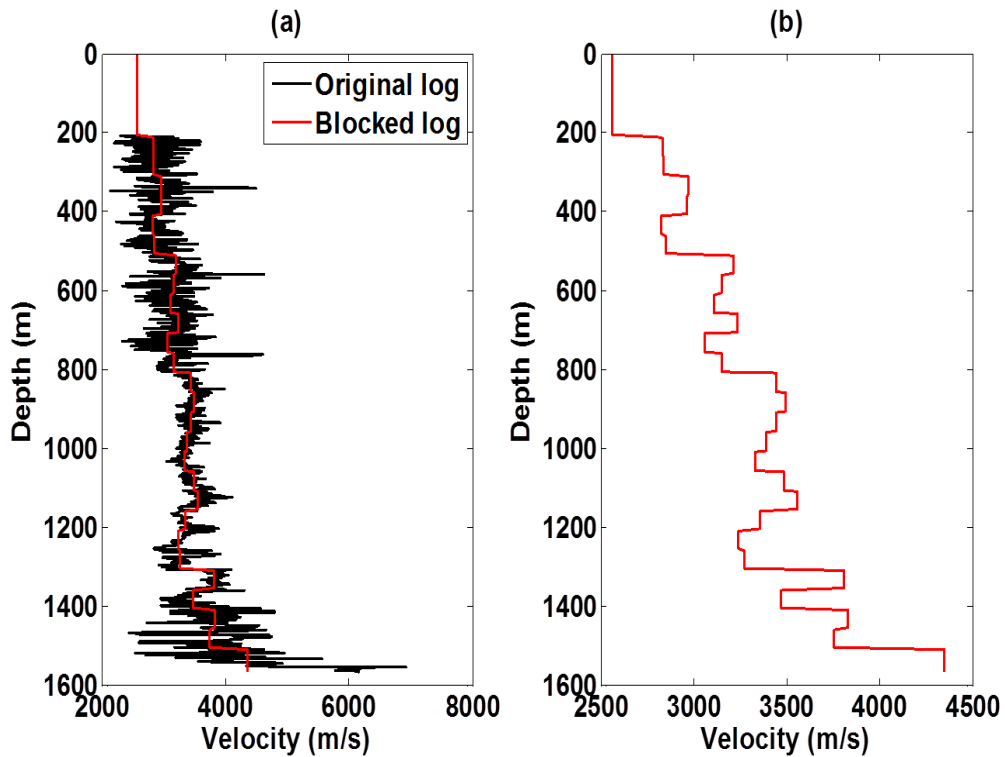


Figure 5.9: A blocked P-wave velocity profile. (a) Shows the original log in black and the blocked log in red; (b) shows only the blocked log. The depth step of the log being blocked is 50 m.

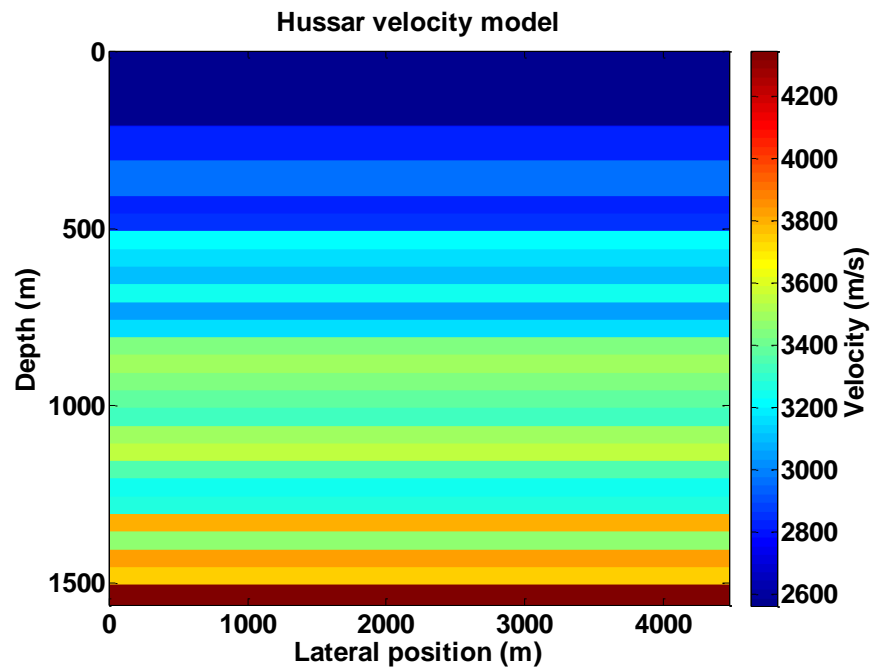


Figure 5.10: Velocity model based on the new blocked P-wave velocity profile.

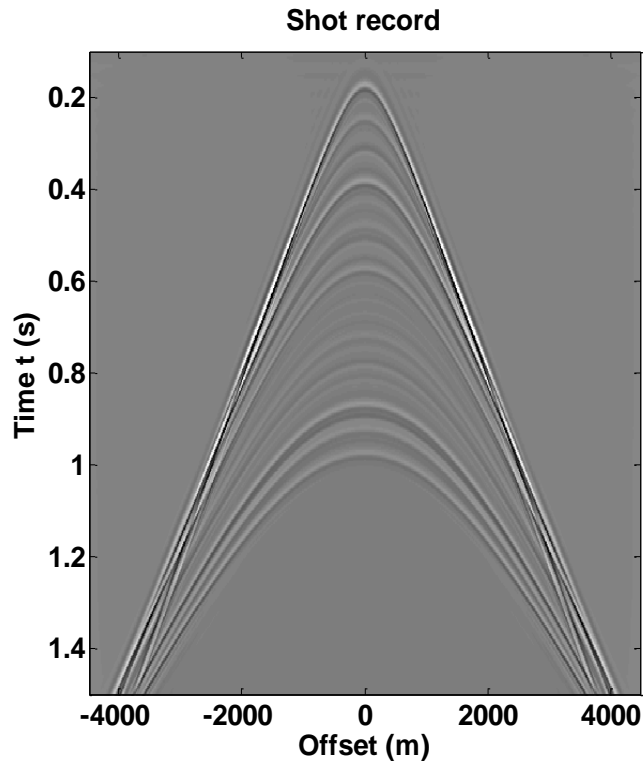


Figure 5.11: Shot record generated from the new velocity model.

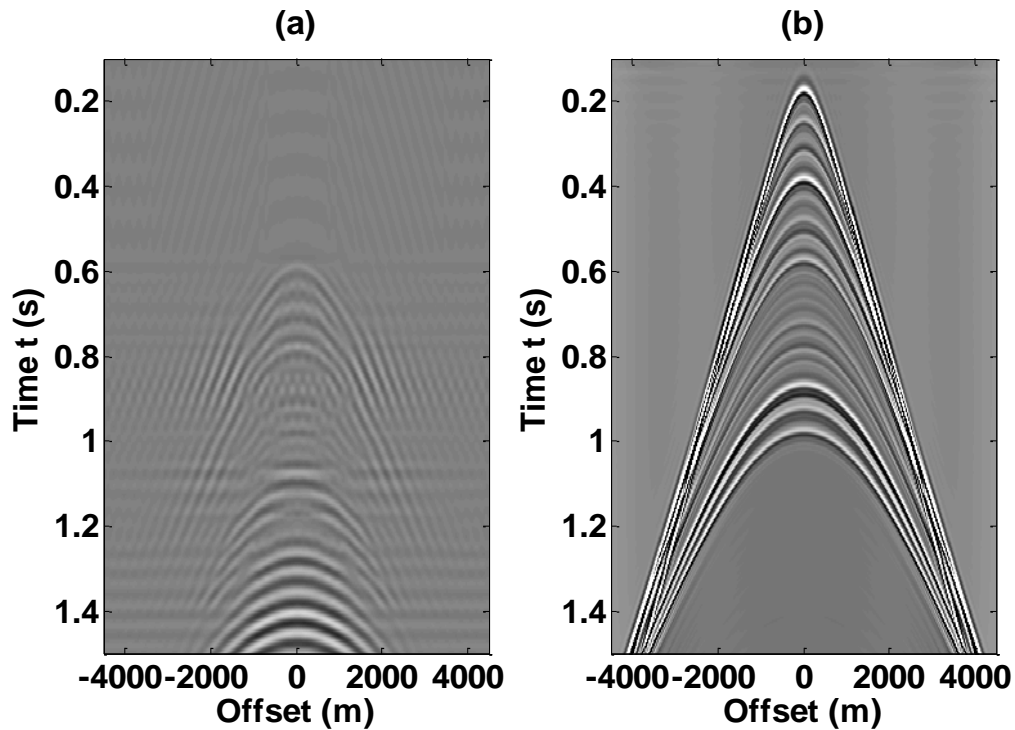


Figure 5.12: Comparison of prediction output with input. (a) Prediction output; (b) input data.

5.4 Chapter summary

The performance of the 1.5D internal multiple prediction algorithm on Hussar synthetics is examined. The synthetics were acquired by blocking well 12-27 with different depth steps. The effectiveness of the 1.5D internal multiple prediction algorithm is demonstrated by the datasets, yielding promising results. The inverse scattering series technology does not require velocity information from the subsurface or any advance knowledge of the multiple generators. This method has been proven to be effective in land seismic data where close interference between primaries and internal multiples occur. Also, it can successfully predict internal multiples generated by relatively thin layers, given that the interval between two primaries is larger than

the optimal ϵ value. By extending the synthetic in offset, the results suggested that certain prediction artifacts can be tied to land apertures.

Chapter Six: Conclusions

6.1 Conclusions

The main goal of this thesis is to evaluate the effectiveness of the inverse scattering series based internal multiple prediction algorithm on various datasets, with an ultimate goal of developing and enhancing the applicability of the method on land seismic data, where it encounters significant challenges. Three case studies were used to accomplish this goal, including synthetic data, physical modelling data and well log synthetics from Hussar data. The following conclusions are made based on the results of this research:

- The computational cost of the 1.5D algorithm is dramatically less compared to the 2D algorithm because few wavenumbers are required for the 1.5D algorithm. The 1.5D method does not need any subsurface information and is suitable for the situation where primaries and internal multiples are mixed together.
- The effects of various ϵ values were analyzed. For smaller ϵ values, artifacts are seen at the arrival times of primaries, and for larger ϵ values, important information is damaged in the prediction output. The ϵ value can be effectively chosen by studying the evolution of large offset artifacts as ϵ is gradually increased.
- The rate of error increase in the 1.5D internal multiple prediction algorithm was examined using data with increasing interface dip. For smaller dipping angles, the algorithm correctly predicts both the zero-offset travel times and moveout patterns. Errors become significant for larger dipping angles. Regardless, the 1.5D algorithm remains valuable in assisting with the identification of the positions of internal multiples, which is helpful for subsequent inversion and interpretation.

- A method to mitigate the large-dip artifacts noticeable in unfiltered 1.5D internal multiple predictions is pointed out. This is done by implementing a k_g -dependent integration-limiting parameter ϵ . This method is preferable to the normal filtering method as it ties the artifacts to its origins.
- ProMAX was used to pre-process the data from physical models. Spiking deconvolution was employed to suppress source wavelet reverberations between the first two primaries. Deconvolution and deghosting are important steps in pre-processing, but deghosting was not used because the source and receiver transducers were close to the water surface in the physical modelling experiment.
- Even if subtraction is problematic, prediction results can lead to obtaining an “internal multiple probability map”, useful for identifying both internal multiples and primaries whose amplitudes are likely to have experienced interference from them. However, a simple variable $\epsilon(k_g)$ may provide significantly improved prediction results permitting subtraction to proceed.
- Choosing the beginning and ending integration points in the nested integrals optimally leads to considerable computation savings.
- In the Hussar synthetics case, the synthetics were acquired by blocking well 12-27 near Hussar, Alberta with different depth steps. The 1.5D algorithm yielded promising results.
- The 1.5D algorithm has been proven to be effective in land seismic data where close interference between primaries and internal multiples occur. Also, it can successfully predict internal multiples generated by relatively thin layers, given that the interval between two primaries is larger than the optimal ϵ value.

- Far-offset artifacts can be effectively eliminated with acquisition changes; when this is not possible, correction of this phenomenon must be achieved with tapering.

6.2 Recommendations

This thesis mainly focused on the 1.5D internal multiple predictions. However, some recommendations regarding the use of 1D internal multiple predictions have also been made. For any particular seismic dataset, given sufficient prestack data coverage, all of the prediction errors of the 1D algorithm can be avoided by using 1.5D, 2D, or 3D versions of the algorithm. The 1D version runs very quickly, so it may be wise to derive as much information as possible from its use as a quick reconnaissance tool. Moving toward a set of maximally general recommendations about when exactly this approximate use of the algorithm is appropriate, the results below represent the initial findings:

- For horizontal reflectors, the result has errors above 5% when the offset is greater than 1.5 times the generator depth.
- The influence of dipping angles on the prediction algorithm was tested on the zero-offset trace, and these results can be extended to relatively near-offset cases. When the generator becomes the dipping interface, it has the strongest effect on the algorithm. In this case, the error rises above the chosen threshold of 1% when the dipping angle exceeds 10 degrees. When the second interface is the dipping interface, a similar error measure exceeds 1% when the dipping angle reaches 11 degrees. When the third interface is dipping, the error exceeds the threshold at a dipping angle greater than 15 degrees. In these studies, 10 degrees dip appears to be a reasonable upper limit for acceptable results.

6.3 Future work

In the study of the effects of dipping angles on the accuracy of the 1D and 1.5D algorithm, the main priority for future research is to move beyond the arbitrary choice of allowable error level. A possible way to achieve this goal is to quantify the error by studying the effects on adaptive subtraction of increasing travel time shift between predicted and measured internal multiples. However, this is problematic as the errors of different offset traces are unreliable which makes adaptive subtraction of 1.5D or 2D difficult to proceed. Another future direction is to compare physical modelling data simulating a land seismic survey with synthetic shot records generated by *mFD2D* (developed by Peter Manning and Joe Wong of CREWES). The *mFD2D* algorithm is executed with MATLAB and uses a finite-difference, time-stepping method to simulate elastic wave propagation in two-dimensional environments. Field land data are ideal in testing the capabilities and limitations of the 1.5D internal multiple prediction algorithm. Well processed data from Western Canada with nearly horizontal reflectors are preferable. The characteristics of land seismic data are major obstacles for internal multiple elimination, including low signal-to-noise ratio, statics, fine layers, and poor spatial sampling. In this work, only the fine layers challenge has been touched on. The ultimate goal is to develop and enhance the applicability of 1.5D algorithm on land seismic data. Also, developing a 2D version of the algorithm is a CREWES priority.

References

- Araújo, F. V., Weglein, A. B., Carvalho, P. M., and Stolt, R. H., 1994, Inverse scattering series for multiple attenuation: an example with surface and internal multiples: 64th Annual International Meeting, SEG, Expanded Abstracts, **13**, 1039–1041.
- Berkhout, A. J., 1982, Seismic migration: imaging of acoustic energy by wavefield extrapolation: 2nd Ed.: Elsevier Science Publishing Company.
- Coates, R. T., and Weglein, A. B., 1996, Internal multiple attenuation using inverse scattering: Results from prestack 1D and 2D acoustic and elastic synthetics: 66th Annual International Meeting, SEG, Expanded Abstracts, 1522-1525.
- De Melo, F., Idris, M., Wu, Z. J., Kostov, C., 2014, Cascaded internal multiple attenuation with inverse scattering series: Western Canada case study: 84th Annual International Meeting, SEG, Expanded Abstracts, 4113-4117.
- Geldart, L.P., and Sheriff, R.E., 2004, Problems in Exploration Seismology and their solutions: Society of Exploration Geophysicists, **14**.
- Hardy, R. J. J., and Hobbs, R. W., 1991, A strategy for multiple suppression: First Break, **4**, 139–144.
- Henley, D. C., and Wong, J., 2013, Which way is up?-experiences with processing physical modeling data: CREWES Annual Report, **25**.

- Hernandez, M., 2012, Internal multiple prediction: an application on synthetic data, physical modeling data and field data: MSc Thesis, University of Calgary.
- Hernandez, M., and Innanen, K. A., 2014, Identifying internal multiples using 1D prediction: physical modelling and land data examples, Canadian Journal of Geophysical Exploration, **39**, 1, 37-47.
- Ikelle, L.T., Amundsen, L., and Eiken, O., 1997, Multiple attenuation at primary/multiple interferences: The Troll example: The Leading Edge, **16**, No. 12, 1751–1753.
- Ikelle, L., Roberts, G., and Weglein, A. B., 1997, Source signature estimation based on the removal of first-order multiples: Geophysics, **62**, 1904–1920.
- Innanen, K. A., 2011, Seismic Signal Analysis Course Notes.
- Innanen, K. A., 2012, 1.5D internal multiple prediction in MATLAB: CREWES Annual Report, **24**.
- Innanen, K. A., and Pan, P., 2014, Large dip artifacts in 1.5D internal multiple prediction and their mitigation: CREWES Annual Report, **26**.
- Kabir, M. M. N., and Marfurt, J. J., 1999, Toward true amplitude multiple removal: The Leading Edge, **18**, 66–73.
- Kelamis, P. G., Zhu, W., Rufaii, K. O., and Luo, Y., 2006, Land multiple attenuation-The future is bright: 76th Annual International Meeting, SEG, Expanded Abstracts, 2699-2703.

- Kelamis, P. G., Luo, Y., Zhu, W., Rufaii, K. O., 2008, Two pragmatic approaches for attenuation of land multiples: 70th EAGE Conference & Exhibition.
- Lamont, M. G., Hartley, B. M., and Uren, N. F., 1999, Multiple attenuation using the MMO and ISR preconditioning transforms: *The Leading Edge*, **18**, 110–114.
- Landa, E., Keydar, S., and Beyfer, I., 1999, Multiple prediction and attenuation using wavefront characteristics of multiple-generating primaries: *The Leading Edge*, **18**, 60–64.
- Landa, E., Belfer, I., and Keydar, S., 1999, Multiple attenuation in the parabolic tau–p domain using wavefront characteristics of multiple generating primaries: *Geophysics*, **64**, 1806–1815.
- Lawton, D. C., Cheadle, S. P., Gallant, E. V., and Bertram, M. B., 1989, Elastic physical modeling: *CREWES Annual Report*, **1**.
- Lawton, D.C., Margrave, G. F., and Gallant, E. V., 1998, Physical modeling of an anisotropic thrust: *CREWES Annual Report*, **10**.
- Lines, L. R., 1996, Suppression of short-period multiples-deconvolution or model-based inversion?: *Canadian Journal of Exploration Geophysics*, **32**, 1, 63-72.
- Lloyd, H. J., 2013, An investigation of the role of low frequencies in seismic impedance inversion: MSc Thesis, University of Calgary.
- Lokshantov, D., 1999, Multiple suppression by data-consistent deconvolution: *The Leading Edge*, **18**, 115–119.

- Luo, Y., Kelamis, P. G., Fu, Q., Huo, S., Sindi, G., Hsu, S., and Weglein, A. B., 2011, Elimination of land internal multiples based on the inverse scattering series: The Leading Edge, 884-889.
- Luo, Y., Zhu, W., Kelamis, P. G., 2007, Internal multiple reduction in inverse-data domain: 77th Annual International Meeting, SEG, Expanded Abstracts, 2485-2489.
- Mahmoudian, F., 2013, Physical modeling and analysis of seismic data from a simulated fractured medium: PhD Thesis, University of Calgary.
- Margrave, G. F., Mewhort, L., Phillips, T., Hall, M., Bertram, M. B., Lawton, D. C., Innanen, K. A. H., Hall, K. W. and Bertram, K. L., 2012, The Hussar low-frequency experiment: CSEG Recorder, Sept., 25-39.
- Morley, L., and Claerbout, J., 1983, Predictive deconvolution in shot–receiver space: Geophysics, **48**, 515–531.
- Pan, P., and Innanen, K. A., 2014, Numerical analysis of 1.5D internal multiple prediction: 84th Annual International Meeting, SEG, Expanded Abstracts, 4135-4139.
- Peacock, K., and Treitel, S., 1969, Predictive deconvolution: theory and practice: Geophysics, **34**, 2, 155-169.
- Ramirez, A. C., and Weglein, A. B., 2005, An inverse scattering internal multiple elimination method: Beyond attenuation, a new algorithm and initial tests: 75th Annual International Meeting, SEG, Expanded Abstracts, 2115-2118.

Reshef, M., Keydar, S., and Landa, E., 2003, Multiple prediction without pre stack data - an efficient tool for interpretive processing: *First Break*, **21**, No. 3.

Sloat, J., 1948, Identification of echo reflections: *Geophysics*, **13**, 1, 27-35.

Spratt, R. S., Goins, N. R., and Fitch, T. J., 1993, Pseudo-Shear-The Analysis of AVO: *Investigation in Geophysics Series*, **8**, 37-56.

Taylor, J. R., 1972, *Scattering Theory*: New York, John Wiley & Sons, Inc.

Verschuur, D. J., 1991, Surface-related multiple elimination, and inverse approach: PhD Thesis, Delft University of Technology.

Verschuur, D. J. and Berkhout, A. J., 2001, CFP-based internal multiple removal, the layer-related case: 71st Annual International Meeting, SEG, Expanded Abstracts, 1997-2000.

Verschuur, D. J., Berkhout, A. J. and Wapenaar, C. P. A., 1992, Adaptive surface-related multiple elimination: *Geophysics*, **57**, 1166-1177.

Verschuur, D. J. and Prein, R. J., 1999, Multiple removal results from Delft University: *The Leading Edge*, **18**, 86-91.

Weglein, A. B., 1999, Multiple attenuation: an overview of recent advances and the road ahead (1999): *The Leading Edge*, **18**, 1, 40-44.

Weglein, A. B., 2014, Multiples: signal or noise?: 84th Annual International Meeting, SEG, Expanded Abstracts, 4393-4399.

- Weglein, A. B., Araújo, F. V., Carvalho, P. M., Stolt, R. H., Matson, K. H., Coates, R. T., Corrigan, D., Foster, D. J., Shaw, S. A., and Zhang, H., 2003, Inverse scattering series and seismic exploration: *Inverse Problems*, **19**, R27–R83.
- Weglein, A.B., and Dragoset, W. H., 2005, Multiple attenuation: *Geophysics Reprint Series*, **23**.
- Weglein, A. B., Gasparotto, F. A., Carvalho, P. M., and Stolt, R. H., 1997, An inverse-scattering series method for attenuating multiples in seismic reflection data: *Geophysics*, **62**, 6, 1975–1989.
- Weglein, A. B., Hsu, S., Terenghi, P., Li, X., and Stolt, R. H., 2011, Multiple attenuation: Recent advances and the road ahead: *The Leading Edge*, **30**, 864-875.
- Weglein, A. B., and Matson, K. H., 1998, Inverse scattering internal multiple attenuation: An analytic example and subevent interpretation: *SPIE Conference on Mathematical Methods in Geophysical Imaging*, 108–117.
- Wong, J., Hall, K. W., Gallant, E. V., Maier, R., Bertram, M. B., Lawton, D. C., 2009, Seismic Physical Modelling at the University of Calgary, *CSEG Recorder*, **34**, 37-43.
- Wong, J., Maier, R., Gallant, E. V., and Lawton, D. C., 2009, Physical modeling of a 3D marine seismic survey: *CREWES Annual Report*, **21**.
- Wu, J. and Weglein, A. B., 2014, The first test and evaluation of the inverse scattering series internal multiple attenuation algorithm for an attenuating medium: *84th Annual International Meeting, SEG, Expanded Abstracts*, 4130-4134.

Xiao, C., Bancroft, J., Brown, J., and Cao, Z., 2003, Multiple suppression: A literature review: CREWES Annual Report, **15**.

Yan, Y., 2002, Suppression of water-column multiples by combining components of oceanbottom seismic surveys: MSc Thesis, University of Calgary.

Yilmaz, O., 1989, Velocity–stack processing: Geophysical Prospecting, **37**, 357–382.

Zhou, Y. and Weglein, A. B., 2013, A new method to eliminate first order internal multiples for a normal incidence plane wave on a 1D Earth: 83rd Annual International Meeting, SEG, Expanded Abstracts, 4136–4140.